UNIVERSITÀ
DEGLI STUDI
DI PADOVA

DIPARTIMENTO
DI INGEGNERIA
DELL'INFORMAZIONE

MASTER THESIS IN BIOENGINEERING FOR NEUROSCIENCE

Enhancing Resting-State fMRI Analysis: Development of an Automated Multi-Echo Preprocessing Pipeline and Functional Connectivity Exploration in Parkinson's Disease

MASTER CANDIDATE

Giulia Bosello

Student ID 2055012

SUPERVISOR

Prof.ssa Alessandra Bertoldo

University of Padova

CO-SUPERVISOR

Ing. Denis Peruzzo, Ing. Alice Giubergia

IRCCS "Eugenio Medea"

ACADEMIC YEAR
2022/2023

Table of Contents

Chapter 1: Introduction

1.1 Outline: Aim and Structure

The human brain is a network of more than 80 billion individual nerve cells interconnected in neural circuits that build our perceptions of the external world, fix our attention, guide our decisions, and implement our actions.[1]

Functional magnetic resonance imaging (fMRI) is widely used to study these brain connections and to investigate neurological disorders, such as Parkinson's disease.

The primary objective of this study is to develop an automated pipeline for preprocessing multi-echo fMRI data at resting state: for this purpose, FSL and AFNI methodologies will be compared based on the evaluation of tSNR maps to evaluate the most effective preprocessing approach. After preprocessing, the data will be subjected to denoising with tedana.

The optimized pipeline will then be applied to the analysis of fMRI data to study differences in functional connectivity between patients with Parkinson's disease and healthy controls, focusing on the relationship between subcortical and cortical areas, as they can be detected more accurately with multi-echo data.

By identifying differences in brain connectivity between the groups through this research, a better understanding of Parkinson's disease can be gained: analysis of subcortical and cortical areas could reveal distinctive patterns useful for diagnosis and evaluation of the disease. The use of multi-echo data could also improve temporal resolution and increase sensitivity in detecting alterations in brain connectivity, providing valuable insights into Parkinson's disease.

In conclusion, this automated pipeline for processing resting-state multi-echo fMRI data in Parkinson's disease facilitates the study of functional connectivity, and the analysis of subcortical and cortical connections contributes to the understanding of the neural basis of the disease and the search for biomarkers for early diagnosis and treatment monitoring.

1.2 Resting-State fMRI

Functional magnetic resonance imaging (fMRI) is a noninvasive technique that provides comprehensive, multiparametric information on brain anatomy, function, and metabolism. [2] Among various fMRI techniques, resting-state fMRI (rs-fMRI) has gained significant advantages, revolutionizing brain mapping research and clinical studies. [3,4]

1.2.1 Principles

Resting-state fMRI was first described by Biswal et al. in 1995 and has since been widely used in both healthy subjects and patients with various neurological, neurosurgical, and psychiatric disorders.[5]

Resting-state fMRI is a specialized functional brain imaging technique that captures spontaneous brain activity without requiring subjects to engage in specific tasks, offering several key advantages over traditional task-based fMRI [4]: unlike paradigm- or task-based functional MRI, rs-fMRI is acquired in the absence of a stimulus or task (at rest), thus allowing easy signal acquisition, requiring minimal effort on the part of patients.

Functional MRI is based on blood oxygen level dependent contrast (BOLD) discovered by Seiji Ogawa in 1990. [4] Because of neurovascular coupling, the BOLD signal, although vascular in nature, is strongly correlated with neuronal activity [5], measuring associated changes in blood flow: when a specific brain region is active, blood flow in that area increases, resulting in detectable fMRI signals.[4]

However, the delay of the hemodynamic response after neural activation is responsible for the relatively poor temporal resolution of fMRI, and the BOLD signal may be altered in brain regions where blood flow is impaired. For example, pathological conditions such as traumatic or anoxic brain injury may affect neurovascular coupling and thus make fMRI suboptimal for assessing neural activity in these pathological conditions. Therefore, these factors must be considered when designing calibrated BOLD experiments and interpreting functional connectivity data, especially in patients with vascular disease.[5]

The principle of rs-fMRI is also based on the fluctuation of the BOLD signal, which is the same as active-task fMRI, but rs-fMRI focuses on the spontaneous alterations of the BOLD signal [5]: it uses the change in magnetization between oxygen-rich and oxygen-poor blood as a baseline measure. [6]

More specifically, brain activity is measured through the low-frequency BOLD signal in the brain [7]: the resting state signals captured in rs-fMRI are coherent low-frequency fluctuations in the range of 0.01-0.08 Hz. Notably, these signals represent distinct cortical network systems in the brain, and what was once discarded in task-based fMRI studies is now considered crucial for understanding spontaneous brain activity as a vital indicator of brain function.[3]

Data can be acquired with a dedicated scan, in which individuals are instructed to simply rest, or by inferring rest state data from rest periods embedded in a series of tasks. [5]
Rs-fMRI is commonly scanned in at least one of three different conditions: eyes closed (EC), eyes open (EO), and eyes fixed on a target (EO-F), usually a crosshair. In the EC case, participants are asked to close their eyes and remain awake during the scan; in the EO case, participants are asked to keep their eyes open; and in the EO-F case, participants are asked to keep their eyes fixed on an object, usually a crosshair presented in the center of the screen, during the scan.[6]

Through rs-fMRI, researchers have revealed the existence and properties of several brain networks in the resting state. Among them, the default mode network (DMN) discovered in 1998 is an important example: it is a functionally connected neural network that represents apparent brain states at rest. [4,7,8] These networks represent specific patterns of synchronous activity between different brain regions and play a crucial role in understanding brain function and communication.[8]
The principles of rs-fMRI have thus led to the exploration of functional connectivity, which involves the analysis of how different brain regions communicate with each other while the brain is at rest. This provides valuable information about the intrinsic architecture of the brain and can help detect alterations in functional connectivity in various neurological and psychiatric conditions.[7]

1.2.2 Advantages of rs-fMRI in Neuroimaging

One of the main advantages of resting-state functional MRI is its ability to allow easy acquisition of the neural signal, requiring minimal effort on the part of patients.[3]
The absence of requirements for task performance makes rs-fMRI a particularly attractive option for patients who may have difficulty executing task instructions: this makes it suitable for a wide range of populations, including those with neurological or mental disorders, neurosurgical and psychiatric conditions, as well as individuals with intellectual disabilities,

pediatric groups, and even unconscious patients. [3,5] These groups can be studied effectively with rs-fMRI techniques.

Biswal et al. first described the importance of neural activity fluctuations in rs-fMRI in 1995: in their experiment, subjects performed bilateral finger tapping, and the researchers observed a highly correlated BOLD time course between the left somatosensory cortex and homologous areas in the contralateral hemisphere. Since then, fMRI has been widely used in both healthy subjects and patients with neurological and psychiatric disorders to study the synchronous and spontaneous fluctuations of various networks in the resting state.[5]

In addition to its clinical and research applications, rs-fMRI offers significant clinical advantages over other neuroimaging techniques. In particular, it does not involve the use of ionizing radiation [4], making it safer than positron emission tomography (PET) and single photon emission computed tomography (SPECT) in the resting state. In addition, studies have shown promising reliability of rs-fMRI, further supporting its usefulness in various research areas.[3]

Over the past two decades, the application of rs-fMRI in clinical and research settings has thus experienced significant growth.[5]

1.2.3 Importance of rs-fMRI in Neurological Research [9]

Functional connectivity, defined as the temporal coherence of neuronal activity patterns between anatomically separated brain regions, reflects functional communication between them.

The BOLD (blood oxygen level dependent) signal provides a link between neuronal activity, which occurs during information processing, and MRI signal intensity. Because the BOLD signal has been shown to reflect the firing of neural populations with a strong correlation between its amplitude and local field potential data, it has been suggested that the BOLD signal is more related to synaptic activity than to neural activity per se, providing information about neuronal information processing at the synaptic level.

Over the past decade, research has focused on spontaneous oscillations of the resting-state BOLD signal in both healthy and pathological brains, revealing the existence of spatially distributed “intrinsic” resting-state (RS) functional connectivity networks known as resting-state networks (RSNs).

Independent component analysis (ICA) is the most used method to isolate functional connectivity networks from fMRI data, as it does not necessarily require prior hypotheses: by applying ICA, the spatial distribution of BOLD signal coherence between brain voxels can be assessed for several RSNs (Fig. 1.1), the most important of which are:

- *Default Mode Network (DMN):* involved in introspection, mind wandering and active episodic memory, it is deactivated during specific goal-directed behavior. Primarily includes the precuneus, posterior cingulate, bilateral inferior-lateral-parietal and ventromedial frontal cortices.
- *Sensorimotor network (SMN):* central to detect and process sensory input and prepare and execute motor functions. Includes primary sensorimotor cortex, supplementary motor area (SMA) and secondary somatosensory cortices.
- *Central executive network (CEN):* involved in executive control and working memory function, operates in mesiofrontal areas, including the anterior cingulate and para-cingulate cortices.
- *Salience network (SN):* Detects and responds to salient behavioral events, primarily involving the dorsal anterior cingulate cortex and bilateral insulae.
- *Dorsal attention network (DAN):* involves voluntary orientation (top-down) and selective attention. Major cortical areas include the superior parietal and frontal areas, including the intraparietal sulcus and frontal eye fields.
- *Auditory network:* used for auditory processing, includes the right and left primary auditory cortex, Heschl’s gyrus, lateral superior temporal gyrus and posterior insular cortex.
- *Visual network:* whose cortical areas most involved are the lateral and superior occipital gyrus and the lingual gyrus.

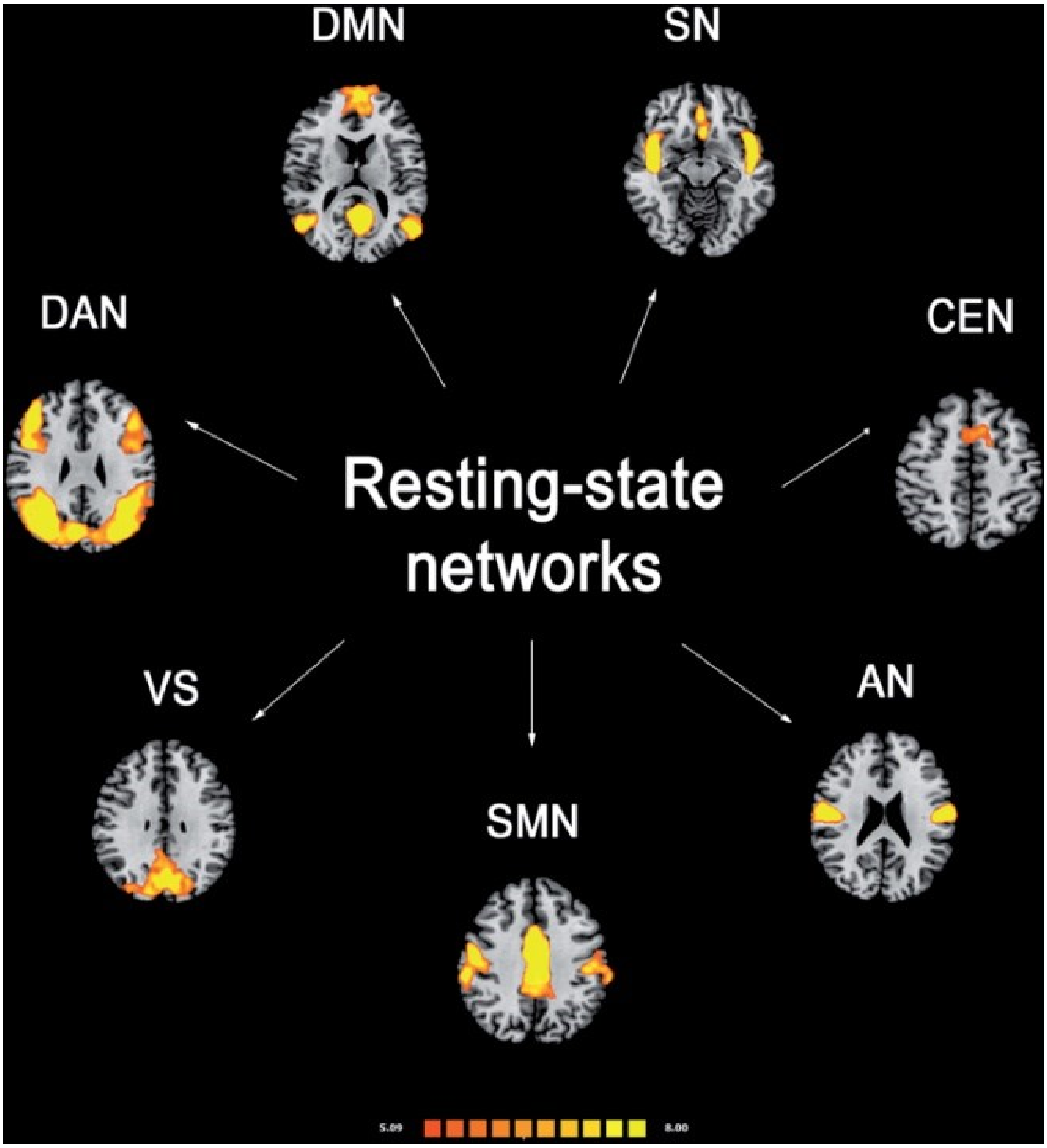

Figure 1.1 - Resting-state functional connectivity networks most widely reported in healthy controls shown in axial view. Colors represent percent change in BOLD signal superimposed on mean anatomical images in standard space. DMN, default-mode network; SN, salience network; CEN, central executive network; DAN, dorsal attention network; SMN, sensorimotor network; VS, visual network; AN, auditory network. [9]

1.2.4 Multi-Echo fMRI Technique

In recent years, studies have revealed that functional MRI data are susceptible to various artifacts, such as subject head motion, cardiac and respiratory effects, and hardware issues. These artifacts have raised concerns about the reliability of fMRI results, particularly in the context of brain function and developmental studies: the presence of artifacts not only reduces the statistical power of fMRI investigations, but also contributes to spurious results, leading to a crisis over confidence in fMRI research.[10]

Multi-Echo fMRI (ME-fMRI) has emerged as a promising approach to improve the fidelity of fMRI signals through physically guided determination of their origins, whether derived from BOLD contrast or artifact sources.[10]

Most echo-planar imaging (EPI) sequences collect a single image of the brain following a radio frequency (RF) pulse at a rate known as repetition time (TR). This typical approach is known as single echo fMRI, as well as standard fMRI. [a] Then, after excitation, standard fMRI uses 2-D echo planar imaging to acquire single-TE slice images, one slice at a time: at 3T, this TE is usually 30ms.[10]

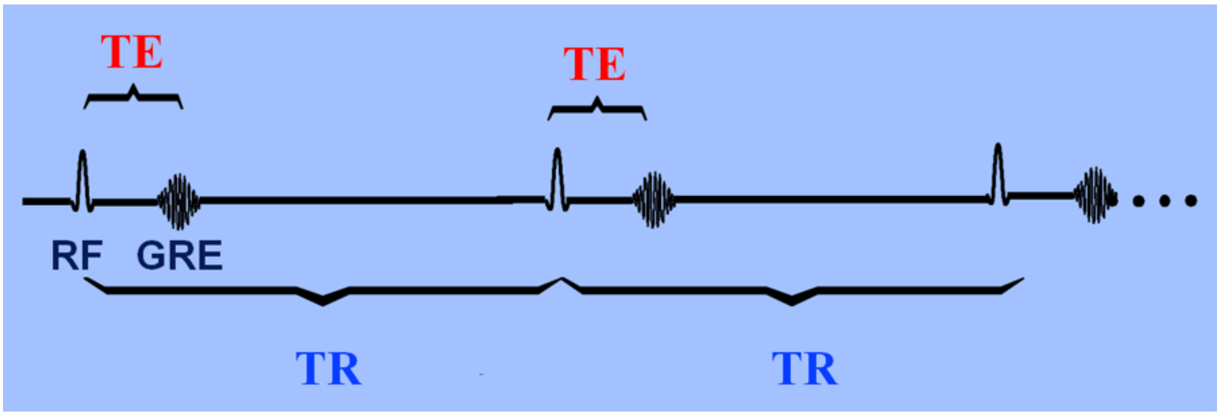

Figure 1.2 - TR and TE are basic parameters of the pulse sequence, typically measured in milliseconds (ms). Echo time (TE) represents the time between the center of the RF pulse and the center of the echo. For pulse sequences with multiple echoes between each RF pulse, different echo times (TE1, TE2, TE3, etc.) can be defined. The repetition time (TR) is the length of time between consecutive corresponding points on a repeated series of pulses and echoes. [11]

In contrast, ME-fMRI uses a slightly different approach: after a standard excitation pulse, a slice image is acquired at the first possible TE. Without re-excitation, another image of the same slice is acquired immediately afterwards, at a longer TE, and so on until the desired number of images and TEs is reached. This operation is performed for each slice of the brain volume.
Thus, unlike conventional single-echo fMRI, ME-fMRI acquires multiple images of the same slice at varying echo times after a single excitation pulse [10], thus achieving multiple volumes with varying contrast levels acquired per RF pulse. [a]

The fMRI signal contains important neural information (termed BOLD signal), but also “noise” (termed non-BOLD signal) caused by factors such as participant movement and changes in respiration.

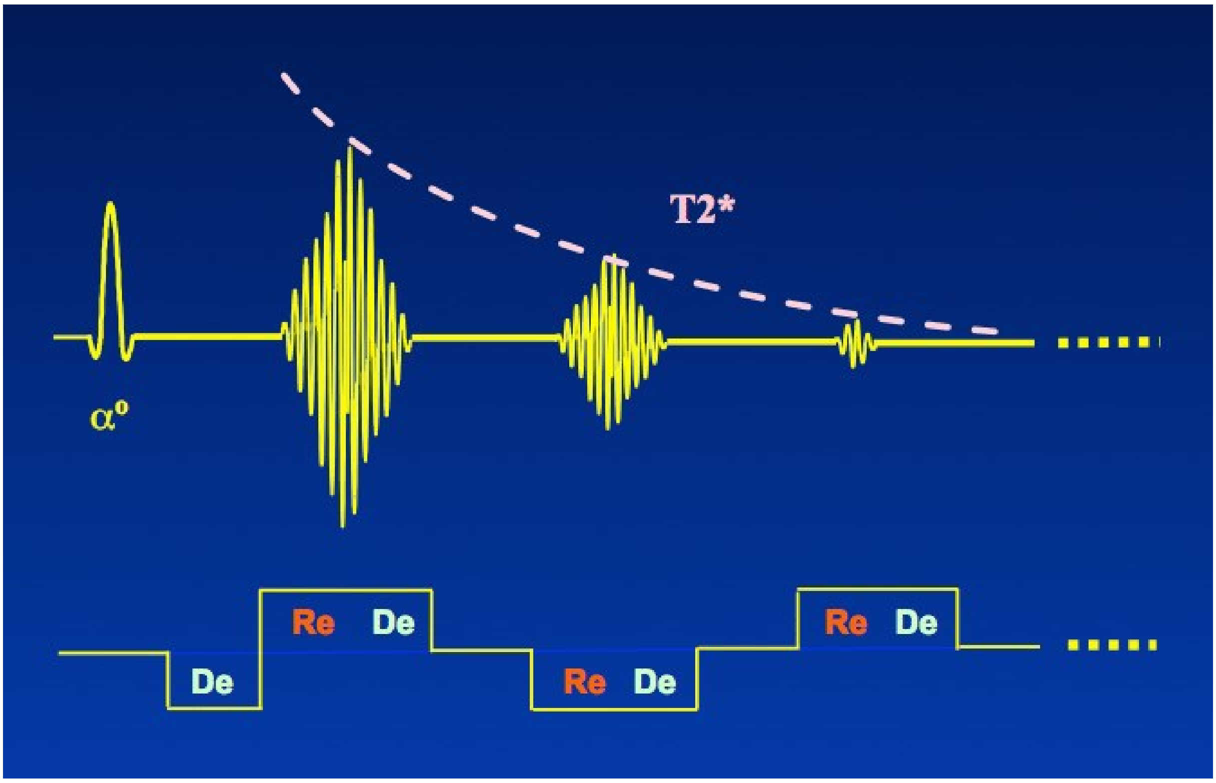

Figure 1.3 - Several echoes can be created after a single RF-pulse by sequential gradient reversals. Generating multiple GREs is possible as long as complete loss of the transverse magnetization by T2 relaxation has not yet occurred. The second half of the first upward gradient lobe dephases the signal (De). The first half of the second downward lobe rephases these spins (Re) and generates a second echo. The process may be repeated, but because of T2*-decay, the maximum usable number of echoes is only 3-4 in most cases. The echo times for each echo are different.* [12]

Multi-echo data collection provides valuable information on both BOLD and non-BOLD signals (noise): since the BOLD signal is known to decay at a predetermined rate, the collection of multiple echoes allows evaluation of the non-BOLD signal, which is crucial for denoising and improving signal quality.

The earliest echo time is the brightest, as the signal has had only a limited amount of time to decay, while the latter echo times show areas where the signal has decayed completely (“drop out”) due to magnetic field inhomogeneity. Using information from multiple echoes, these images can be optimally combined to exploit the signal from earlier echoes. [a]

1.2.4.1 Advantages of Multi-Echo fMRI [a]

There are several reasons for considering the use of multiple echo EPI (ME-EPI):

- *Comparison of echoes*: the ME-EPI allows individual single-echo time series to be analyzed separately and then compared, offering insights into changes in signal characteristics.
- *Improvement of signal-to-noise ratio (SNR)*: through weighted averaging of echoes (“optimal combination”), ME-fMRI achieves a higher signal-to-noise ratio (SNR) and

increases the statistical power of analyses, especially in regions prone to signal dropouts such as the orbitofrontal cortex, ventral temporal cortex or ventral striatum, which are characterized by low T2* values.

- *Enhancement of denoising*: the availability of multi-echo data allows the application of advanced denoising techniques, such as ICA-based denoising, including tedana, specifically designed for multi-echo data, enabling significant improvements in signal quality.

1.2.4.2 Costs and Benefits of Multi-Echo fMRI [a]

Several aspects should be considered before choosing to implement multi-echo fMRI:

- *Possible increase in TR*: The time cost of ME-fMRI is slightly higher than that of single-echo fMRI due to the acquisition of multiple echo times: while the shortest TE is essentially free (it is collected in the interval between the RF pulse and the single-echo acquisition) and the second one tends to roughly match the TE of the single echo, the additional echoes take longer. This needs to be evaluated in relation to other factors such as slice coverage, TR, and acceleration: if acceleration is increased, it is worth making an empirical comparison to ensure that there is not a nonnegligible loss of SNR or an increase in artifacts.
- *SNR improvement*: despite the time cost, weighted averaging of echoes to optimize T2* weighting can offer a reliable and beneficial increase in data quality.
- *Consider long-term data use*: if the dataset is intended for future analysis over an extended period, continued development of more powerful multi-echo denoising methods can add further value to the data.
- *Signal recovery in droupout areas*: multi-echo fMRI enables effective signal recovery in brain regions prone to droupout due to low T2* values, such as the orbitofrontal cortex, ventral temporal cortex, or ventral striatum, providing valuable information for research focusing on these specific areas.
- *Cost of quality control*: regardless of the fMRI approach chosen, performing thorough data quality control is essential. Therefore, this involves an investment of time and resources when examining denoising results.

1.3 Parkinson's Disease: Clinical and Neurobiological Aspects

Parkinsonism is a syndrome characterized by bradykinesia and rigidity, often caused by increased muscle tone. Parkinson's disease (PD) is the most common cause of Parkinsonism.

Specifically, Parkinson's disease is a chronic, idiopathic neurodegenerative disorder that primarily affects individuals aged 65 to 80 years, with a prevalence ranging from 0.25% to 4%.[13] It is the second most common neurodegenerative disorder and is characterized by a clinical tetrad of motor dysfunction, including resting tremor, rigidity, bradykinesia (reduction of movements), and loss of postural reflexes (in more advanced stages).[14]

However, PD is not defined solely by its motor symptoms; it also involves various non-motor symptoms (NMS) that can have a significant impact on the quality of life of those affected,[14] such as depression (caused by excessive inhibition of basal ganglia circuits) and dementia in the advanced stages.

1.3.1 Symptomatology

Pathologically, Parkinson’s disease is a multifaceted neurological disorder characterized by motor and nonmotor symptoms, the pathology of which involves the loss of nigrostriatal dopaminergic neurons and the presence of intraneuronal Lewy bodies, particularly in the ventrolateral and caudal segments of the substantia nigra pars compacta.

The substantia nigra consists of the pars compacta (SNpc), which serves primarily as an input to the basal ganglia circuit and supplies dopamine to the striatum, and the pars reticulata (SNpr), which serves primarily as an output, conveying signals from the basal ganglia to various brain areas.

The SNpc contains subgroups of dopamine-containing neurons, the so-called nigrosomes, of which nigrosome 1 is the largest, where in the PD there is the most pronounced dopaminergic leakage compared to other subregions of the SN.

In later stages of the disease, further lesions occur in non-dopaminergic brain areas.

Pathological changes in PD can be classified into three main areas: midbrain (involving loss of dopaminergic neurons), basal ganglia (associated with dopaminergic depletion), and cortical (related to functional reorganization). Collectively, these changes contribute to the complex motor and nonmotor symptoms observed in PD patients. [13]

1.3.1.1 Motor Symptoms

Degeneration of nigrostriatal dopaminergic neurons, resulting in disruption of basal ganglion-thalamus-cortical circuits, underlies the classic motor signs and symptoms of PD, such as tremors, reduced movement, and muscle rigidity [13] and can begin years or even decades before the onset of these typical motor symptoms, spreading throughout the nervous system.[9]

In Parkinson's, tremor is characterized by oscillatory and rhythmic activity, brought about by alternating contractions of agonist and antagonist muscles.

The motor symptomatology typically seen in Parkinson's disease consists of a reduction in the amplitude of some movements (as in the case of finger tapping) and some presence of tremor: at the onset of the disease, it may occur asymmetrically (unlike in other Parkinsonisms) in the left hand.

There is also a reduction in the speed and frequency of execution of movements (assessed as the number of movements per unit time), especially in the prone-supination movement of the forearm and feet (dysdiadocokinesia).

These symptoms tend to become more pronounced as the disease progresses: in fact, the patient develops marked tremor in both hands, some anteroflexion of the trunk (which shifts the center of gravity forward and leads to the classic festinated gait of the Parkinsonian patient), axial rigidity during walking, and lacks pendular oscillatory movement of the upper limbs during the act of walking.

1.3.1.2 Non-Motor Symptoms

Parkinson's disease is not exclusively a pathology of dopaminergic cells: it also affects neurons that contain other neurotransmitters, such as norepinephrine, serotonin, and acetylcholine: it follows that the disease also affects other areas of the CNS and spinal cord.

In addition to the well-known motor symptoms, in fact, PD is characterized by various nonmotor features that play an important role,[13] as they can have a significant impact on the patient's quality of life and functional independence.[15]

These nonmotor features include cognitive deficits, hyposmia (reduced sense of smell), mood alterations, depression, psychosis, and behavioral and perceptual abnormalities.[15] Some nonmotor symptoms may even precede motor symptoms or emerge later as the disease progresses[11] , and may confer greater disability than motor symptoms: autonomic dysfunction, in particular, is common in people with PD and is known for its strong negative contribution to quality of life and its association with a poorer prognosis and survival..[17]

Depression, on the other hand, affects about 35% of PD patients and has been associated with decreased functioning, cognitive impairment, increased stress, and reduced quality of life. [15]

1.3.2 Disease Stages [16]

i. *Premotor or prodromal period*: complaints such as depression, anhedonia, hyposmia, constipation, and sleep disturbances may be present that precede the onset of classic motor symptoms (bradykinesia, rigidity, tremor, and loss of postural reflexes). Some early motor symptoms may be shoulder pain (frozen shoulder), difficulty getting up from a chair, or slowing of voluntary movements.

ii. *Time 0*: Degeneration of dopaminergic neurons is already underway in the premotor phase, but only when more than 50% of them are destroyed do the first motor symptoms, particularly bradykinesia, begin to appear, resulting in the diagnosis of the disease.

iii. *Early phase*: includes the first 7-10 years of the disease, when the main motor symptoms are observed, generally in the absence of complications due to therapy or cognitive in nature. The cornerstones of this phase are bradykinesia and mood alterations. However, complaints such as exhaustion, perceived heaviness of the feet, and inability to run may also occur. At this stage, therapy is usually already underway.

iv. *Advanced or late phase*: this is a phase in which cognitive disorders and non-motor disorders, particularly dysautonomic disorders (orthostatic hypotension and urinary dysfunction), prevail and severely affect the patient's quality of life. Complications, related to both cognitive dysfunction and side effects of therapy, are also observed in this phase.

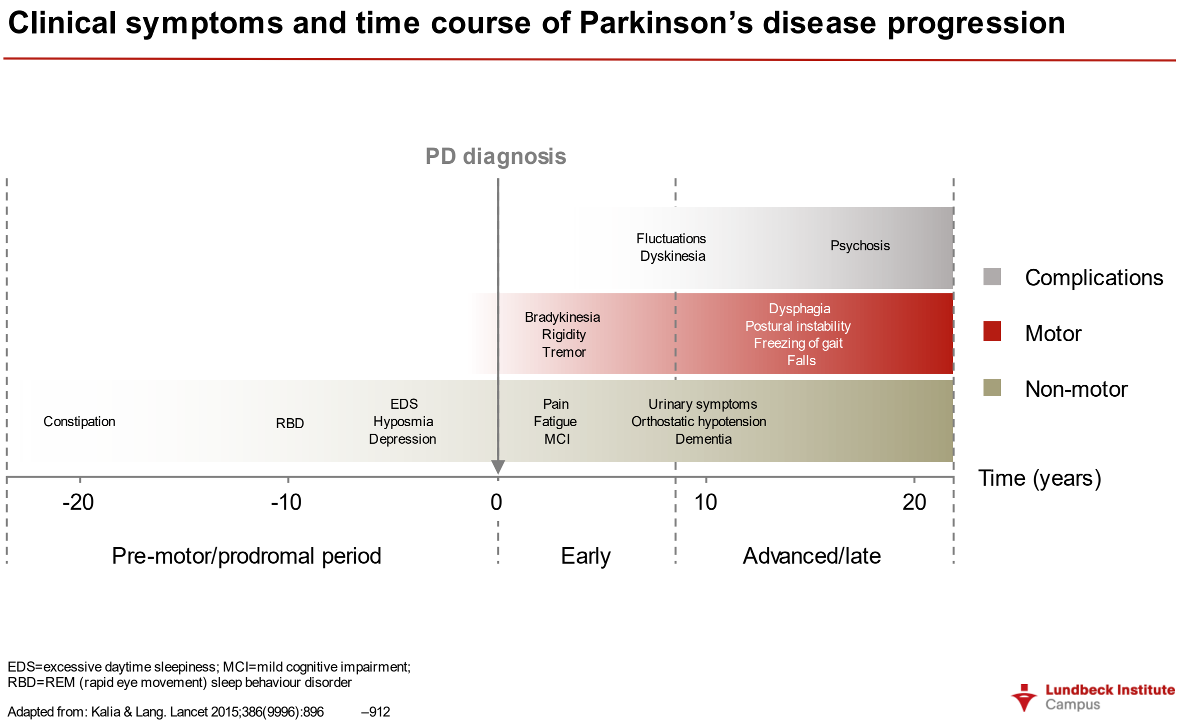

Figure 1.4 - Clinical symptoms and time course of Parkinson's Disease progression.

In addition to the symptomatology given by the disease itself, conditions associated with the disease may also occur: generally, after 7 to 8 years of therapy administration, problems related in part to the failure of the therapy may arise.
One of the main problems faced in the treatment of this disease is that of motor fluctuations, caused by an inconsistent concentration of dopamine in the brain: this is reflected in the patient's inability to perform consistent motor performances, presenting moments when they are significantly better and others when they are significantly worse.

So-called on-and-off moments can alternate suddenly and unpredictably throughout the day in the form of:

- *Wearing off*: this refers to the phenomenon observed when the dose of therapy fails. The drug takes effect for only a few hours, after which symptoms suddenly reappear until the next dose is taken. This phenomenon, called end-of-dose deterioration, is partly responsible for daily motor fluctuations.
- *Sudden switch-off or freezing*: the patient experiences motor blockade, sudden rigidity, so he or she cannot move.
- *Delayed onset*: the benefit from therapy occurs with some latency: thus, there is no early response, but delayed efficacy.
- *Variable response with meals*: if the dopaminergic therapy is derived from an amino acid taken in the diet (as in the case of Levodopa, or L-DOPA, which is derived from phenylalanine) intestinal absorption of the drug may be impaired: in the case where the meal is highly proteinic, the proteins in the meal will compete for the same amino acid transporters, consequently slowing absorption of the drug.
- *Yo-yo phenomenon*: random and unpredictable fluctuations unrelated to therapy.
- *Episodic lack of response to LD dose*.

In more advanced stages, in particular, the transition from moments of blocking (off) to moments of excessive and involuntary movement is even more pronounced.
These phenomena are called dyskinesias and are partly related to the therapy, partly to the neurodegeneration on which the therapy acts: they can lead to several negative consequences, such as falls and difficulty in performing gestures in a purposeful manner.
About 10 years after the disease, non-motor off phenomena, such as depression or anxiety, can also occur, due to dopamine deficiency in the brain.

1.3.3 Diagnosis

The clinical diagnosis of Parkinson's Disease is based on clinical evidence of motor signs [15]: in particular, it is based primarily on the presence of bradykinesia and at least one symptom among rigidity, tremor, and postural instability.[17] These manifestations may initially affect only one hemisphere of the body.

However, recent findings suggest that PD may also present with nonmotor symptoms already at onset, such as depression, orthostatic hypotension, and REM sleep phase disturbances, which have good associative evidence with the disease. On the other hand, some non-motor symptoms, such as anxiety, have weaker evidence of association.[14]

In the diagnostic work-up of patients with Parkinsonism, brain MRI is commonly used to assess structural anatomy and brain pathology.

In neurodegenerative pathology, it can help make a correct diagnosis, as it can identify patterns of structural degradation and assess cerebrovascular damage (found in vascular Parkinsonism), thus being important in differentiating PD from other causes of Parkinsonism such as multiple sclerosis, normal pressure hydrocephalus, or Wilson's disease. In addition, it may support the diagnosis of atypical neurodegenerative Parkinsonism.[13]

In addition, rs-fMRI can be used to assess regional interactions and functional connectivity in PD, focusing mainly on motor pathways.[13] Changes in functional connectivity, particularly involving cortico-striatal and mesolimbic-striatal dopaminergic circuits, provide valuable insights into the pathophysiological mechanisms underlying motor symptoms in PD. [9]

1.3.4 Therapy [16]

Once the dignosis of Parkinson's disease is firmly established, drug treatment is initiated. The most common drug therapies to address the disorder are:

- *Levodopa (L-DOPA)*: is the main treatment option for this disease and the most effective drug to date. It is an amino acid that is converted to dopamine in the CNS and goes to compensate for the lack of endogenous dopamine production in these patients. After crossing the blood-brain barrier, it is converted to dopamine by DOPA-decarboxylase (at the level of the synaptic terminals of dopaminergic neurons): the newly formed dopamine is released into the synaptic space to go on to bind to postsynaptic receptors.
- *Botulinum toxin (BoNT-A)*: acts at the level of nerve endings that innervate muscles, going to interfere with the release of a particular neurotransmitter: acetylcholine. Botulinum toxin is administered only parenterally, by injection.

1.3.5 Rating Scales

The degree of severity of the disease can be established through various rating scales. These scales, considering different items (motor and non-motor), assign the patient a score proportional to the severity of the disorder: the higher the score, the more advanced the disease.

1.3.5.1 MDS - Unified Parkinson's Disease Rating Scale

The most widely used scale is the MDS-UPDRS scale (Fig.1.5), which allows a common language about the severity of the disease in a specific patient and at a specific time in the course.[16]

The MDS-UPDRS is a revision of the Unified Parkinson's Disease Rating Scale (UPDRS), originally developed in the 1980s, certain aspects of which have been improved by the Movement Disorder Society (MDS).

The MDS-UPDRS was developed to assess various aspects of Parkinson's disease, including non-motor and motor experiences of daily living and motor complications. It includes a motor assessment and characterizes the extent and burden of the disease in various populations.[17]

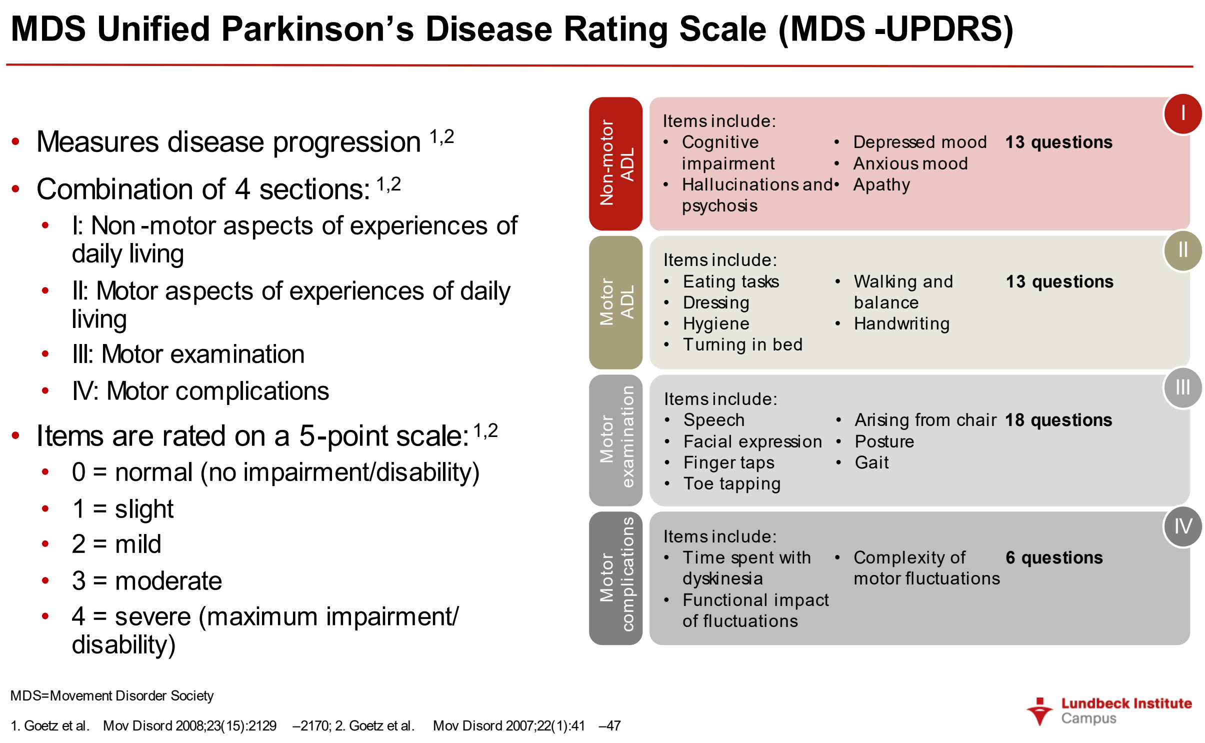

MDS Unified Parkinson's Disease Rating Scale (MDS -UPDRS)

- Measures disease progression [1,2]
- Combination of 4 sections: [1,2]
  - I: Non -motor aspects of experiences of daily living
  - II: Motor aspects of experiences of daily living
  - III: Motor examination
  - IV: Motor complications
- Items are rated on a 5-point scale: [1,2]
  - 0 = normal (no impairment/disability)
  - 1 = slight
  - 2 = mild
  - 3 = moderate
  - 4 = severe (maximum impairment/ disability)

I — Non-motor ADL
Items include:
- Cognitive impairment
- Hallucinations and psychosis
- Depressed mood
- Anxious mood
- Apathy

13 questions

II — Motor ADL
Items include:
- Eating tasks
- Dressing
- Hygiene
- Turning in bed
- Walking and balance
- Handwriting

13 questions

III — Motor examination
Items include:
- Speech
- Facial expression
- Finger taps
- Toe tapping
- Arising from chair
- Posture
- Gait

18 questions

IV — Motor complications
Items include:
- Time spent with dyskinesia
- Functional impact of fluctuations
- Complexity of motor fluctuations

6 questions

MDS=Movement Disorder Society

1. Goetz et al. Mov Disord 2008;23(15):2129 –2170; 2. Goetz et al. Mov Disord 2007;22(1):41 –47

Lundbeck Institute Campus

Figure 1.5 - MDS - Unified Parkinson's Disease Rating Scale with related assessment criteria and scoring scales.

1.3.5.2 Hoehn & Yahr Scale

There is also a disease staging scale: the Hoehn & Yahr scale (Fig.1.6), commonly used to describe the symptoms of Parkinson's disease progression. It was originally published in 1967 in the journal Neurology by Melvin Yahr and Margaret Hoehn and included stages 1 to 5, where stage 5 indicates the terminal stage, with a severe reduction in the patient's autonomy.

A modified scale was then proposed, with the addition of stages 1.5 and 2.5 to describe the intermediate course of the disease. [18,19]

A stage 0, corresponding to the absence of signs and symptoms, may also be included.[16]

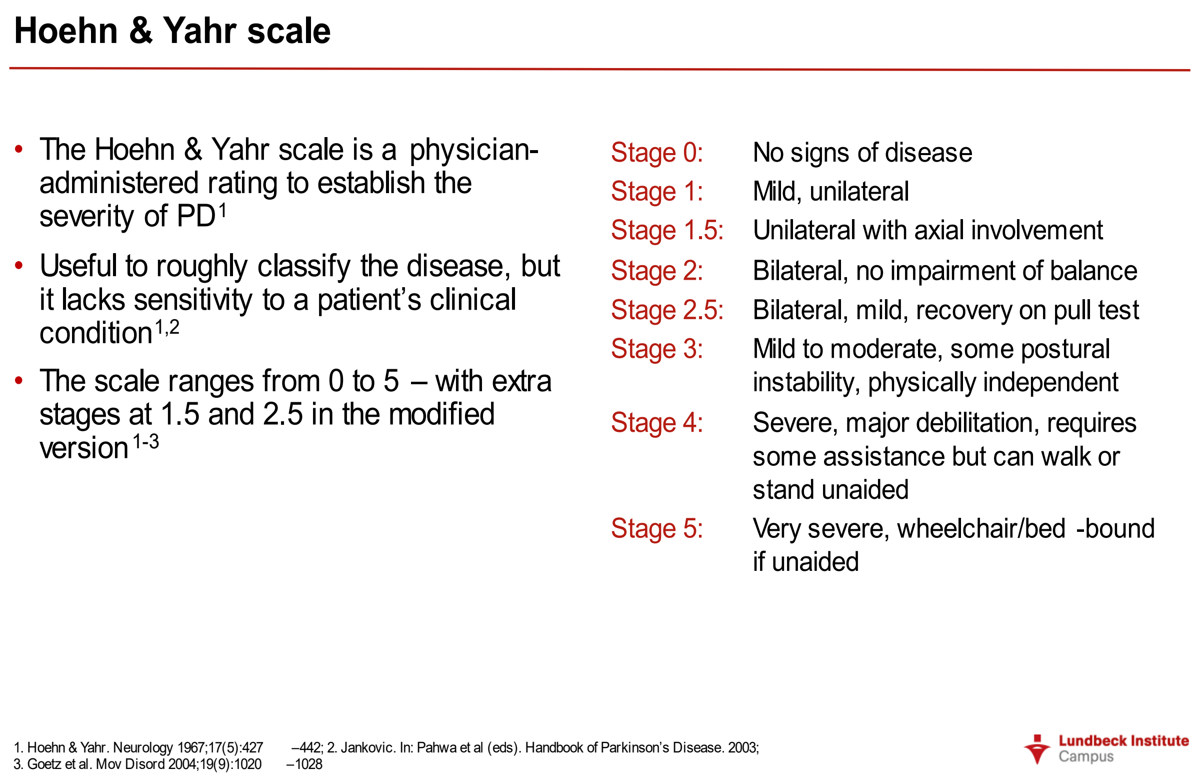

Hoehn & Yahr scale

- The Hoehn & Yahr scale is a physician-administered rating to establish the severity of PD[1]
- Useful to roughly classify the disease, but it lacks sensitivity to a patient's clinical condition[1,2]
- The scale ranges from 0 to 5 – with extra stages at 1.5 and 2.5 in the modified version[1-3]

Stage 0:	No signs of disease
Stage 1:	Mild, unilateral
Stage 1.5:	Unilateral with axial involvement
Stage 2:	Bilateral, no impairment of balance
Stage 2.5:	Bilateral, mild, recovery on pull test
Stage 3:	Mild to moderate, some postural instability, physically independent
Stage 4:	Severe, major debilitation, requires some assistance but can walk or stand unaided
Stage 5:	Very severe, wheelchair/bed -bound if unaided

1. Hoehn & Yahr. Neurology 1967;17(5):427 –442; 2. Jankovic. In: Pahwa et al (eds). Handbook of Parkinson's Disease. 2003;
3. Goetz et al. Mov Disord 2004;19(9):1020 –1028

Lundbeck Institute
Campus

Figure 1.6 - Hoehn & Yahr scale with related assessment criteria and scoring scales.

1.4 Previous Studies on Functional Connectivity in Parkinson's Disease

Neuroimaging techniques, particularly functional magnetic resonance imaging (fMRI), have been widely used to study the pathophysiology of neurodegenerative disorders such as Parkinson's disease (PD), providing valuable insights into its pathophysiological changes, potential treatments, and progression-related changes.[10]

In cohorts of PD patients, advanced MRI techniques, including functional connectivity (FC) analysis, have shown promise in providing additional diagnostic markers for early-stage PD, as demonstrated by diffusion changes in the orbitofrontal region in the pre-motor phase of PD. [13]

Resting-state functional magnetic resonance imaging (rs-fMRI) represents a powerful tool for studying depression-associated network abnormalities in PD patients, as it allows characterizing spontaneous brain activity and identifying brain networks with co-variant patterns, without the need to perform specific tasks: depressed patients with PD showed increased spontaneous regional neural activity in the orbitofrontal area and decreased functional integration within the prefrontal-limbic network, compared with non-depressed patients and healthy controls.[14]

Lou et al. (2015) also showed that depressed patients with PD exhibit decreased FC in the left dorsolateral prefrontal cortex and right superior temporal gyrus, and increased FC in the right posterior cingulate cortex (PCC), compared with non-depressed patients.

Furthermore, specific patterns of functional coupling/decoupling between resting state networks (RSNs) have been observed in PD patients, particularly within neurocognitive networks critical for efficient behavioral and cognitive performance.[9]

A recent meta-analysis by Helmich et al. found reduced coupling between the posterior putamen and the inferior parietal cortex in PD, demonstrating that reduced functional connectivity within the posterior putamen and its severity correlate with PD symptoms.[11] This subcortical area and its cortical projections are modulated by levodopa administration.[9]

In contrast, the anterior putamen showed increased connectivity with the inferior parietal cortex, a finding interpreted as compensatory: indeed, these results suggest that dopamine depletion in PD leads to a remapping of brain connectivity, affecting the sensorimotor circuitry and sensorimotor integration.

Thus, changes in functional connectivity are associated with tremor in PD: given also the increased functional connectivity in the cerebellothalamic circuit of internal globus pallidus and putamen and the correlation of dopamine depletion of the globus pallidus to the severity of clinical tremor, the presence of pathological interactions between the basal ganglia and the cerebellothalamic circuit in patients with tremor-dominant PD is inferred.[13]

Rs-fMRI literature supports that aberrant functional interaction within corticostriatal loops may represent a potential early biomarker of PD-related neurodegeneration, even in subjects at high risk of developing clinical PD.
Longitudinal studies have also revealed compensatory effects and treatment-related changes during disease progression: an increase in resting-state functional connectivity within the primary motor cortex (M1) has been demonstrated in PD patients. This increase in connectivity may in fact represent a compensatory response of networks to local neuronal injury, allowing the same global performance to be maintained, or a loss of dynamic network properties. [9]

Postmortem and molecular imaging studies have provided fundamental insights into alterations in dopaminergic and nondopaminergic neurotransmission within the hypothalamus in the early and late stages of PD. However, more generally, the autonomic dysfunction observed in PD may reflect alterations in functional communication between the hypothalamus and other regions involved in the regulation of autonomic function.[20]

Overall, fMRI and rs-fMRI studies have contributed significantly to the understanding of PD pathophysiology and potential biomarkers for early diagnosis and monitoring of disease progression. However, further research is needed to resolve inconsistencies between studies and better understand the complexity of the disease.[9]

1.5 Existing Approaches for Preprocessing Resting-State fMRI Data

Before subjecting raw fMRI data to any kind of statistical analysis, some crucial preprocessing steps are commonly performed to ensure the quality and reliability of subsequent analyses.

1.5.1 Typical rs-fMRI data Preprocessing Steps [a][b]

To ensure the reliability and accuracy of rs-fMRI data, a series of basic preprocessing steps are usually performed:

1.5.1.1 Evaluation of data quality

As a first step, individual aberrant slices in the fMRI acquisition are identified and excluded: these slices may be affected by random variations in signal intensity, such as noise spikes, appearing too bright or too dark, or containing artifacts. These can arise from physiological sources (patient motion, breathing, heart rate, anxiety, drowsiness, medications) or from the scanner itself (field inhomogeneities, eddy currents, gradient heating, electronics). Timely identification and exclusion of these problematic slices, a process also known as “scrubbing”, are critical to avoid potential deterioration of the entire experiment. This can be done through visual inspection of the starting images in montage mode, or by resorting to more sophisticated graphical and semi-automatic methods.

1.5.1.2 Slice Timing Correction

In most fMRI studies, slices are acquired one at a time, resulting in differences in the timing of slice acquisition: the signal recorded from one slice may be offset in time by up to several seconds from another. The situation is further complicated depending on whether slices were acquired in sequential order (1,2,3,4,5,6...) or interleaved (1,3,5...2,4,6...) and whether simultaneous multislice imaging was used. This carries the risk of introducing errors, especially in rapid, event-related fMRI studies; therefore, it is critical to correct for differences in slice timing to ensure accurate results.

Two basic strategies are generally used to correct slice timing:

- *Data shifting*: is the most used method, in which recorded points are shifted to reflect their correct offset relative to the time of the stimulus. An interpolation of the points is made to fit the fixed TR-based timing grid, thus producing some blurring and degradation of the data.

- *Model shifting*: the predicted position of the hemodynamic response function (HRF) is varied, treating the slice position as an additional independent variable in the subsequent statistical analysis. Sometimes, to improve accuracy, time derivatives of the HRF are also incorporated into the model.

1.5.1.3 Motion Correction

Head movement is a major source of error in fMRI studies, requiring the development of various strategies to deal with this problem: head restraint by padding and straps is essential, and more rigid restraints such as bite bars and masks are sometimes used. Training and education of subjects before imaging are also important.

Prospective motion correction can be performed using echo navigators, but retrospective motion correction where the head is treated as a rigid body with three directions of translation (displacement) and three axes of rotation is more common. Having chosen a single functional volume in a run as a reference, each volume is aligned to this by an iterative procedure to minimize a cost function (as the mean-squared difference). Visualization of the rotation and translation parameters provides valuable insight into the effects of motion.

1.5.1.4 Distortion Correction

The fMRI/BOLD sequences acquire gradient echoes and are therefore sensitive to magnetic inhomogeneity (T2*) effects, resulting in spatial distortions and signal dropouts, especially near the skull base and in regions such as the anterior frontal and temporal lobes. Techniques such as field mapping and "unwarping" methods are available to mitigate these distortions: although they are essential for sophisticated neuropsychological experiments, they are not as commonly used in mapping the baseline eloquent cortex for clinical fMRI studies.

1.5.1.5 Temporal Filtering

fMRI data often exhibit slow drift of the baseline signal over time and rapid fluctuations due to noise. Detrending, i.e., removal of low-frequency drift, can be carried out using a high-pass filter after the Fourier transform or time-domain averaging methods. Alternatively, confounding predictors, such as a discrete cosine transform basis set, can be added later in the data analysis to account for low-frequency fluctuations to remove gradual drifts.

High-frequency signal fluctuations (noise) can instead be removed through a low-pass filter, but this is generally not recommended for most studies because it can bias the estimation of individual HRFs and reduce the fMRI signals of interest.

1.5.1.6 Spatial Smoothing

Spatial smoothing consists of averaging the signals of adjacent voxels: it improves the signal-to-noise ratio (SNR) but reduces the spatial resolution by blurring the image and smeared activated areas in adjacent voxels. However, this process is justified by the fact that neighboring brain voxels are often intrinsically related in terms of function performed and blood supply.

For spatial smoothing, Gaussian filters are commonly used to convolve ("multiply") the fMRI data: a weighted average of the signals from neighboring voxels is computed, with weights decreasing with increasing distance from the target voxel.

The choice of optimal kernel size takes into account several factors, such as slice thickness, in-plane resolution, and the need to spatially separate small regions of activation. In general, a full-width half-maximum (FWHM) value of about 4-6 mm is preferred for single-subject studies and 6-8 mm for multi-subject analyses.

1.5.2 Available Software for rs-fMRI Data [a][c]

In fMRI data analysis, most major MRI manufacturers offer basic integrated software for fMRI processing (e.g., GE's BrainWave and Philips' I View BOLD), sufficient for fMRI studies based on simple tasks used for clinical cortical mapping.

However, more complex experiments require third-party solutions: many software programs are free and open source, and can provide robust toolsets for experimental design, data processing and analysis. Among the most widely used independent fMRI software, those of interest for this discussion are:

- *AFNI (Analysis of Functional Neuroimaging)*: is a large collection of free C-based programs for processing, analyzing and visualizing fMRI data. Originally developed by Robert Cox at the Medical College of Wisconsin in the mid-1990s, AFNI is now housed at the National Institute of Mental Health (NIMH) in Bethesda, MD. Additional tools include a skull removal program and SUMA for cortical surface-based fMRI analysis. It runs on Unix, SGI, Solaris, Linux, and Mac OS X.

- *FSL (FMRIB Software Library)*: is a suite of free applications from the Functional Magnetic Resonance Imaging of the Brain (FMRIB) laboratory at the University of Oxford. The first version of this software was released in 2000, and FSL has continued to grow exponentially since then. It is designed primarily for Mac OS X and Linux but can also be used on Windows in a virtual machine environment. The most widely used modules include FEAT (a model-based analysis for task-based fMRI), MELODIC (a model-free ICA-based analysis for resting-state fMRI), BET (for brain extraction), FAST (for tissue segmentation) and MCFLIRT (for motion correction). Tools are also available for tractography and diffusion analysis, as well as ASL-based perfusion and fMRI measurements.

- *SPM (Statistical Parametric Mapping):* was created in the late 1980s by Karl Friston to analyze PET images at the voxel level. Within five years, SPM became the dominant method for analyzing PET and fMRI data (an emerging technique at the time). Today SPM is in its 12th version under continuous development by members and collaborators of the Wellcome Trust Centre for Neuroimaging at University College London. SPM is free and runs on Windows, Linux, and Mac OS X provided the MATLAB core is installed. SPM has all the necessary functionality for processing, analyzing and visualizing fMRI data: like most other fMRI software, SPM uses the General Linear Model (GLM) for its main analysis, since Friston was an early proponent of this technique.

- *Brain Connectivity Toolbox*: contains over 120 statistical and brain connectivity functions designed primarily for complex network analysis (graphs) and is widely used to analyze resting-state fMRI studies. This free site is the work of several researchers, mainly Olaf Sporns of Indiana University and Mikail Rubinov of Cambridge. MATLAB installation is required, although some functions may run on Octave.

- *tedana (TE-dependent analysis)*: is a Python library for denoising multi-echo functional magnetic resonance imaging (fMRI) data. tedana originally began as part of the ME-ICA pipeline, although it has since differentiated itself: whereas the ME-ICA pipeline originally performed both pre-processing and TE-dependent analysis of multi-echo fMRI data, tedana now assumes that one is working with data that have been previously pre-processed.

Chapter 2: Materials and Methods

2.1 Dataset Characteristics

The dataset used in this study includes magnetic resonance imaging (MRI) scans of a group of 105 subjects with Parkinson's disease (PD) and 63 healthy control individuals (HC).
The scans were acquired at the San Camillo Hospital Institute using a magnetic imaging system manufactured by Philips using the Ingenia_CX model, with a magnetic field of 3 Tesla and an imaging frequency of 127,759 Hz. During the MRI imaging sessions, subjects were in a resting state, keeping their eyes open and without a specific target to focus on. Before the start of the acquisitions, the patients' attention was called, and their vigilance state was checked.

For each subject, data are available regarding both the anatomical structure of the brain (using T1w3D, T2w3D, and FLAIR3D sequences) and brain function during the resting state, including processes related to blood oxygenation. Specifically, data are available on the BOLD signal acquired using three different echo times (TE): 10 ms, 20 ms and 30 ms, with a repetition time (TR) of 2 seconds.
The image slices were acquired in interspersed order with phase coding in the antero-posterior direction using the SENSE technique with an acceleration factor of 3.3.
In addition, for a volume of data associated with the third echo time, acquisitions of the BOLD signal are available in both the antero-posterior direction (AP sequence) and the postero-anterior direction (PA sequence). This was done to allow correction of magnetic field distortions.

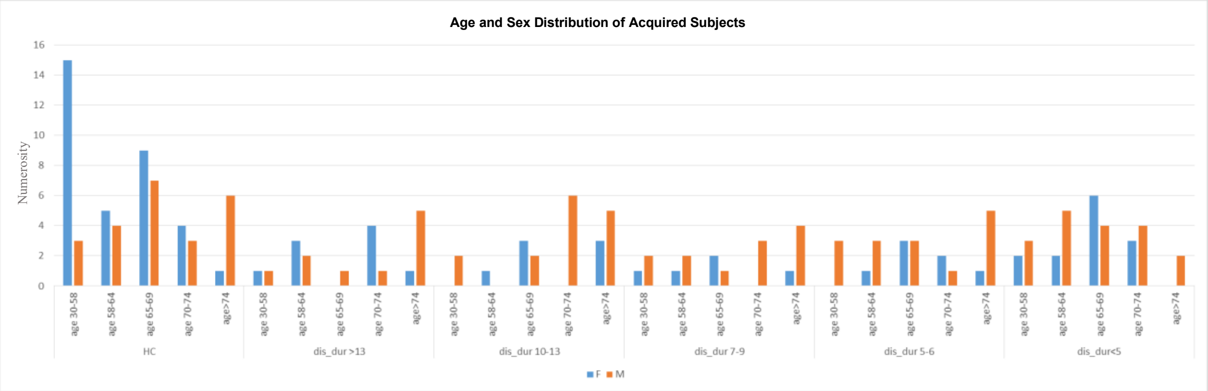

Figure 2.1 - Distribution by sex (females in blue and males in orange) and age in the cohort of healthy subjects (HC) and patients with Parkinson's disease (stratified by duration of the disorder, dis_dur).

Healthy controls and patients underwent the same clinical, behavioral, and cognitive assessment protocol. As shown by the similarity of age and sex distributions between the two cohorts in

Fig. 2.1 on the previous page, healthy subjects cover the same age range as the sample of subjects with Parkinson's disease.

Detailed information on symptoms manifested at disease onset and cognitive status of the participants was also made available (Fig. 2.2 below). it is possible to identify, from a cross-sectional perspective, healthy versus Mild Cognitive Impairment (MCI) subjects in the healthy cohort and all three cognitive states in the cohort of subjects with Parkinson's disease (dementia, MCI at two levels of severity, and no MCI).

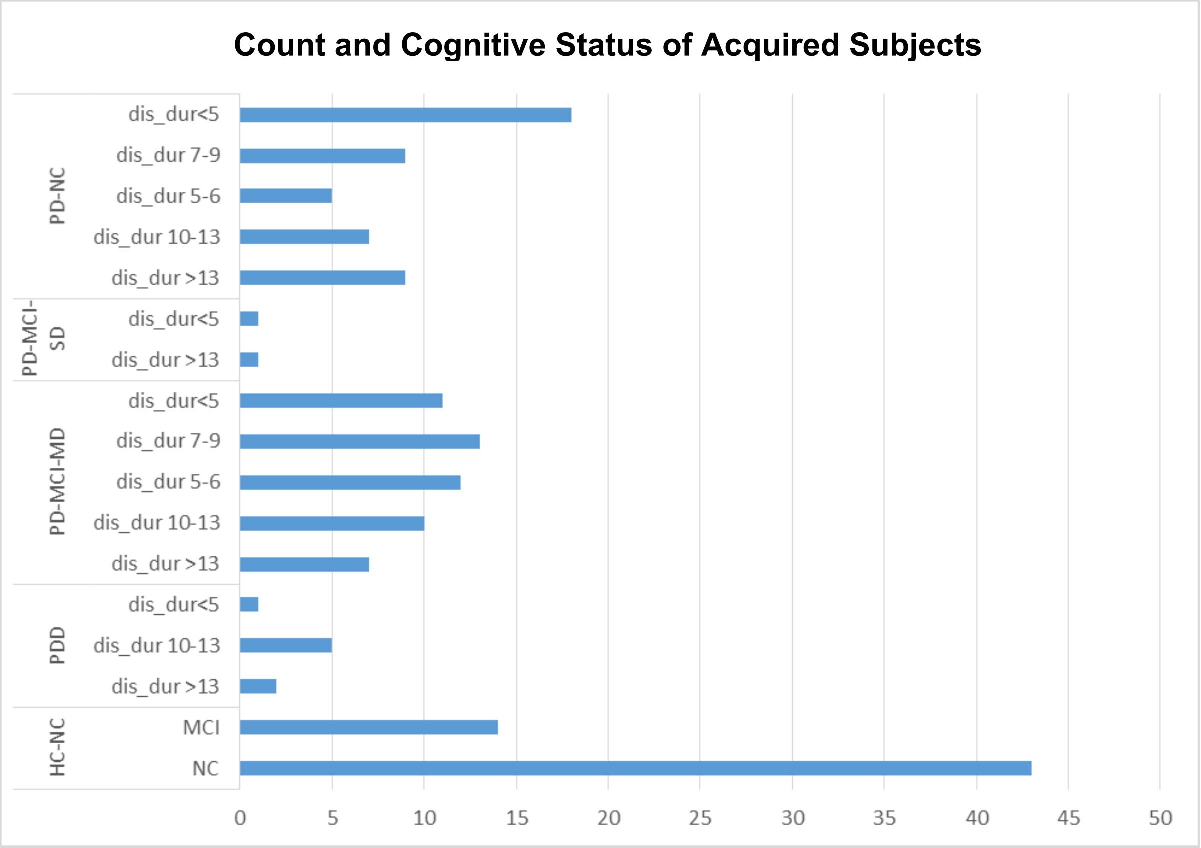

Figure 2.2 - Information regarding the numerosity (y-axis) and cognitive status (x-axis) of the subjects in the dataset. For the cohort of healthy subjects (HC) the condition of Mild Cognitive Impairment is indicated with HC-MCI and with NC-MCI the condition of No Cognitive impairment. In the cohort of subjects with Parkinson's disease (PD), the condition of Dementia is indicated with D, the condition of Mild Cognitive Impairment-Major Depression with PD-MCI-MD, the condition of Mild Cognitive Impairment-Severe Depression with PD-MCI-SD, and the condition of No Cognitive Impairment with PD-NC. For PD patients, the duration of the disorder (dis-dur) is also indicated.

From this data set, a 70-year-old healthy subject and a 60-year-old patient with Parkinson's disease, both with an MMSE score of 30, were considered to fine-tune the data preprocessing pipeline.

2.2 Development of the Preprocessing Pipeline

2.2.1 AFNI: Slice timing and Motion Correction

TASK	TOOL	COMMAND	OPTIONS
MOTION PARAMETER ESTIMATION	AFNI	*3dvolreg*	motion parameters estimated on the third echo: -1Dfile saves them in a text file, -1Dmatrix_save saves the transformation matrices for each volume
SLICE TIMING	AFNI	*3dTshift*	-tpattern specifies the slice acquisition pattern (altplus indicates an alternate acquisition pattern, beginning with an even slice)
MOTION CORRECTION	AFNI	*3dAllineate*	-1Dmatrix_apply to apply the estimated motion parameters on each echo
AFNI TO NIFTI DATA FORMAT CONVERSION	AFNI	*3dAFNItoNIFTI*	converts BRIK data (data from the image itself in compressed binary format) to NIfTI format

Table 2.1 - commands used to implement slice timing and motion correction in AFNI.

In the context of multi-echo EPI (ME-EPI) data analysis, it is essential to follow several preprocessing steps to ensure accurate results: among these, slice timing and motion correction emerge as crucial steps.

In fMRI data acquisitions, two-dimensional pulse sequences are often used to collect images one slice at a time. This means that during a single repetition time (TR), several slices are acquired at temporally distinct times. This temporal variation can become a significant problem, especially when longer TRs are used. Therefore, discrepancies in the acquisition times of different slices must be addressed and corrected.

In parallel, another critical aspect is motion correction: this stage aims to align the time series of images so that the brain is consistently positioned in each image. This correction is critical to ensure that variations in head or brain position between different acquisition times do not compromise the accuracy and interpretation of the analysis results.[21]

One prominent software for analyzing and visualizing functional MRI data is AFNI: it is open source and was initially created in 1994 to meet the needs of researchers at the Medical College of Wisconsin. Initially focused on mapping activations in the Talairach-Tournoux coordinate system, AFNI has evolved over time into a comprehensive tool for analyzing fMRI data. One of the main strengths of AFNI is its flexibility and transparency.

In recent years, further improvements have been made to the user experience of the fMRI data processing flow in AFNI, including the introduction of "super-scripts" that simplify the entire analysis process and the addition of graphical interfaces to manage these operations intuitively.[22]

AFNI's *3dvolreg* software was used to estimate the movement parameters. The algorithm is based on iterating linearized weighted least squares to make each sub-brick as similar as possible to the base brick. The resulting parameters (Fig. 2.3 and Fig. 2.4 on the following page) from the motion correction process include information on translations and rotations of the subject's head during image acquisition: translations refer to movements along the spatial axes (x, y and z), while rotations refer to changes in orientation around the same axes. Describing the small movements of the head during image acquisition is essential to the quality of the data: they are crucial in compensating for any unwanted movement, ensuring that volumes are aligned with each other correctly. The -1Dfile option of *3dvolreg* saves these parameters in a text file, while the -1Dmatrix_save option saves the transformation matrices for each volume.[d]

For slice timing correction, AFNI's *3dTshift* is used, which shifts the voxel time series from the input dataset so that the separate slices are aligned to the same time origin. The -tpattern parameter specifies the slice acquisition pattern: in the case of an alternative acquisition pattern, starting with an even slice, the 'altplus' option is used.[e]

Finally, motion correction is performed using AFNI's *3dAllineate*. The estimated motion parameters can be applied to each echo using the -1Dmatrix_apply option. This step ensures alignment between the different echoes in the dataset.

To maintain preprocessing consistency, it is recommended to apply the same motion correction transformation to all echoes. [a] This approach avoids possible shifts in the mean or voxelwise scale that could affect subsequent analyses. Instead of calculating and applying the head motion correction parameters to individual echoes, it is therefore advisable to calculate these parameters from one echo and apply the resulting transformation to all echoes.[a] The motion parameters were estimated on the echo closest to T2, i.e. the third echo (TE=30 ms).

Slice timing correction is essential prior to multi-echo denoising with tools such as tedana. This correction makes it possible to assume synchronous events between the different slices. If the repetition time (TR) is 1 second or more, slice timing correction must be performed before applying tedana. This correction is particularly important for multi-echo datasets, where differences in timing between echoes can affect the results. Furthermore, it is essential to maintain consistent slice timing between all echoes. Since the slice timing is defined as the time of the excitation pulse for each slice, it remains constant regardless of the timing of the echo. Therefore, it is recommended to use the same slice timing for all echoes in a ME-EPI series, otherwise differences in slice timing may affect the echo-dependent estimates. [a] [23]

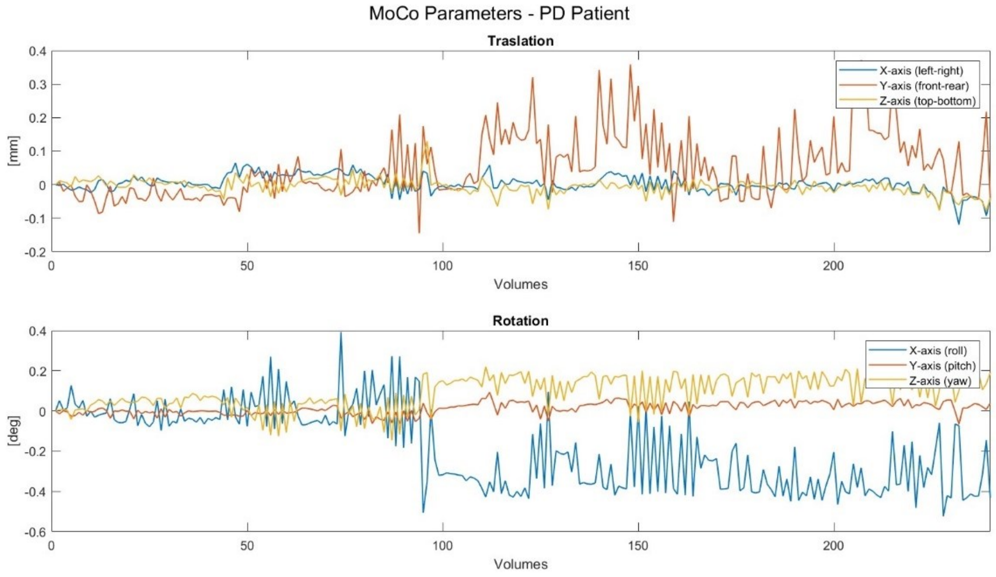

Figure 2.3 - Motion parameters (MoCo) estimated by the 3dvolreg command of AFNI in the third echo (TE=30ms) acquired in the patient with Parkinson's disease. The first 3 parameters refer to translation in mm (top graph) along the x-axis (left-right, in blue), y-axis (front-rear, in red), z-axis (top-bottom, in yellow) respectively. The second 3 parameters refer to rotation in degrees (bottom graph) along the x-axis (roll, in blue), y-axis (pitch, in red), z-axis (yaw, in yellow).

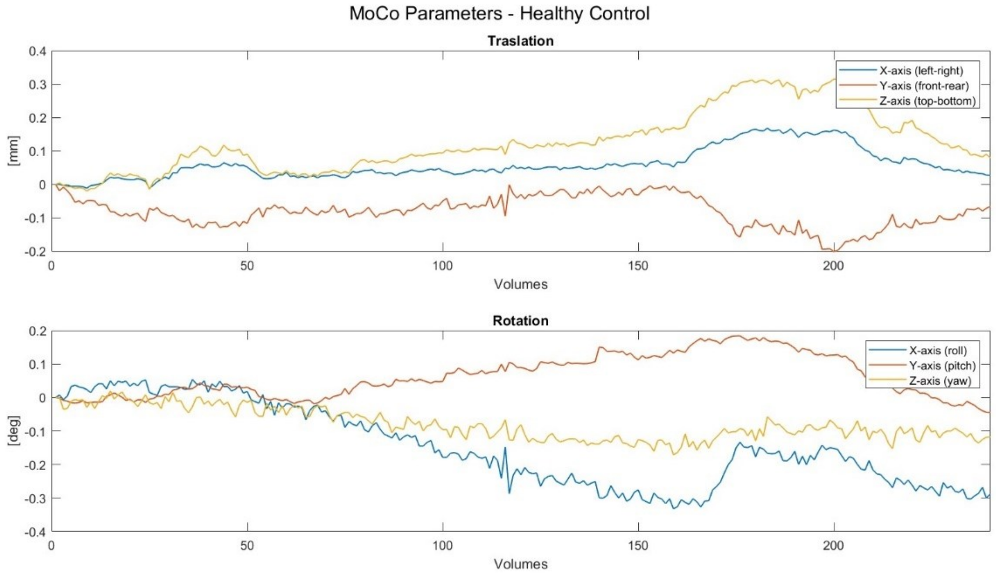

Figure 2.4 - Motion parameters (MoCo) estimated by the 3dvolreg command of AFNI in the third echo (TE=30ms) acquired in the healthy control. The first 3 parameters refer to translation in mm (top graph) along the x-axis (left-right, in blue), y-axis (front-rear, in red), z-axis (top-bottom, in yellow) respectively. The second 3 parameters refer to rotation in degrees (bottom graph) along the x-axis (roll, in blue), y-axis (pitch, in red), z-axis (yaw, in yellow).

2.2.2 Tedana: Optimal Combination of Echoes [a]

TASK	TOOL	COMMAND	OPTIONS
ECHOES COMBINATION	tedana	*t2smap*	echoes optimal combination (without denoising)

Table 2.2 - commands used to implement the optimal combination of echoes in tedana.

Tedana is a data processing technique used to decompose multi-echo Blood Oxygen Level Dependent (BOLD) data through the application of principal component analysis (PCA) and independent component analysis (ICA). This method aims to identify components of the data that exhibit TE-dependent (echo time) and TE-independent characteristics. Components that exhibit TE-dependent behavior are classified as BOLD, while those that exhibit TE-independence are considered non-BOLD and are removed as part of data cleaning.
In the approach implemented by tedana, time series data acquired from all echo times (TE) collected are merged and subjected to decomposition. This process leads to the identification of components that can be classified as BOLD or non-BOLD.

In the specific context discussed, tedana was used only to optimally combine the three echoes, with the goal of obtaining a single functional magnetic resonance imaging (fMRI) signal. The optimal combination is achieved through a series of steps that include:

- Monoexponential decay model fit
- Adaptive mask generation
- Optimal combination

2.2.2.1 Monoexponential Decay Model Fit

The main step involves fitting a mono-exponential decay model to the data. This model helps to estimate voxel-specific values of T2* and S0, where T2* represents the rate of signal decay over time, affecting aspects such as signal dropout and BOLD sensitivity, while S0 indicates the initial signal intensity within a voxel before decay (reflecting coil sensitivity).

Since T2* and S0 naturally fluctuate over time, estimating them on a volume-by-volume basis with a limited number of echoes produces noisy results, so the average maps of T2* and S0 are considered. To facilitate model fitting, tedana performs logarithmic transformation of the BOLD data using $\log(|S|+1)$, where S denotes the BOLD signal and echo times are multiplied by -1. A linear regression is then applied to the transformed data to obtain a simple line.

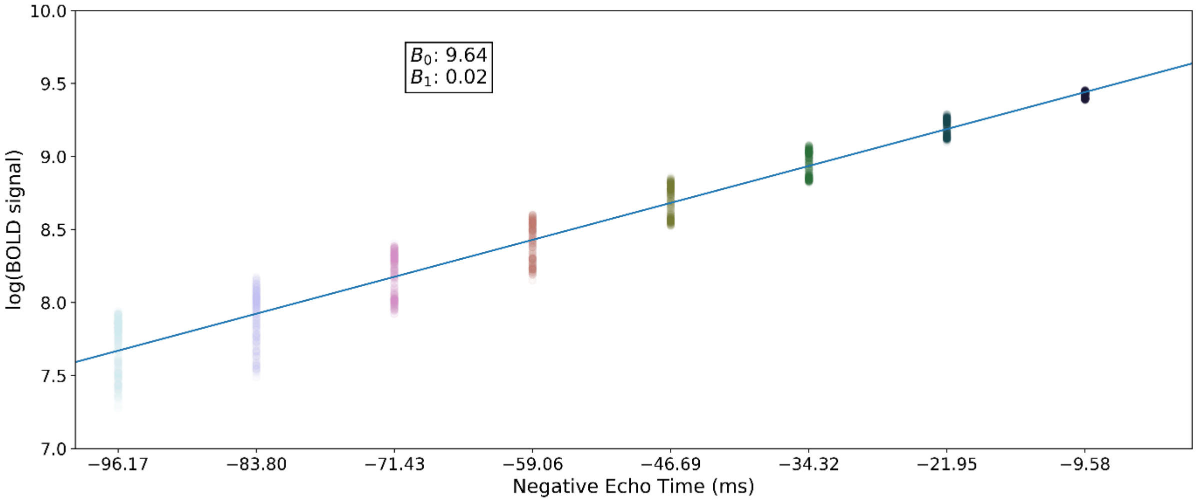

Figure 2.5 - Example of model fit: the BOLD data are subjected to logarithmic log(|S|+1) transform, where S denotes the BOLD signal and echo times are multiplied by -1, and a linear regression is applied to these to obtain a simple line. From the values of intercept B0 and slope B1, it will be possible to derive the values of interest S0 and T2.* [a]

The key values of interest in the decay model, S0 and T2*, can be obtained through simple transformations of the intercept (B0) and slope (B1) of the line, respectively, illustrated in Eq. 2.1 and Eq.2.2 below.

$$S_0 = e^{B_0} \qquad\qquad T_2^* = \frac{1}{B_1}$$

Equations 2.1 and 2.2 - Voxel-specific values of S0, the initial signal intensity within a voxel before decay, and T2, the rate of signal decay over time, respectively.*

The resulting values can be used to show the single-exponential decay model fitted to the original data, as can be seen in Fig.2.6 below.

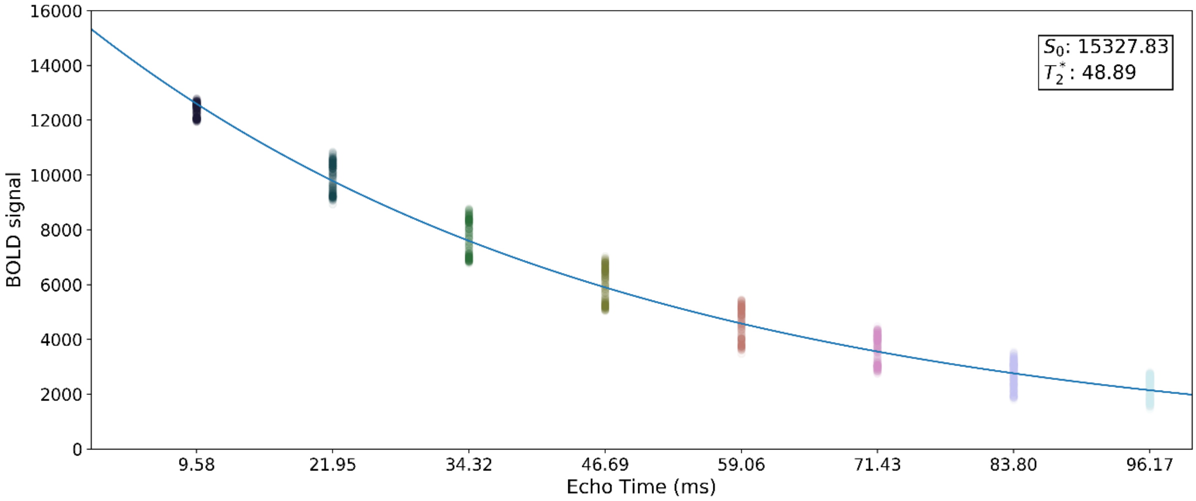

Figure 2.6 - Continuation of the example described in Fig. 2.5: The values of S0 and T2 obtained by applying equations 1 and 2 to the values of B0 and B1 derived from the linear regression can be used to apply a single-exponential decay model to the original data.* [a]

2.2.2.2 Adaptive Mask Generation

Some brain regions, such as the orbitofrontal cortex and temporal poles, experience signal dropout especially at longer echo times. To avoid using the poor-quality signal of the affected echoes when calculating parameters such as T2* and S0 for a given voxel, tedana generates an adaptive mask: in this mask, a value is assigned to each voxel, indicating the number of echoes with reliable signal. When calculating the values of T2* and S0, only the first n echoes are considered, where n corresponds to the value of the adaptive mask for that voxel.

2.2.2.3 Optimal Combination

Using the estimated values of T2*, tedana combines the signal of different echoes through a weighted average. The weights assigned to each echo are determined by the equation 2.3 below.

$$w_{TE} = TE * e^{\frac{-TE}{T_2^*}}$$

Equation 2.3 - weights assigned to each echo to combine them through a weighted average.

The calculated weights are then normalized across all echoes. These normalized weights are used to calculate a weighted average, taking advantage of the higher signal content in the earliest echoes and the higher sensitivity in the later echoes.

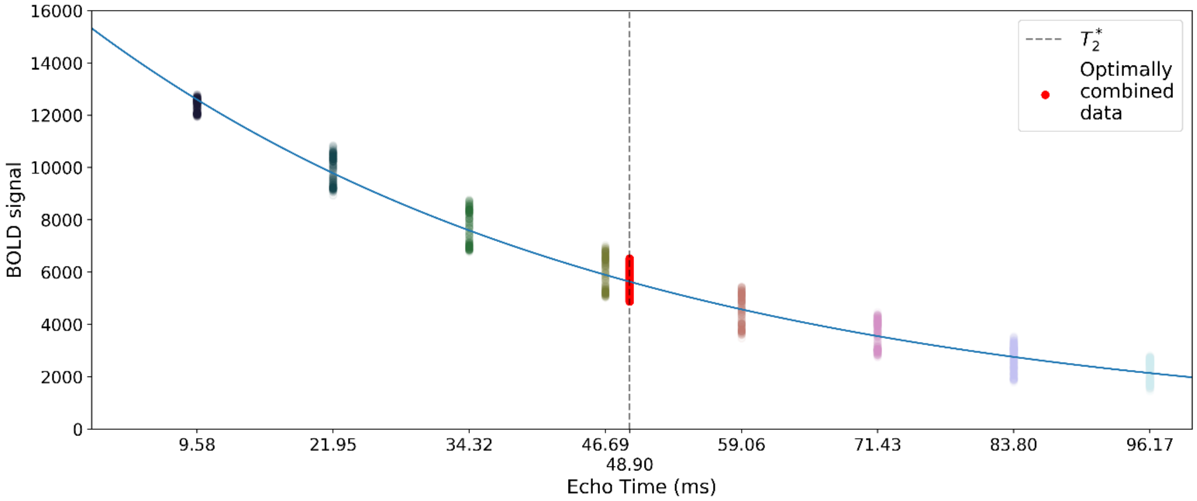

Figure 2.7 - Continuation of the example described in Fig. 2.5: The distribution of values resulting from the optimal combination of data lies between the distributions of individual echoes. [a]

The distribution of values resulting from this optimal combination of data lies between the distributions of the individual echoes (Fig. 2.5 above).

In addition, the time series of the optimally combined data has the characteristics of a mixture of other echoes, as it effectively represents a combination of such echoes.

The results of the optimal combination of echoes with tedana is shown in Fig. 2.8 below for the subject with Parkinson's disease (PD) and the healthy control, respectively.
For each subject, the three separate echoes (TE=10,20,30 ms), as well as the result of slice timing and motion correction in AFNI, are shown initially, followed by the result of their optimal combination in tadana: the first echo time is the brightest, due to the limited signal decay time, while darker areas (so-called "drop out") are observed in the last echo times, due to complete signal decay, because of the inhomogeneity of the magnetic field. The image obtained from the optimal combination of echoes uses the information from all three images, exploiting the signal from the earlier echoes to cope with the drop out phenomenon. [a]

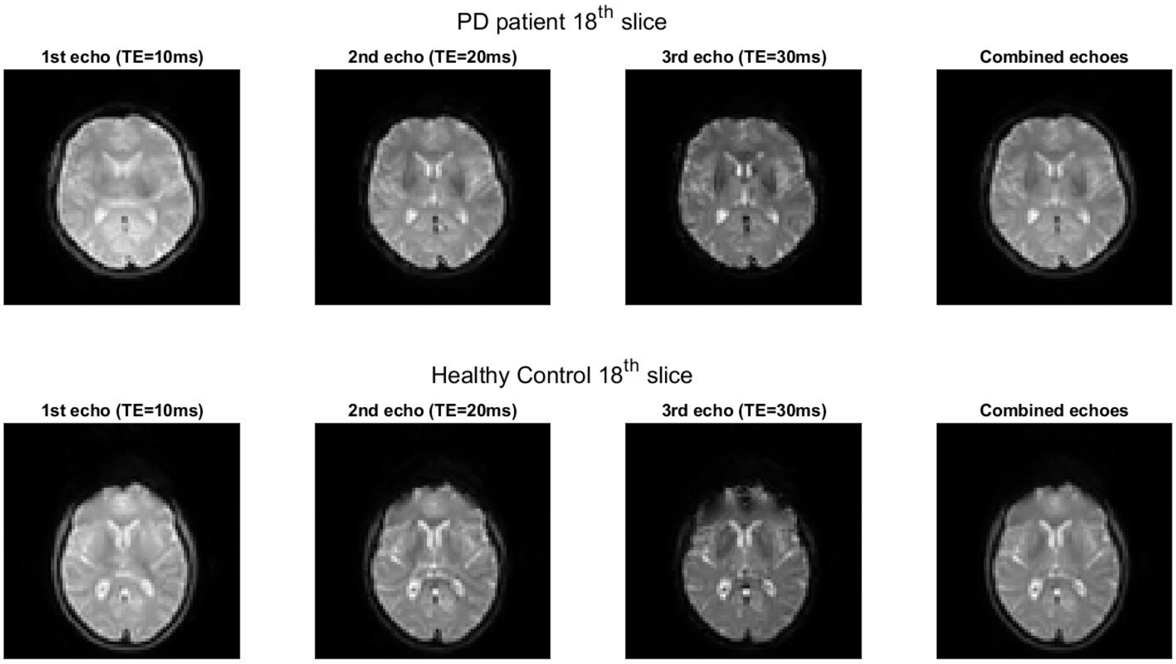

Figure 2.8 - Representation of the signal at echo times TE=10,20 and 30ms in the two subjects considered in the study and result after the optimal combination of the three echoes using tedana, respectively in the patient with Parkinson's disease (on the top) in the healthy control (on the bottom).

Fig. 2.9 on the following page also shows the histograms derived from an analysis of the temporal signal-to-noise ratio (tSNR) maps (see Section 2.4.1 "*Evaluation Metrics: Temporal Signal-to-Noise Ratio (tSNR)*" for more information). The results confirm what has just been said: the tSNR maps follow a decreasing trend as the echo time increases, with the image optimally combined with tedana presenting higher tSNR values demonstrating better overall signal quality, especially in the regions affected by the dropout.

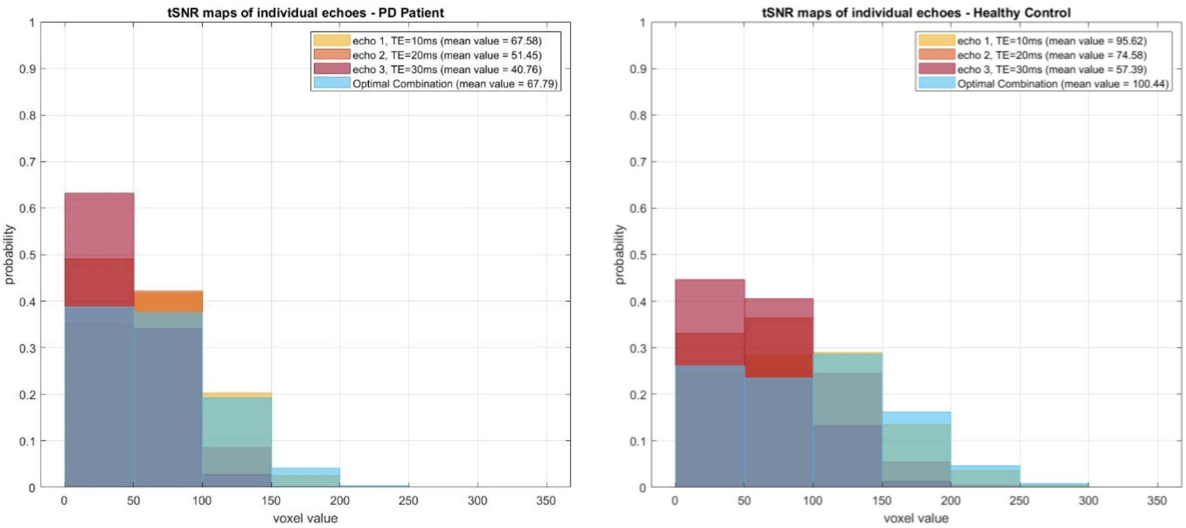

Figure 2.9 - Histograms of the temporal signal-to-noise ratio (tSNR) maps of the single-echo acquisitions (TE=10ms in yellow, TE=20ms in orange and TE=30ms in red) and of the optimal combination of echoes performed with a tedana (in light blue), respectively for a patient with Parkinson's disease (on the left) and healthy control (on the right). For this evaluation, the images were normalised to make their tSNR values comparable.

The image corresponding to the first echo time (TE=10 ms) is more uniformly bright for both subjects, with a higher average tSNR among the single-echo acquisitions, justified by the short echo time that did not allow the signal to undergo significant decay.

In the image corresponding to the second echo time (TE=20 ms), the signal starts to undergo some decay due to the longer echo time. This is reflected in the tSNR map: a decrease in the average tSNR is observed compared to the image with TE=10 ms. However, as the echo time is still relatively short, the image is still uniform without very dark areas.

In contrast, the image corresponding to the third echo time (TE=30 ms) has the lowest average tSNR of the three due to the very long echo time. The signal undergoes significant decay, leading to the presence of darker areas where the signal has been completely lost: the tSNR map reflects this signal loss with lower values than the other two images.

Finally, the optimally combined image with tedana, using information from all three images to improve signal quality, presents a better tSNR map than the individual images, as expected. In fact, higher tSNR values are observed in regions where the images with longer TE lost signal, as the information from the images with shorter TE is used to fill these gaps.

2.2.3 AFNI: B0 Field Distortions Correction

TASK	TOOL	COMMAND	OPTIONS
B0 DISTORTION ESTIMATION	AFNI	*3dQwarp*	-plusminus for "meet-in-the-middle" warping (-base AP sequence, -source PA sequence)
B0 DISTORTION CORRECTION	AFNI	*3dNwarpApply*	-nwarp to apply negative warp

Table 2.3 - commands used to implement B0 distortions correction in AFNI.

Any step that alters the relationship between the signal quantities and the echoes, such as field distortion correction or filtering, must take place after the combination of the echoes to prevent the intensity gradients and subsequent calculation of T2* values at voxel level from being distorted or incorrect. An aggressive temporal filter or spatial smoothing could similarly distort the relationship between echoes at each time point. [a]

In the context of multi-echo MRI data processing, it is crucial to accurately address the correction of B0 field distortions to obtain reliable results, as it can cause inaccuracies in the spatial representation of the data.
For this purpose, once the three echoes with tedana were optimally combined, AFNI's *3dQwarp* command was used to calculate the displacement field to correct distortions in brain images: it is a mathematical representation of the spatial deformations applied to the base image to align it with the source image. In this case, the meet-in-the-middle deformation technique was used with the baseline sequences in the antero-posterior direction (AP sequence) and the source sequence in the postero-anterior direction (PA sequence). The displacement field is generated by comparing the base image with the source image using motion correction and alignment algorithms to calculate the displacement field that represents the geometric transformation required to match the two images.

The *3dQwarp* command generates a positive warp and a negative warp:

- The positive warp (or warp plus) represents the spatial deformation required to align the base image with the source image.
- The negative warp (or warp minus) represents the spatial deformation required to align the source image with the base image.

In summary, *3dQwarp* generates plus and minus warps, i.e., positive and negative warps, by calculating the displacement field that aligns the base image with the source image and vice versa. These displacement fields are then applied to the respective images to achieve the desired alignment.

Once the deformations of the B0 field have been estimated, their correction is performed using AFNI's *3dNwarpApply* command, developed specifically for this task.
Since the analyzed images were acquired in the antero-posterior (AP) direction, negative (minus) warp transformations were applied to correct distortions. Using a minus warp, the calculated displacement field between the source image (PA in this case) and the base image (AP in this case) is applied to the source image itself, producing an image aligned with the base image. Then, MINUS deformation is used to align the source image with the base image. [f]
The application of negative warp for distortion correction was also confirmed by comparing tSNR maps computed on the same image, corrected using positive warp, negative warp, and the combination of the two, respectively.

The results of B0 field distortion correction using negative strain in AFNI are shown in Fig. 2.10 and Fig. 2.11 on the following page for the subject with Parkinson's disease (PD) and healthy control, respectively.
For more details on choosing the type of warp to be used, see Section 2.4.2 "*B0 field distortion correction: Warp selection*".

The same pre-processing steps performed with AFNI were also performed with the FSL (the FMRIB Software Library) software. More details on the comparison between the two tools can be found in section 2.4.3 "*Comparison of preprocessing pipelines: AFNI vs FSL*".

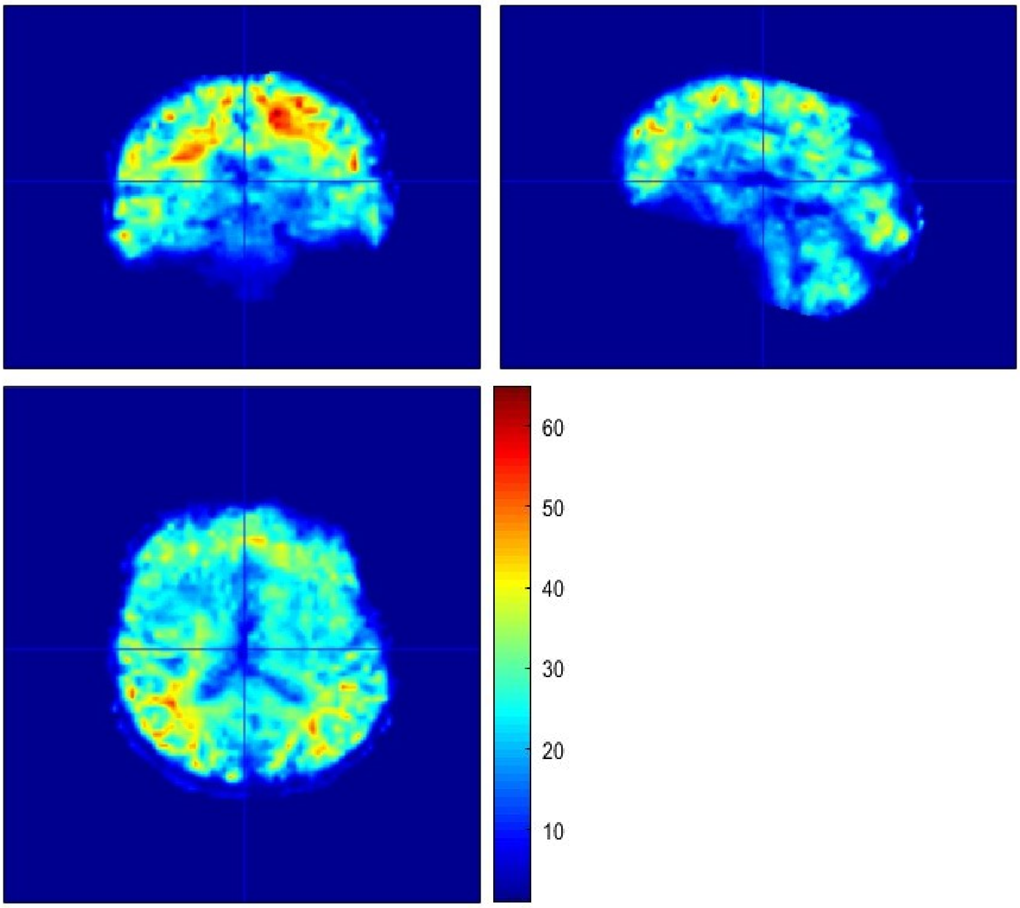

Figure 2.10 - Temporal signal-to-noise ratio (tSNR) maps of the fMRI signal in Parkinson's Disease (PD) patient after correction of B0 field distortions.

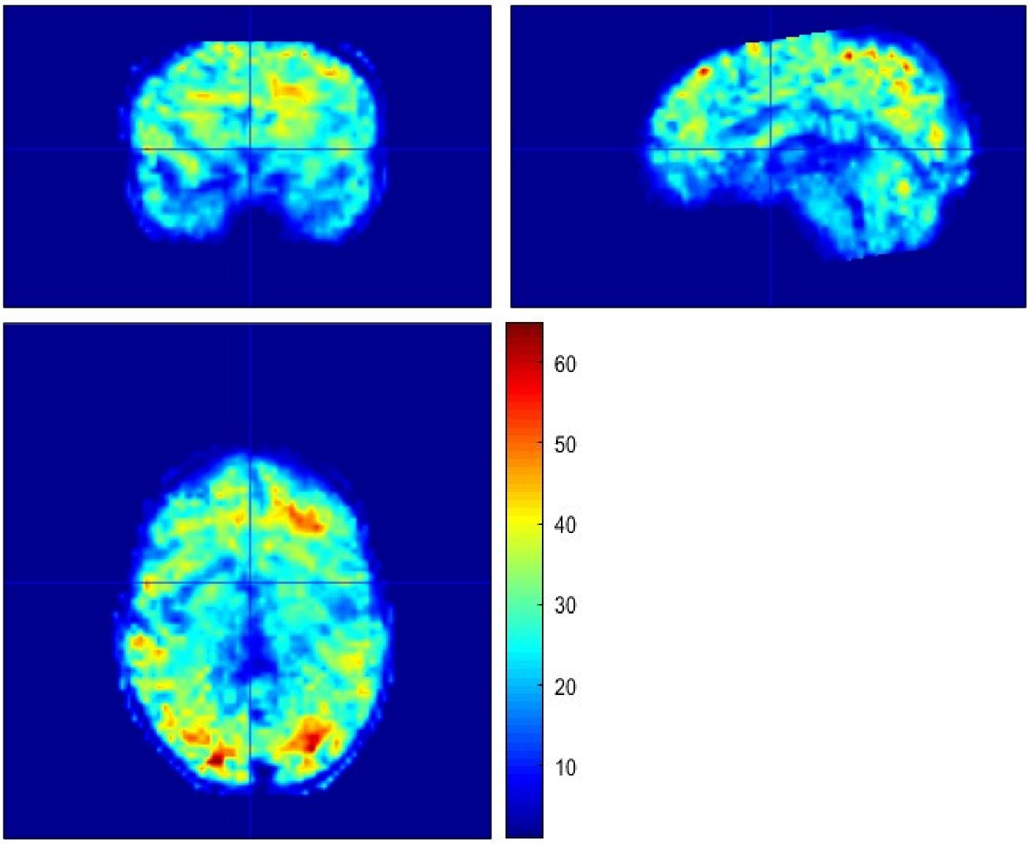

Figure 2.11 - Temporal signal-to-noise ratio (tSNR) maps of the fMRI signal in the healthy control after correction of B0 field distortions.

2.2.4 Regression for White Matter and Cerebrospinal Fluid

As part of fMRI signal analysis, regression of white matter (WM) and cerebrospinal fluid (CSF) is a crucial process to remove the effect of these physiological components from the neural signal of interest. Before applying regression, tissue segmentation was performed on T1w images using FAST (FMRIB's Automated Segmentation Tool) in FSL, generating probabilistic maps for the GM, WM, and CSF compartments. From these probabilistic maps, binary masks were then derived, which, when applied to the fMRI signal, allowed identification of the white matter and CSF regions.[24]

Through Principal Component Analysis (PCA), regressors were obtained separately for WM and CSF voxels to remove these physiological influences from the fMRI signal. This approach was standardized using a fixed number of principal components, ensuring uniformity of analysis across subjects. The residuals obtained were subsequently used to analyse the neural activities of interest using the general linear model (GLM).

2.2.4.1 SPM12: Realignment and Coregistration

Before proceeding with the implementation of the regression for white matter (WM) and cerebrospinal fluid (CSF), SPM12 software was used to perform some preliminary operations: initially, to realign the volumes of the fMRI signal to create an averaged image, which was subsequently used for coregistration of the fMRI image in structural space to enable the application of the WM and CSF masks to the signal. In the context of functional MRI data analysis, the realignment and coregistration steps are crucial to ensure accurate alignment of the acquired images and correction of motion-related artifacts.

In the realignment process, temporal images obtained from the same subject are aligned through a 6-parameter spatial transformation (rigid body) obtained by a least-squares approach. The first image of the acquisition sequence is chosen as the reference, and subsequent images are aligned to it by obtaining estimates of the translation and rotation parameters for each image. After the realignment process, the images are reprocessed (resliced) to match the voxel positions of the reference image and a volume-averaged image is generated.. [25]

In the process of coregistration, the goal is to align different imaging modalities, such as in this case aligning fMRI data with structural images such as FLAIR (fluid-attenuated inversion recovery) scans. Using a rigid-body transformation model, which includes three translation and three rotation parameters, an attempt is made to maximize the similarity between the images to be aligned. The choice of objective function depends on the mode of the images involved (same mode or different modes). Through the coregistration process, the transformation parameters that optimally align the image to be moved (in this case, the fMRI image) with the reference image (in this case, the structural image) are estimated. Then, the images are reprocessed (resliced) to match the voxel positions of the reference image.

In both processes, parameters such as the type of interpolation used, wrap-around handling in the image directions, and masking can be adjusted to handle regions where data sampling has been compromised by subject motion.[25]

The results of the coregistration of the fMRI image on the FLAIR-T2w structural image with SPM12 and the masks to extract the white matter and CSF signals from the resulting image are shown in Fig. 2.12 and Fig. 2.13 on the following pages, for the subject with Parkinson's disease (PD) and the healthy control, respectively.

A) **Normalized Mutual Information Coregistration – PD Patient**

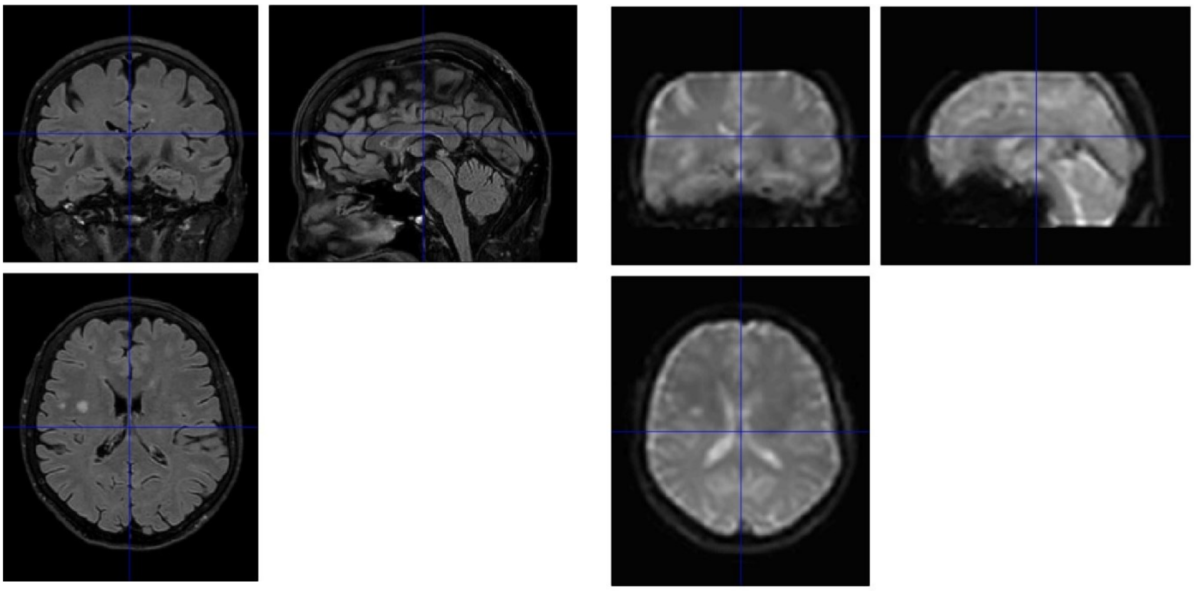

B) **PD Patient's WM mask**

C) **PD Patient's CSF mask**

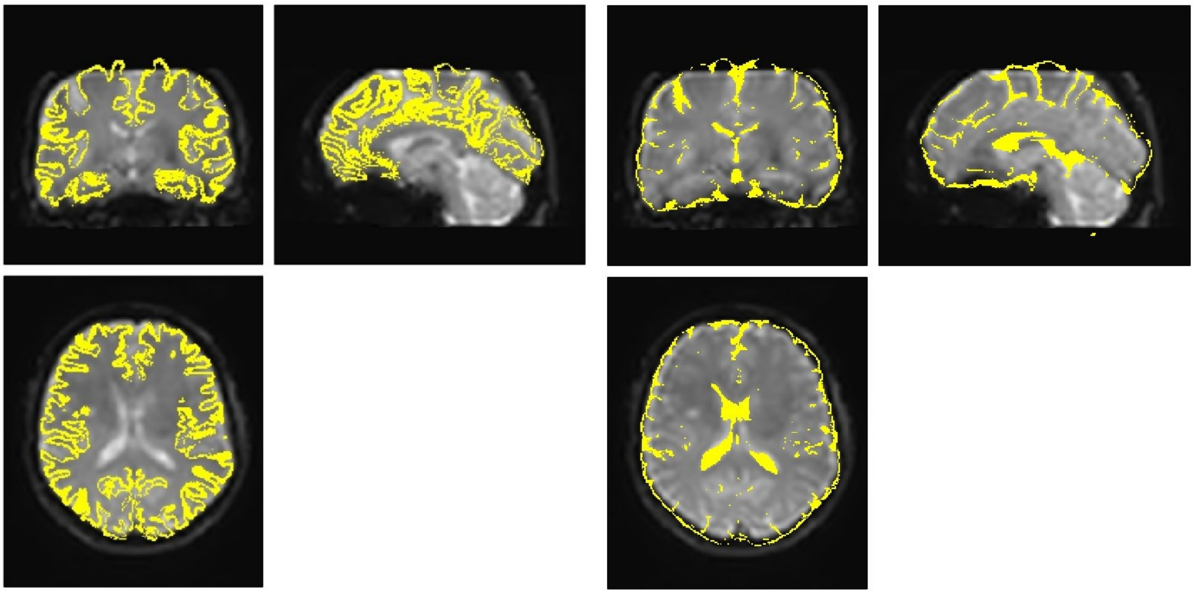

Figure 2.12 - Result of the coregistration of the fMRI image on the FLAIR-T2w structural image with SPM12 (A) and corresponding masks used to extract the white matter (B) and CSF (C) signal in the subject with Parkinson's disease (PD).

A) **Normalized Mutual Information Coregistration – Healthy Control**

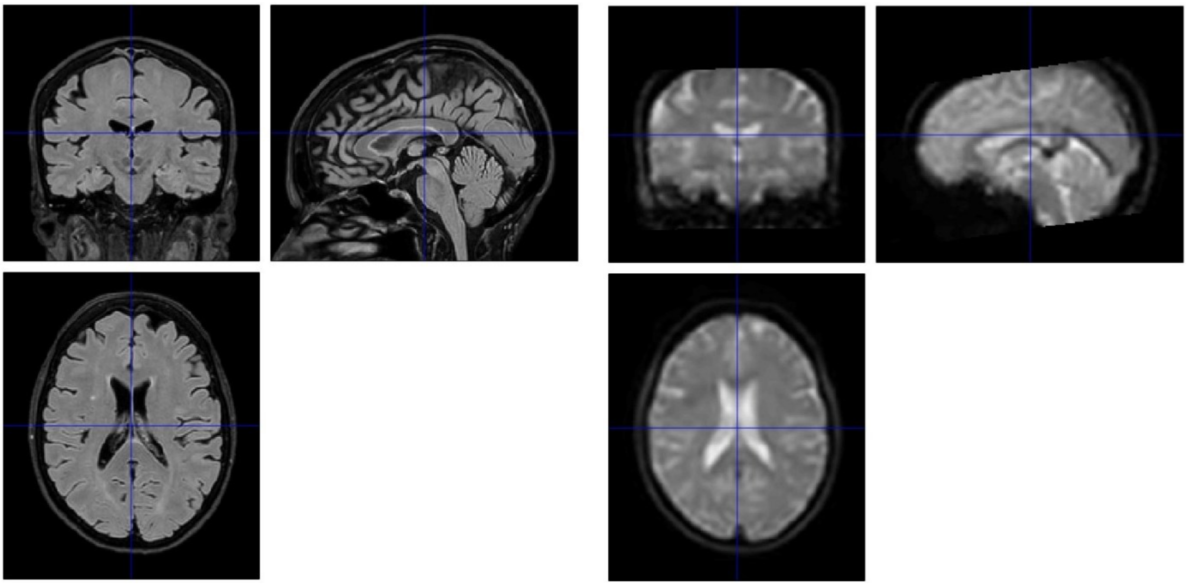

B) **Healthy Control's WM mask**

C) **Healthy Control's CSF mask**

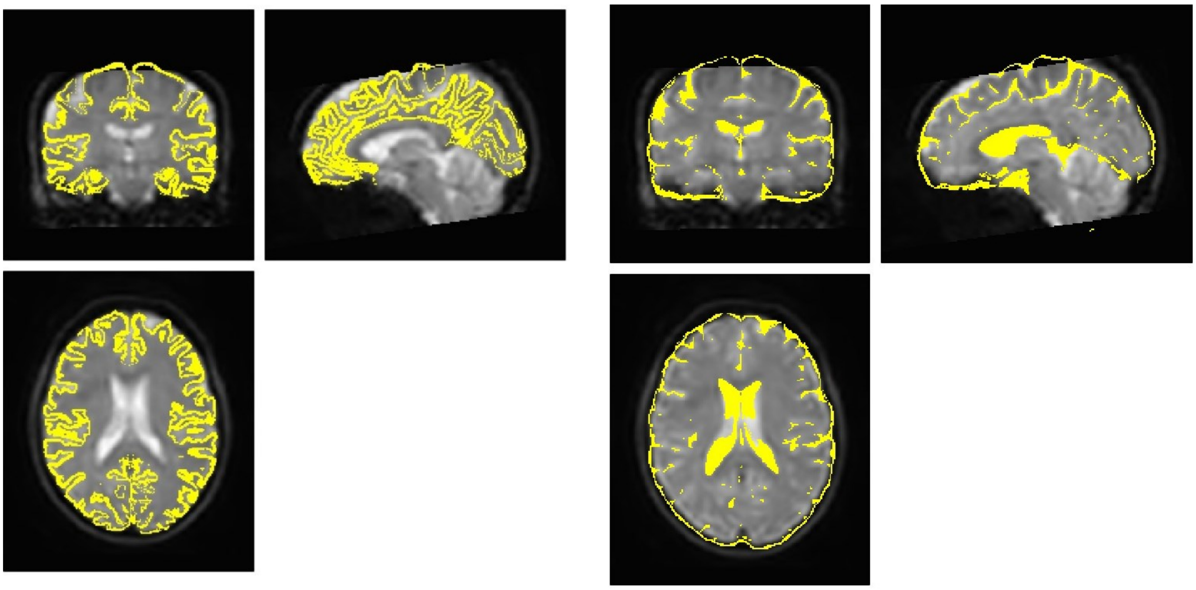

Figure 2.13 - Result of the coregistration of the fMRI image on the FLAIR-T2w structural image with SPM12 (A) and corresponding masks used to extract the white matter (B) and CSF (C) signal in the healthy control (HC).

2.2.4.2 MatLab: Principal Component Analysis (PCA)

In the context of functional connectivity (FC) analysis using task-free functional magnetic resonance imaging (fMRI) data,[28] i.e., under resting conditions, the handling of noise is critical, as its complex spatiotemporal structure can introduce bias into connectivity estimates.[27]

Noise signals, which are uncorrelated signals with the phenomenon of interest and therefore must be regressed from the data, can be computed using mathematical models or data-driven methods. The data-driven approach involves the direct extraction of noise signals from fMRI data by separating useful signals from noise through multivariate decomposition methods, such as Principal Component Analysis (PCA).[27]
The latter is a technique developed to identify the main modes of variation in high-dimensional data and plays a key role in this context: by projecting the raw fMRI data into orthogonal spaces called principal components (PCs), which represent the largest variance in the original dataset,[28] it allows the identification of the eigenvalues (amount of variation) and eigenvectors (direction of variation) of the data's covariance matrix.[26]

In this work, signals from cerebrospinal fluid (CSF) and white matter (WM) are considered as noise signals because they are believed to contain mainly physiological and hardware noise, devoid of neural signals. Using these signals as noise estimates and regressing them from the data improves the signal-to-noise ratio in gray matter (GM), the region of interest. A commonly used approach to calculate noise signals related to the CSF and WM is based on extracting the fMRI time series from the CSF and WM masks, respectively, and calculating the representative signals by PCA,[24][27] followed by regressing these component time series from the data.
The use of PCA on the fMRI signal to which the white matter and CSF masks were applied led to the identification of principal components for each subject: the practical challenge, however, is to choose the number of these principal components of the CSF and WM compartments to be selected for regression from the data.

Several criteria emerge from the literature, such as identifying "significant" components not due to random noise or ensuring that the selected components explain a significant part of the variance of the time series. These estimates are subject-specific but are often treated as fixed values in fMRI-based neuroimaging software and studies. A frequent choice is to extract five regressors from CSF and WM signals, respectively, as shown in the CONN toolbox (https://www.nitrc.org/projects/conn), where they are used as defaults, but also in many other studies using different software (e.g., Baniqued et al., 2018). [27]

In accordance with these results, five principal components were identified for each CSF and WM signal and for each subject (Fig. 2.14), keeping the choice of the number of principal components to be considered consistent across subjects: this uniformity in the choice of the number of regressors was maintained to avoid a variation in model complexity across participants.

The overall extraction of ten principal components per subject, obtained from both the fMRI signal with the white matter mask applied and the fMRI signal with the CSF mask applied, provided the set of regressors needed to implement the General Linear Model (GLM). This GLM-based approach facilitated the calculation of the residuals, which represent the fMRI signals devoid of the influences of white matter and CSF.

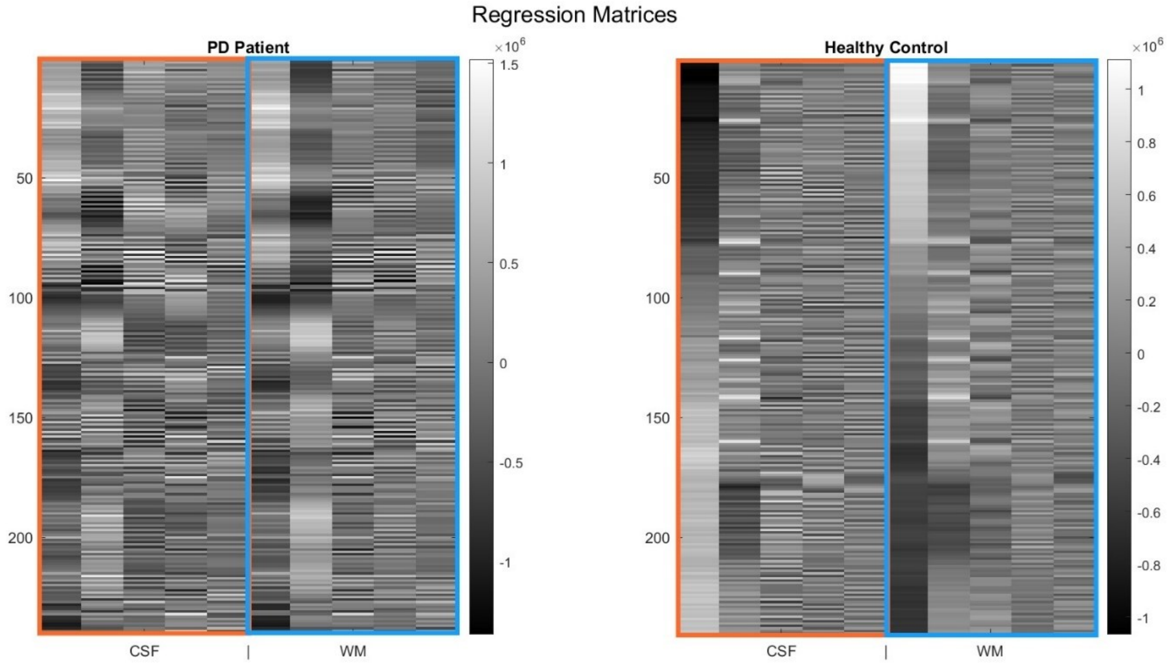

Figure 2.14 - Regression matrices used in the general linear model (GLM) to regress the white matter (WM) and cerebrospinal fluid (CSF) signal. Each subject's matrix consists of 10 regressors: 5 principal components obtained from PCA on the masked fMRI signal for CSF (in orange) and 5 principal components obtained from PCA on the masked fMRI signal for WM (in blue).

2.2.4.3 MatLab: General Linear Model (GLM) Analysis [24]

The General Linear Model (GLM) analysis is a widely used technique in the field of functional magnetic resonance imaging (fMRI) to study the relationship between experimental observations and predicted responses. In this method, fMRI time series data, denoted as y, are modeled as a linear combination of various factors, including predicted task responses, and a white Gaussian distributed additive noise term ε. The model can be expressed through the Eq. 2.4 below:

$$y = \beta_0 + \beta_1 x_1 + \beta_2 x_2 + \ldots + \beta_n x_n + \varepsilon$$

Equation 2.4 - General Linear Model (GLM) equation. y represents the dependent variable (fMRI time series data) modeled as a linear combination of xi factors. βi is the parameter weight associated with the contribution of each factor to the dependent variable y. ε represents a distributed Gaussian white additive noise term.

Here, x_i represents each model factor, and β_i is the parameter weight associated with the contribution of each factor to the dependent variable y. This model represents a linear mixture of factors that can be used to capture the relationship between the experimental conditions and brain activity.

The GLM analysis involves statistical testing to evaluate how well the time series of each voxel in the brain is explained by this linear combination of model factors. The fitted results are converted into t- or F-statistics, allowing the assessment of the significance of each model factor's contribution to y. This testing assumes a null hypothesis where the parameter weights β_i for the model factors are zero, indicating no contribution from those factors.
The GLM approach offers flexibility in shaping the predicted responses by modifying the model factors, accommodating inconsistent temporal delays and variability of hemodynamic response function (HRF) shapes across different brain regions.

This process is analogous to correlational analysis, but compared to traditional correlation analysis, the GLM approach is more versatile and can accommodate complex experimental designs involving multiple cognitive conditions. It can also incorporate various sources of variability as model factors, such as motion parameters, physiological fluctuations, subject-related information, and environmental factors. The GLM technique finds applications beyond basic correlation analysis, including characterizing impulse responses in event-related designs, studying psychophysiological interactions among brain regions, and exploring relationships between fMRI and other imaging modalities.

However, the GLM has its limitations. Its validity relies on assumptions about relationships between model factors, noise, and the structure of the noise term. Unfortunately, these assumptions are often not thoroughly discussed in practice. Additionally, the GLM assumes linearity of blood oxygen level-dependent (BOLD) responses, which might not hold true in all cases. In such situations, more complex higher-order models need to be considered.

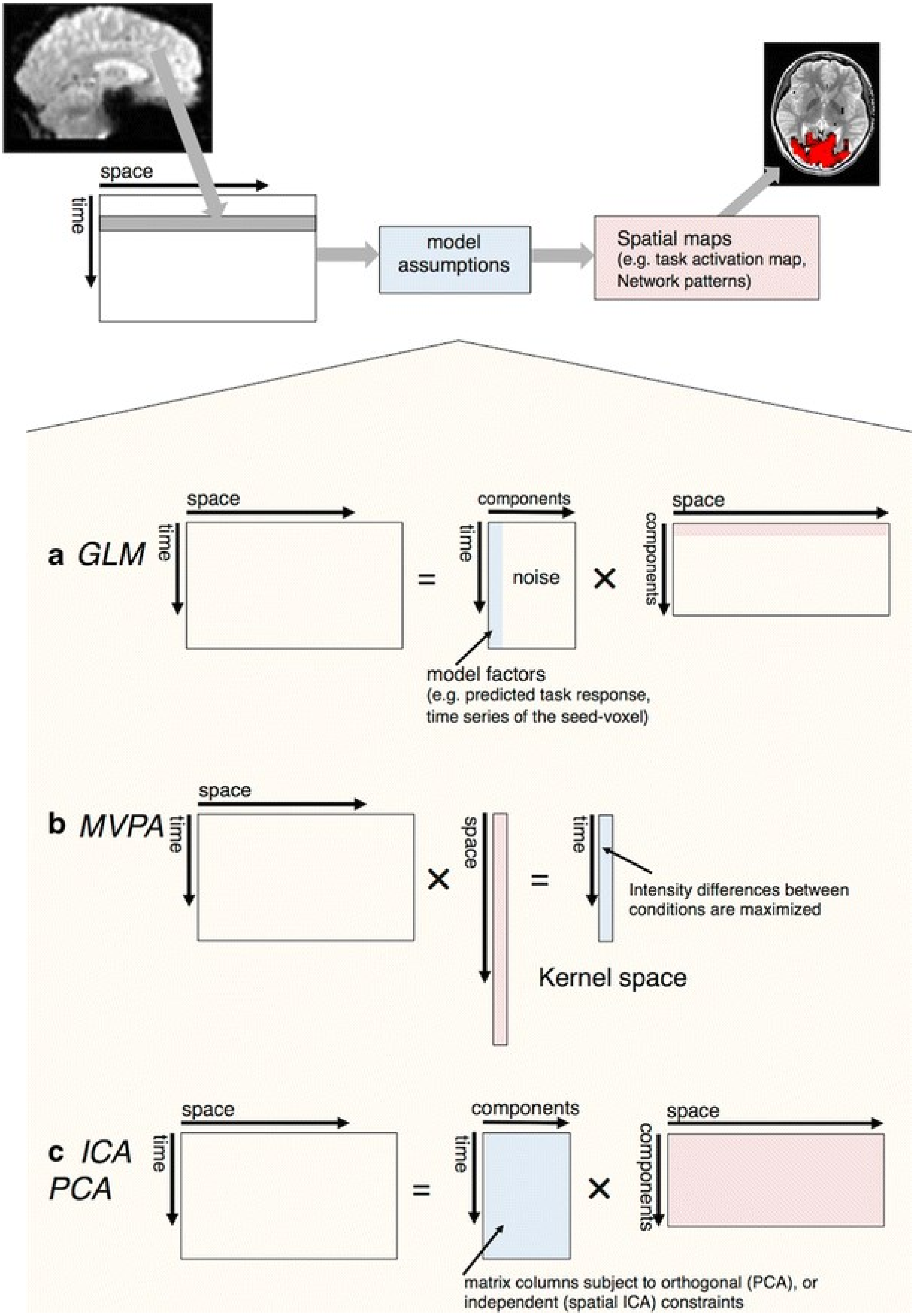

Figure 2.15 - Most model-based and model-free analyses in fMRI studies can be incorporated into a consistent matrix decomposition scheme. Specifically, the 4-D fMRI dataset can be reorganized into a 2-D matrix by aligning all voxels from the same time point in a row; several approaches (e.g., GLM (a), MVPA (b), ICA/PCA (c)) attempt to decompose the 2-D matrix into subcomponents by imposing various assumptions on the structure of the decomposed matrix (blue rectangles), then extract spatial patterns (network patterns, pink rectangles) of neuron-related contributions.[27]

In this context, the General Linear Model (GLM) was employed with the purpose of regressing, for each subject, the rs-fMRI signal for white matter (WM) and cerebrospinal fluid (CSF). The five principal components obtained from PCA, known as "scores," derived from WM and CSF signals, were used as predictors. This resulted in a total set of ten predictors, or regressors.

The design matrix X (Fig. 2.14 on previous pages), also known as the predictor matrix, was assembled by combining the motion correction parameters (see section 2.2.1: "*AFNI: Slice Timing and Motion Correction*") with the WM and CSF space scores derived from the principal component analysis. This generated a matrix of size 240 x 16, where 240 represents the number of time series and 16 indicates the number of predictors.
When processing the fMRI data, represented by the variable y, the β parameter was estimated using the Weighted Least Squares (WLS) method, as shown in Eq. 2.5 below. The weights for each volume were assigned considering the corresponding Framewise Displacement (FD) value, with one volume being considered an outlier in the case of FD>0.4.

$$\beta \ = \ (X^T \ diag(w) \ X)^{-1} \ X^T \ diag(w) \ Y$$
$$where \ \ X \ = [MoCoparams \ \ score_1^{CSF} \quad ... \quad score_5^{CSF} \ score_1^{WM} \quad ... \quad score_5^{WM}]$$

Equation 2.5 - Estimation of parameter β using the WLS method. X represents the design matrix, or predictive matrix, obtained by concatenating the 6 motion correction parameters (3 for translation and 3 for rotation) subjected to appropriate demeaning, the 5 principal components of the CSF and the 5 principal components of the WM resulting from the PCA. W represents the weights associated with each volume, estimated from the Framewise Displacement (FD) value of each volume. Y represents the raw fMRI signal to be regressed for the CSF and WM signals.

The fMRI signal reflecting the effect of WM and CSF was obtained by a regression process. These are the residuals resulting from the application of the WM, defined by the difference between the original fMRI signal and the response predicted by the model for each data point, considering the associated weights. In other words, the wres quantity was calculated as in Eq. 2.6 below, where w represents the weights assigned to each volume, Y represents the initial fMRI signal and $\hat{Y}$ denotes the response predicted by the model. The resulting signal is thus the fMRI signal cleaned of WM and CSF artifacts.

$$wres \ = \ w\left(Y \ - \ \hat{Y}\right) \qquad \text{where } \ \hat{Y} \ = \ X \quad \beta$$

Equation 2.6 - Calculation of the weighted residuals of the general linear model (GLM), wres, as the difference, weighted by w, between the original (raw) fMRI data and the predicted model response. Y represents the initial fMRI signal and $\hat{Y}$ indicates the predicted response from the model, calculated as the product of the design matrix, X, and the estimated parameter β.

The results of the rs-fMRI signal regression for cerebrospinal fluid (CSF) and white matter (WM) using the General Linear Model are presented in Figures 2.17 and 2.18 on the following page. These figures show the results for the subject with Parkinson's disease (PD) and the healthy control, respectively.

Fig 2.16 below shows the temporal signal-to-noise ratio (tSNR) maps obtained with the corresponding histogram, which provide further details on the signal evaluation (see section 2.4.1 "*Evaluation metrics: Temporal signal-to-noise ratio (tSNR)*" for more information). It is observed that when regressing the signal for white matter and cerebrospinal fluid, the mean tSNR values increase exponentially, indicating a clear signal improvement with this step.

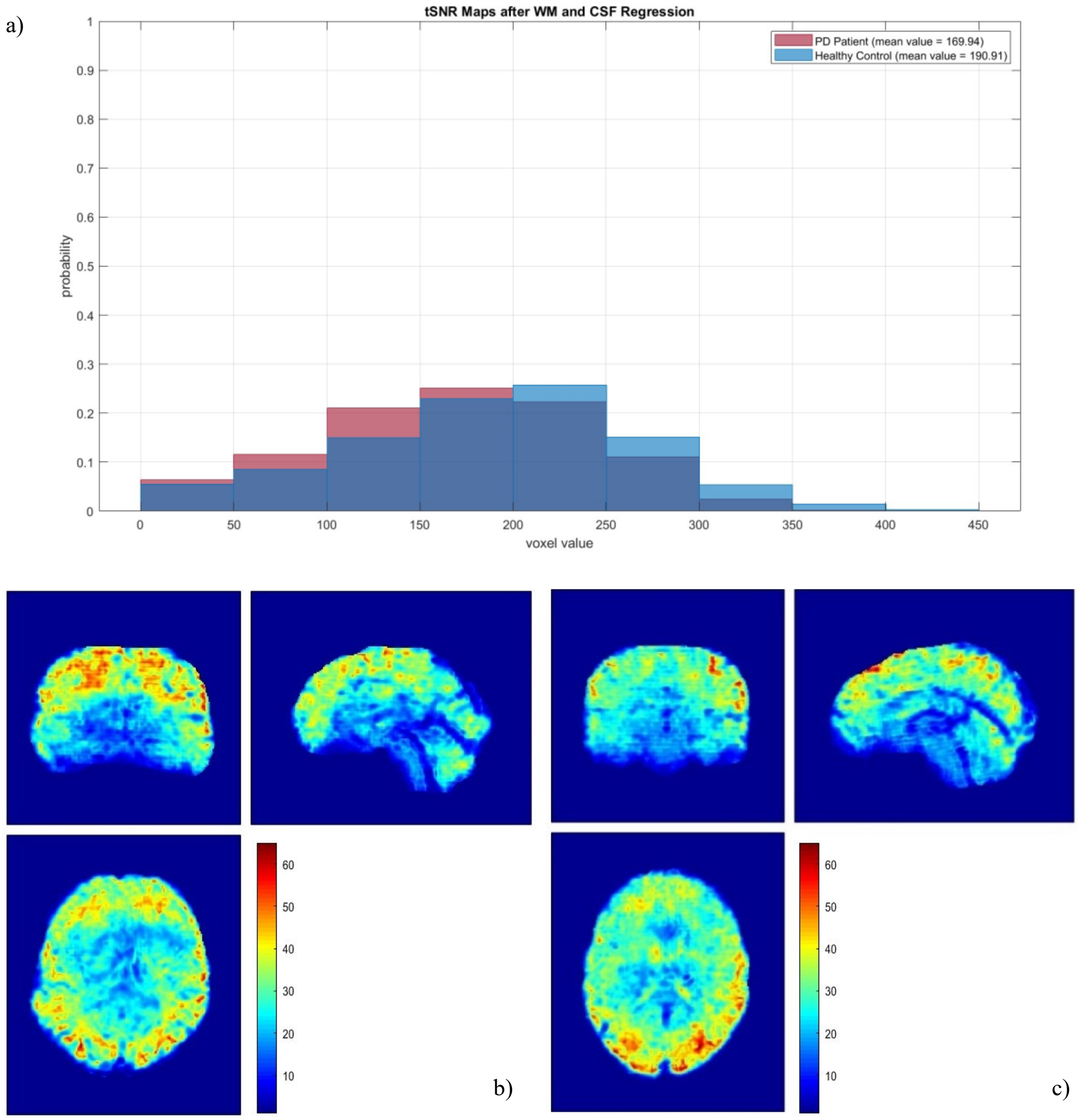

Figure 2.16 - Histogram of the temporal signal-to-noise ratio (tSNR) maps obtained by regressing the signal for white matter and cerebrospinal fluid (a). Below, images of the tSNR maps are presented for the subject with Parkinson's disease (b) and the healthy control (c), respectively.

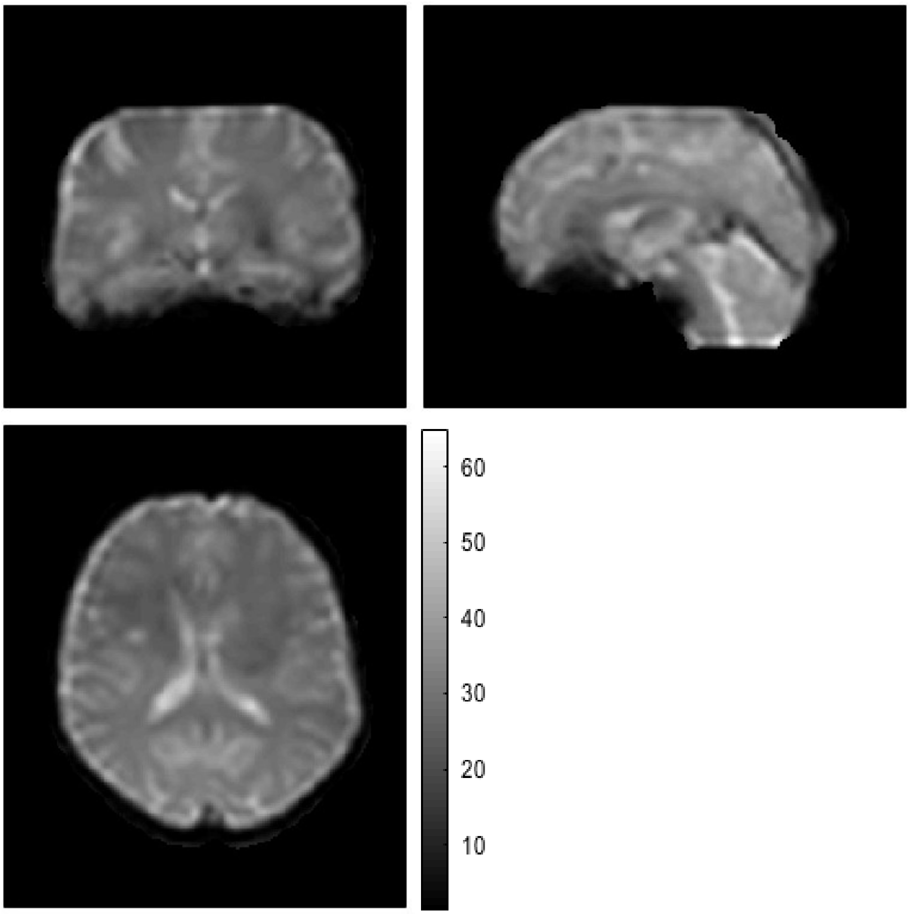

Figure 2.17 - Regression result for WM and CSF on rs-fMRI signal on subject with Parkinson's disease.

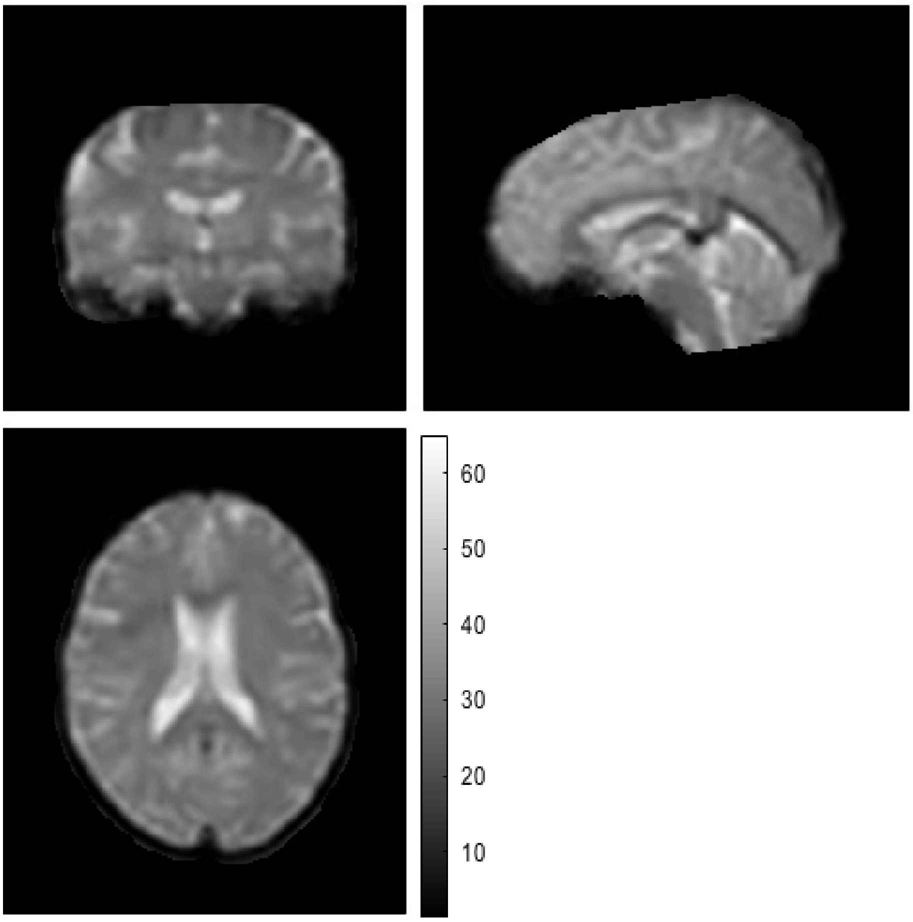

Figure 2.18 - Regression result for WM and CSF on rs-fMRI signal on healthy subject.

2.2.5 Signal Filtering

Analysis of fMRI data involves dealing with different sources of signal variation and noise to extract meaningful neural information. One challenge is the presence of slow drift of the baseline signal over time, along with rapid fluctuations due to noise.[a][b]

Resting-state fMRI studies have highlighted the importance of low-frequency fluctuations (LFFs) in the range of 0.01-0.08 Hz. These fluctuations are believed to have physiological significance and reflect spontaneous neuronal activity, as demonstrated by Biswal et al. in 1995 and Lu et al. in 2007. Specifically, low-frequency oscillations (0.01-0.073 Hz) have been shown to be predominantly attributable to gray matter (GM), while higher-frequency oscillations (0.073-0.25 Hz) are more confined to white matter (WM). In addition, Cordes et al. observed that respiratory and aliased cardiac signals fall within the relatively high frequency band.
For this reason, the data are generally subjected to a band-pass filter, e.g., 0.01-0.08 Hz, to attenuate the influence of low-frequency and high-frequency physiological noise.[21]

Considering these findings from the literature, practical implementations were applied to filter resting-state functional magnetic resonance imaging (rs-fMRI) data: in particular, filtering techniques were employed to deal with both low-frequency and high-frequency noise, including low-frequency drift handling in the latter case, ensuring the extraction of reliable information on neural activity.

2.2.5.1 High-Pass Filter

Before applying a high-pass filter to the rs-MRI data, a crucial step was performed to improve the quality of the data analysis: the *fslmaths* command was used with the *-Tmean* option to average the original signal between voxels over time. This average represents the low-frequency component of the signal, often referred to as the "baseline" or "trend."
Next, after averaging the signal, the original signal was subjected to a high-pass filter using the same *fslmaths* command, this time with the *-bptf* option. The high-pass filter was designed to remove the low-frequency components, emphasizing the high-frequency variations within the signal.

The implementation of the high-pass filter in FSL involved the definition of the parameter σ, which is required as an input by the function *fslmaths* for applying a temporal filter to the data:

its value is determined by applying Eq. 2.7 on the following page, considering a specific value of the repetition time interval (TR) of 2 seconds and a cutoff frequency (f_{cutoff}) of 0.008 Hz.

$$\sigma = \frac{1}{2 \cdot TR \cdot f_{cutoff}}$$

Equation 2 7 - Calculation of the σ parameter that determines the degree of filter attenuation, considering TR=2s and f_{cutoff}=0.008Hz.

The σ parameter modulates the attenuation effect of the filter, influencing the amplitude of the filter response. A higher σ value results in a wider frequency response, which intensifies high-pass filtering and promotes noise reduction.

It is important to note that the low-frequency component of the signal before filter application may contain relevant information. Therefore, to preserve this information, a sum is made between the high-pass filtered signal and the previously calculated average, again using the *fslmaths* command, this time specifying the *-add* option. In this way, the effect of the trend or low-frequency component can be removed from the filtered signal, better isolating the high-frequency variations.
This process ensured that the corrected low-frequency signal maintained its calibrated level, effectively counteracting signal drift.

2.2.5.2 Low-Pass Filter

A sixth-order Chebyshev low-pass filter was implemented in Matlab. This filter was evaluated with cut-off frequencies of 0.08 Hz and 0.2 Hz.

The choice of filter type and order was determined on the basis of previous research conducted by the research team: through a comparison of Butterworth and Chebyshev filters and the use of the *buttord* and *cheb2ord* functions to estimate the optimal order of the filter, it was found that, for the data in question and considering the cutoff frequencies of interest, a sixth-order Chebyshev filter was the most suitable choice.

Then, evaluating the temporal signal-to-noise ratio (tSNR, see Section 2.4.1 "*Evaluation Metrics: Temporal Signal-to-Noise Ratio (tSNR)*" for more information) maps of the resultant images, the one at 0.08 Hz was chosen as the optimal cutoff frequency: in fact, as can be seen in Fig. 2.19, it implies a better average tSNR, demonstrating a prevalence of signal over noise.

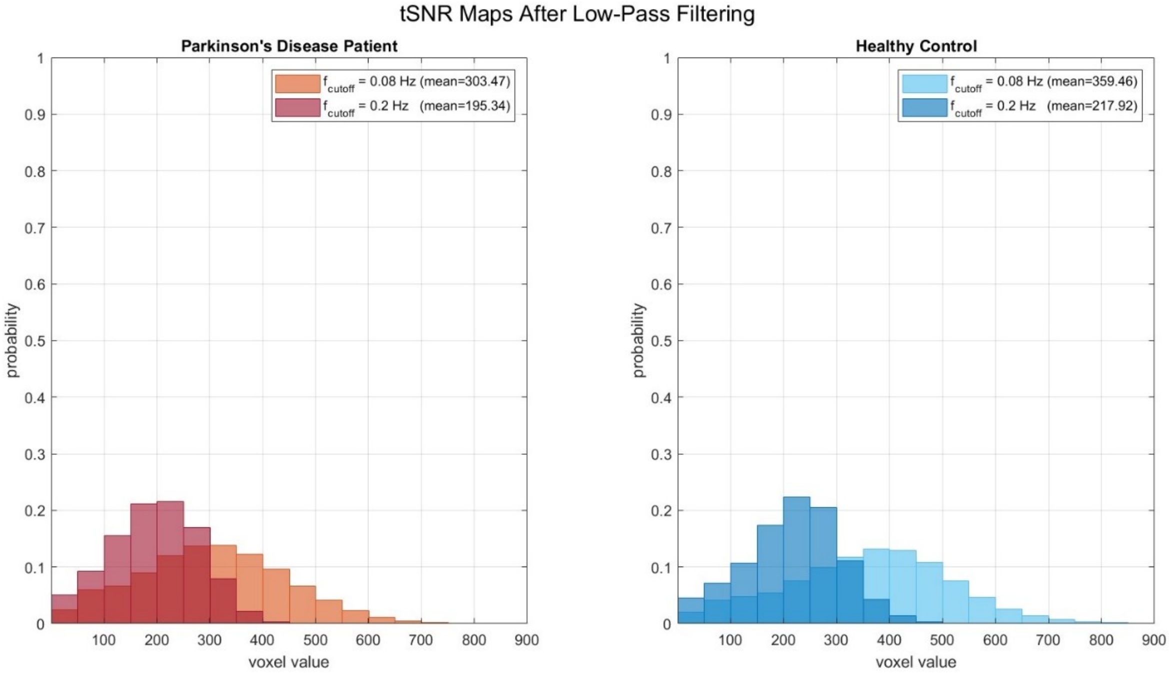

Figure 2.19 - Histogram of the distributions of temporal signal-to-noise ratio (tSNR) values along voxels after low-pass filtering, in the case of cutoff frequency of 0.08 Hz (first distribution) and 0.2 Hz (second distribution) in patient with Parkinson's disease (left) and healthy control (right).

The results after high-pass filtering with cutoff frequency of 0.008 Hz and low-pass filtering with Chebyshev filter of order 6 with cutoff frequency of 0.08 Hz are shown in Figs. 2.20 and 2.21 on the next page, for the subject with Parkinson's disease (PD) and healthy control, respectively, later including a view of the obtained fully pre-processed tSNR maps in Figs. 2.22 and 2.23.

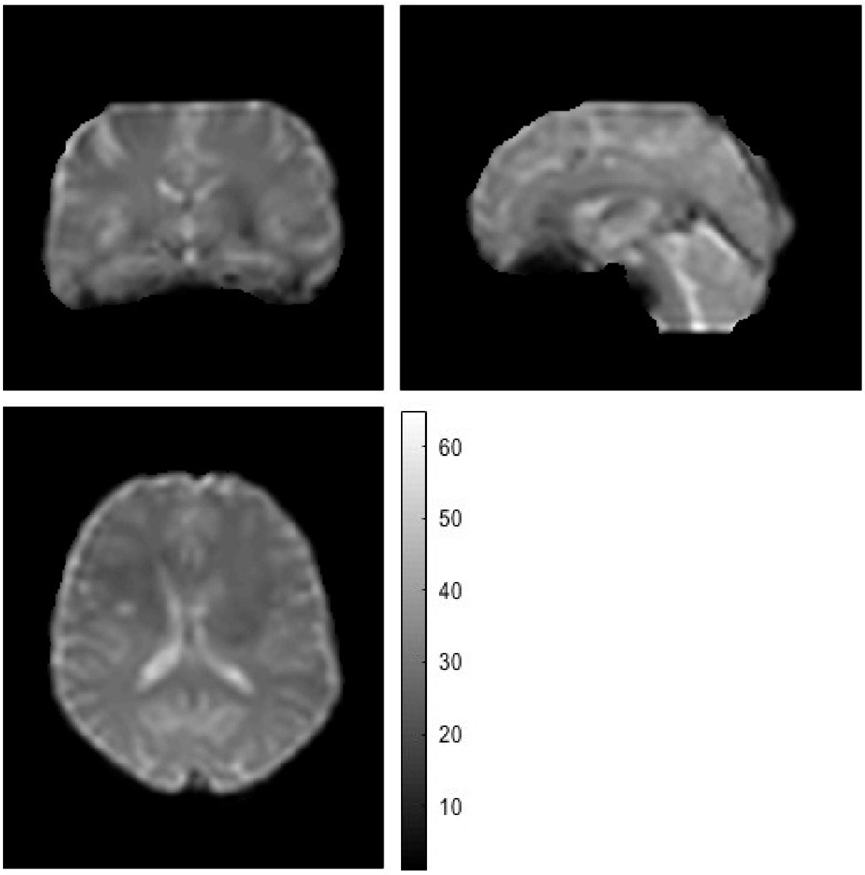

Figure 2.20 - Result of high-pass filtering (with cut-off frequency of 0.008 Hz) and low-pass filtering (with Chebychev filter of order 6 and cut-off frequency of 0.08 Hz) of the rs-fMRI signal of subject with Parkinson's disease (PD).

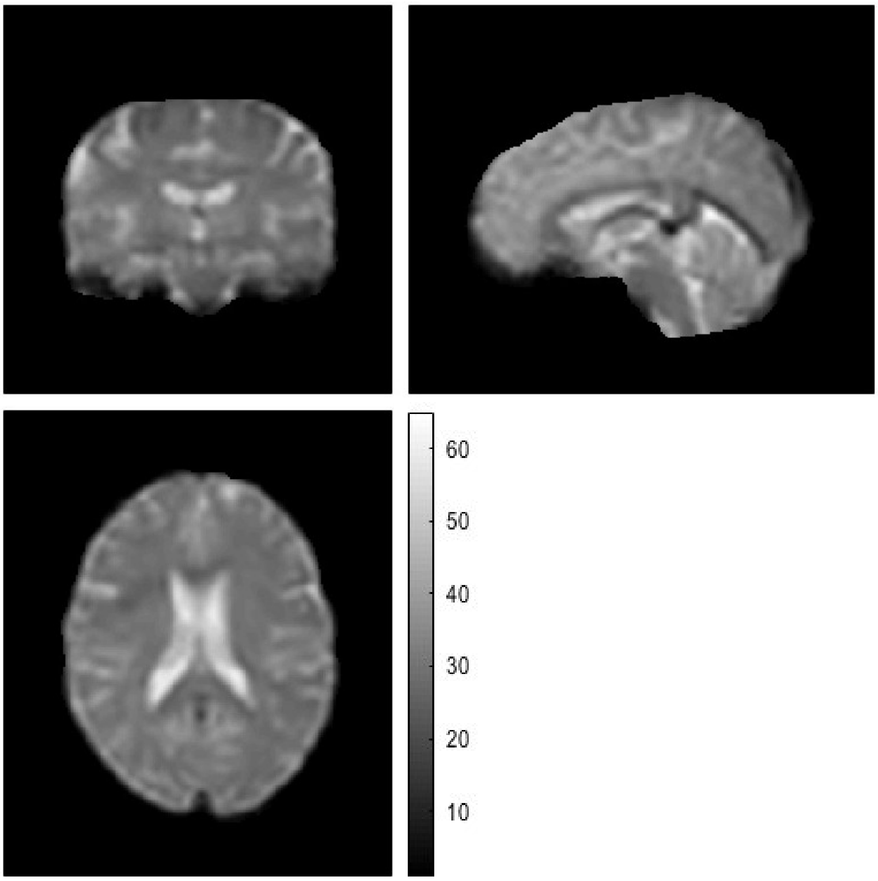

Figure 2.21 - Result of high-pass filtering (with cut-off frequency of 0.008 Hz) and low-pass filtering (with Chebychev filter of order 6 and cut-off frequency of 0.08 Hz) of the rs-fMRI signal of healthy control.

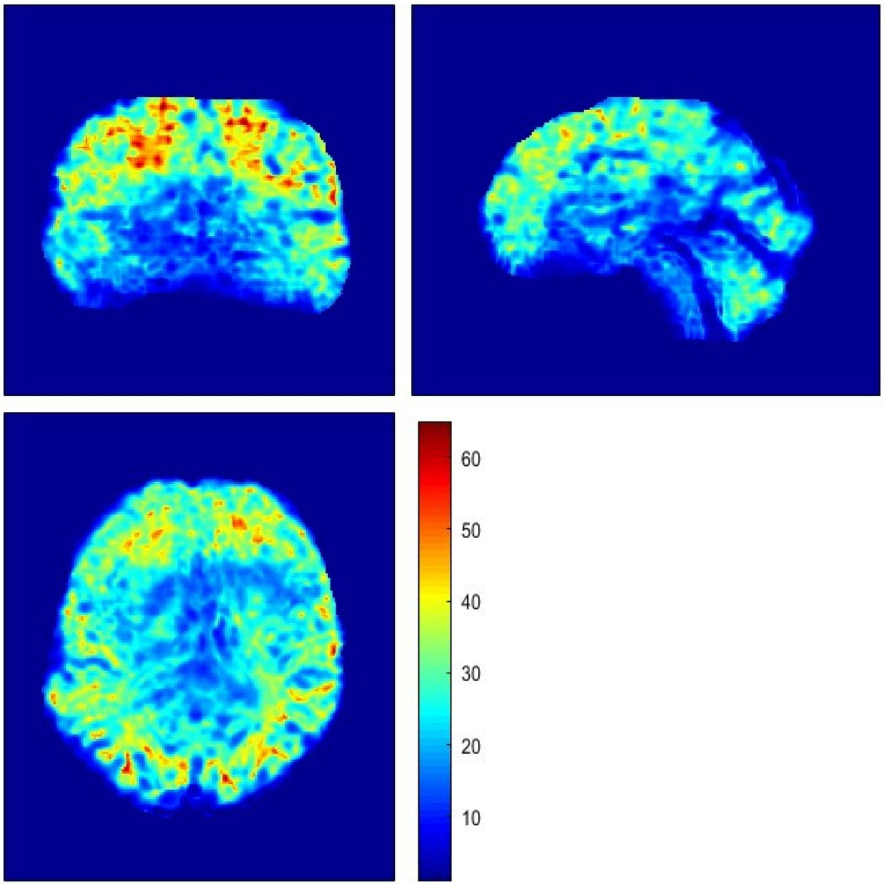

Figure 2.22 - Temporal signal-to-noise ratio (tSNR) obtained after low-pass filtering with a cut-off frequency of 0.008 Hz in the Parkinson's disease patient.

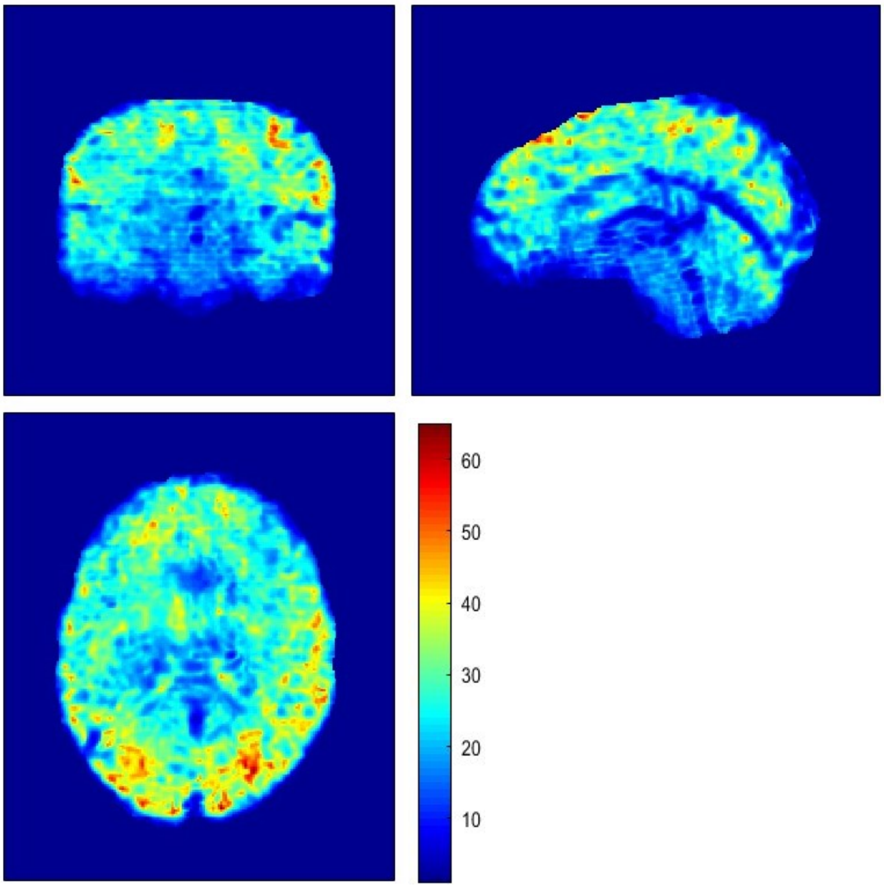

Figure 2.23 - Temporal signal-to-noise ratio (tSNR) obtained after low-pass filtering with a cut-off frequency of 0.008 Hz in the healthy control.

2.2.6 Intensity Normalization and Spatial Smoothing [a][b]

As a final step in the pre-processing pipeline, two processes were implemented: intensity normalization and spatial smoothing. These processes are essential to improve the performance of subsequent image analyses, such as functional connectivity analysis, in the context of this study. Their inclusion is common in the pre-processing phase of rs-fMRI data, as they contribute significantly to intra- and inter-subject comparability.

The main purpose of intensity normalization is to make acquisitions comparable with each other. In this context, the 4D EPI series of each subject were rescaled so that the average was 100.

On the other hand, spatial smoothing was implemented through convolution with a Gaussian kernel to increase statistical power and reduce noise. This process consists of averaging the signals of adjacent voxels, improving the signal-to-noise ratio (SNR). However, it must be considered that this operation tends to reduce spatial resolution, causing image blurring and diffusion of the activated areas into adjacent voxels. This is justified by the fact that neighboring brain voxels are often correlated in terms of functions performed and blood supply.

For spatial smoothing, a Gaussian filter was used as standard to convolve the fMRI data. This filter calculates a weighted average of the signals of neighboring voxels, with weights decreasing with increasing distance from the target voxel. The optimal kernel size was selected taking into account the resolution in space: given the size of the acquisition voxel (3x3x3.3), an FWHM width of 4 mm was chosen, which corresponds to the width of the reliable trigger signal.

2.3 Exploration of Functional Connectivity (FC)

Connectivity represents the study of the interaction between different brain regions, which can be categorized in terms of anatomical, functional, and effective connectivity:

- *Anatomical connectivity*. This form of connectivity involves the physical connections or interactions between different anatomical areas of the brain. Its analysis can be conducted using structural imaging techniques in combination with methods such as diffusion tensor tractography.[3]
- *Functional connectivity (FC)*. Functional connectivity seeks to establish links between spatial regions of interest based on the linear temporal correlation between neuronal signals.[3] This type of connectivity is widely examined using resting-state fMRI: several research studies (Biswal et al., 1995; Lowe et al., 1998; Xiong et al., 1999; Cordes et al., 2000; Greicius et al., 2003; Fox et al., 2005, 2006; Fransson, 2005; Vincent et al., 2006) have exploited this technique to obtain information on functional connectivity.[21]
- *Effective connectivity*. This more advanced level of functional connectivity analysis focuses on the underlying direct causal connections between functionally related regions. Effective connectivity is based on a mechanistic model that considers how data influence the neural system. It specifically refers to the influence that one neural system exerts on another.[3]

2.3.1 Coregistration on Atlas and FC Maps Extraction

A promising approach in research is the use of resting state functional connectivity (RSFC). This technique makes it possible to assess the synchronization of rs-fMRI signals between different brain regions while the subject is in a resting state inside the MRI machine, without requiring the performance of specific tasks. It should be noted that although RSFC is not a direct measure of anatomical connectivity, it is closely related to brain anatomy, thus providing information about the organization of large-scale brain circuits and is strongly associated with neural networks activated during specific tasks. Furthermore, RSFC is heritable and correlates with gene expression in the cerebral cortex, making it a valuable tool in estimating large-scale brain networks.[29]

Measuring functional connectivity involves calculating the temporal correlation between pairs of time series extracted from regions of interest (ROIs) or brain voxels.[k] The correlations observed in spontaneous BOLD fluctuations could reflect correlations between neuronal activity in different brain regions. In this context, the meantime course of a region of interest is used to generate a functional connectivity map by voxel-by-voxel correlation analysis.[21]

There are two main approaches to parcellating the brain using rs-fMRI: the local gradient approach and the global similarity approach. The local gradient approach, also known as boundary mapping, exploits the fact that RSFC patterns can vary significantly from one spatial location to another. These sudden changes can be detected by calculating local gradients in the RSFC patterns of the entire brain: this approach is particularly effective in delineating cortical areas, as the detection of abrupt changes in the RSFC is similar to the histological delineation of cortical areas.

On the other hand, approaches based on global similarity, such as mixture patterns and spectral clustering, group brain regions based on similarity in the temporal patterns of the rs-fMRI or RSFC patterns. These approaches often do not take spatial distance into account, which means that distant regions in the brain can be clustered in the same predefined network. However, some of these approaches try to avoid labelling spatially separate or neighboring regions separately. Since global similarity approaches try to aggregate voxels or vertices with similar temporal patterns, the resulting plots may appear very consistent in terms of connections, suggesting that they may reflect possible neurobiological units. Furthermore, these graphs can be used to reduce the complexity of rs-fMRI data in applications where it is difficult to process voxel-level data with the original resolution. In these applications, each graph can be represented by averaging the temporal signals of the voxels or vertices contained in the graph, and ideally, the voxels or vertices within the same graph should show very similar fMRI temporal patterns.

Local gradient-based approaches tend to generate consistent graphs because they implicitly favor consistency and discourage high RSFC gradients within a graph. In contrast, global similarity-based approaches explicitly seek to maximize the coherence of connections and, theoretically, may produce more cohesive graphs than local gradient-based approaches.

However, local gradient-based approaches appear to be more sensitive in detecting certain biological boundaries than global similarity-based approaches. Therefore, an integrated approach combining both methodologies could be useful for generating meaningful and neurobiologically informative brain maps, especially in applications requiring dimensionality reduction.[29]

In this study, to ensure the quality and reliability of the data before proceeding with functional connectivity analysis, rs-fMRI data were subjected to a censoring process in order to exclude outliers among the volumes, using an exclusion criterion based on a framewise displacement (FD) of 0.4 as a threshold.

Data registration was then performed with the cortical atlas of Schaefer et al. (2018), available at https://github.com/ThomasYeoLab/CBIG/tree/master/stable_projects/brain_parcellation, using SPM12 software. These new plots are based on the influential brain networks published by Thomas Yeo in 2011 and add further detail by partitioning the global networks using a gradient-weighted Markov random field model (gwMRF) that combines local gradient and global similarity approaches.[29] The plots come in different versions, which subdivide the cortex at different resolutions, up to a maximum of 1000 regions based on rs-fMRI.[1]

Two Nifti files for each parcel resolution, FSLMNI152_1mm and FSLMNI152_2mm, aligned to the 1 and 2 mm FSL MNI models respectively, can be found at the link provided. These parcels were derived from the fsaverage6 space and transferred into the MNI volumetric space. Each plot was associated with one of the seven or seventeen functional networks previously defined by Yeo et al.[g]

For the registration of the data in the present study, 200 cortical parcels, with a thickness of 1 mm, were considered, divided into 17 networks (Fig. 2.24 below).

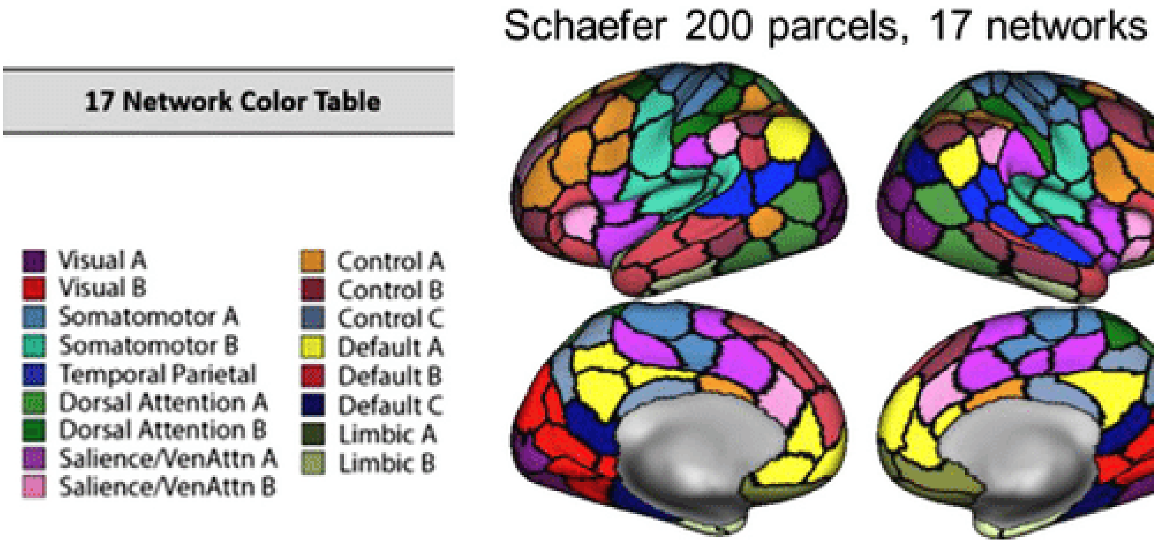

Figure 2.24 - Map of the division of the brain into 200 plots and 17 networks from Schaefer's atlas (2018).[30]

The results obtained by coregistering the previously described Schaefer atlas on the FLAIR-T2w structural image using the SPM12 software (see section 2.2.4.1 "*SPM12: Realignment and Coregistration*" for details regarding recording in SPM12) are shown in Fig. 2.25 on the following page, for the patient with Parkinson's disease (in the figure above) and the healthy control (in the figure below), respectively.

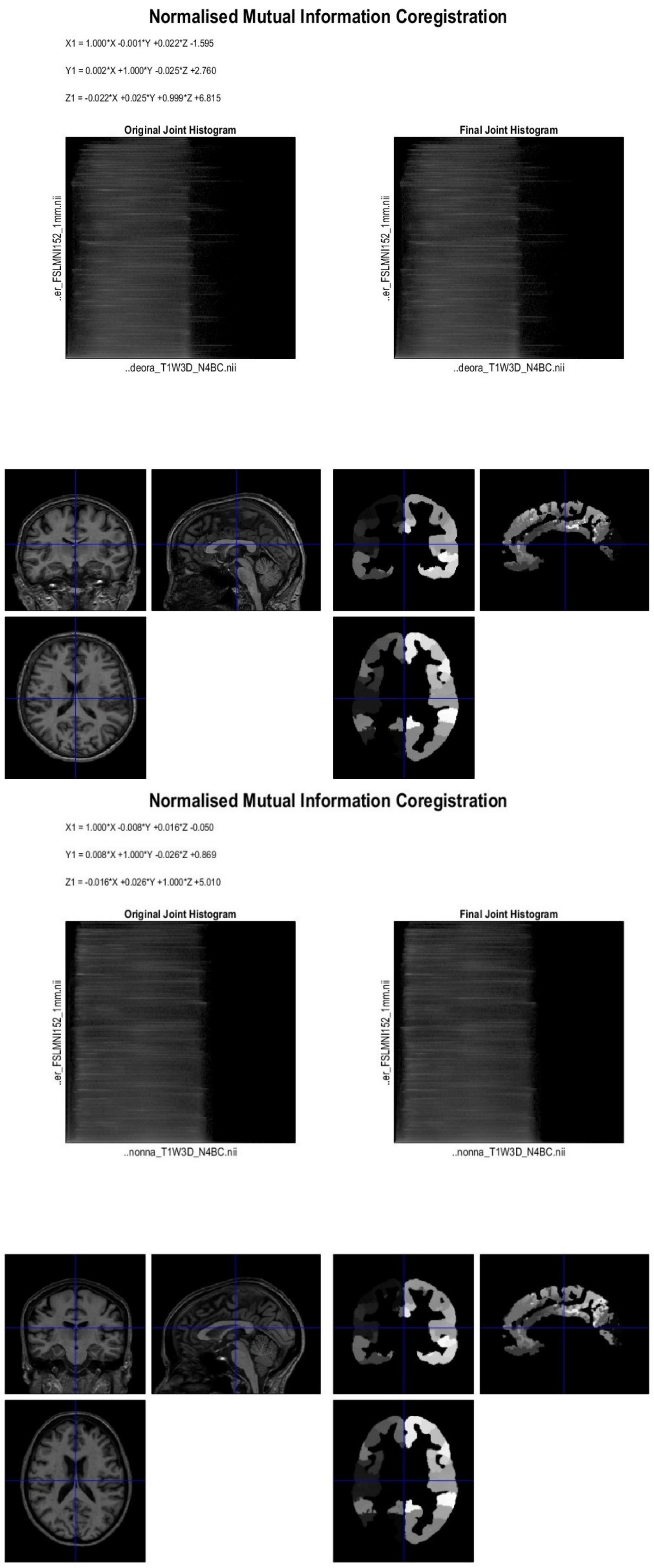

```
X1 = 1.000*X -0.001*Y +0.022*Z -1.595

Y1 = 0.002*X +1.000*Y -0.025*Z +2.760

Z1 = -0.022*X +0.025*Y +0.999*Z +6.815
```

```
X1 = 1.000*X -0.008*Y +0.016*Z -0.050

Y1 = 0.008*X +1.000*Y -0.026*Z +0.869

Z1 = -0.016*X +0.026*Y +1.000*Z +5.010
```

Figure 2.25 - Results of the registration of the Schaefer atlas (200 parcels, 17 networks) on the FLAIR-T2w structural image with SPM12 in the patient with Parkinson's disease (on the top) and the healthy control (on the bottom).

2.4 Intermediate Results and Evaluation Metrics

2.4.1 Evaluation Metrics: Temporal Signal-to-Noise Ratio (tSNR)

In science and engineering, signal-to-noise ratio (SNR) is a measure that compares the intensity of a desired signal with the background noise level. In the context of data obtained by magnetic resonance imaging (MRI), this evaluation is commonly used to compare different aspects of imaging hardware, imaging protocols and acquisition sequences. In this specific context, SNR is conceptualized by comparing the signal present in the MRI image with the noise floor of the image itself. Mathematically, the SNR represents the ratio of the average signal intensity measured in a region of interest (ROI) to the standard deviation of the signal intensity in a region that lies outside the area of the object under examination (i.e., a region where the tissue signal is absent) or the standard deviation of the noise distribution, if the latter is known.

SNR can be increased by variations in factors such as field of view, scanning parameters, magnetic field strength and layer thickness, as these parameters affect the noise floor. From another perspective, scanning hardware plays a significant role in the SNR levels of data from fMRI (functional magnetic resonance imaging). For example, SNR increases approximately linearly with magnetic field strength and is largely influenced by the receiving coils.

However, translating the concept of SNR from MRI images to fMRI images is a more complex process than it might seem. First, the noise in fMRI images does not correspond to the background noise in MRI images: in fMRI images, system noise affects the image, as does noise generated by the subject (such as heart beats, breathing, and movement) and by the activity performed itself. Using time series outside the brain to measure noise is not sufficient to capture all noise data.

Second, since the main goal of fMRI studies is to detect minute fluctuations over time, the SNR of the image may not be an adequate indicator. For this purpose, one can resort to the use of the temporal SNR (tSNR), described in Eq. 2.8 below, which considers the temporal (mean) trend of the signal.

$$tSNR = \frac{\bar{S}}{\sigma_N}$$

Equation 2.8 - Calculation of the temporal signal-to-noise ratio (tSNR) value as the ratio of the mean intensity, $\bar{S}$, to *the standard deviation of the background,* σ_N.

The baseline values are deeply influenced by the specific scanning parameters used to acquire the fMRI data. Moreover, since BOLD signal fluctuations are very small in magnitude, this definition does not provide any meaningful information about the strength of the activation signal, which makes it probably inadequate for task-related fMRI data: in fact, the higher the baseline value of the data, the lower the impact of the activation signal on the overall SNR. Therefore, the SNR value of a particular voxel alone is not sufficient to distinguish active from inactive voxels.

In contrast, tSNR can be particularly useful in the evaluation of fMRI under resting conditions, as it provides clear and easily interpretable information regarding the change in noise level in the brain: in practice, for each voxel, the mean and standard deviation of the corresponding time series are calculated and subsequently used to determine tSNR.
It should be emphasized that the interpretation of tSNR turns out to be applicable only in gray matter.[31]

2.4.2 B0 Field Distortion Correction: Warp Selection

To correct the B0 field distortions in the fMRI signal derived from the optimal combination of echoes in tedana, it is necessary to specify which warp to use in the *3dNwarpApply* command of AFNI.

Since the images were acquired in the anteroposterior (AP) direction, and the field distortions were computed with the *3dQwarp* command using the AP sequence as the base and the posteroanterior (PA) sequence as the source, we expect to apply the negative warp (MINUS) generated by the command itself to the signal. This choice is supported by the fact that the use of a MINUS warp results in applying the calculated displacement field between the source image (PA) and the base image (AP) to the source image itself, aligning the source image with the base image.

However, the application of the correct warp was investigated by comparing the tSNR maps of the signal, defined as the ratio between the mean value of the fMRI signal over time to its standard deviation, considering three conditions: application to the signal of the negative warp only (MINUS), the positive warp only (PLUS) and both warps together (PLUS+MINUS).

The results confirm that the correct warp to be applied to the fMRI signal to correct the B0 field distortions in a signal acquired in the AP direction is the negative warp, in the case of using the AP sequence as the base and the PA sequence as the source for the calculation of the displacement field. In fact, the tSNR map obtained by applying this warp to the signal shows higher tSNR values than the other conditions, demonstrating a prevalence of the signal of interest over noise (Fig. 2.26 below).

Further confirmation was obtained by comparing the correlation between fMRI signal in the three different applied warp conditions and the relative T1 structural image considering repere points: the highest correlation is again obtained with the application of negative warp (Fig.2.27 on the following page).

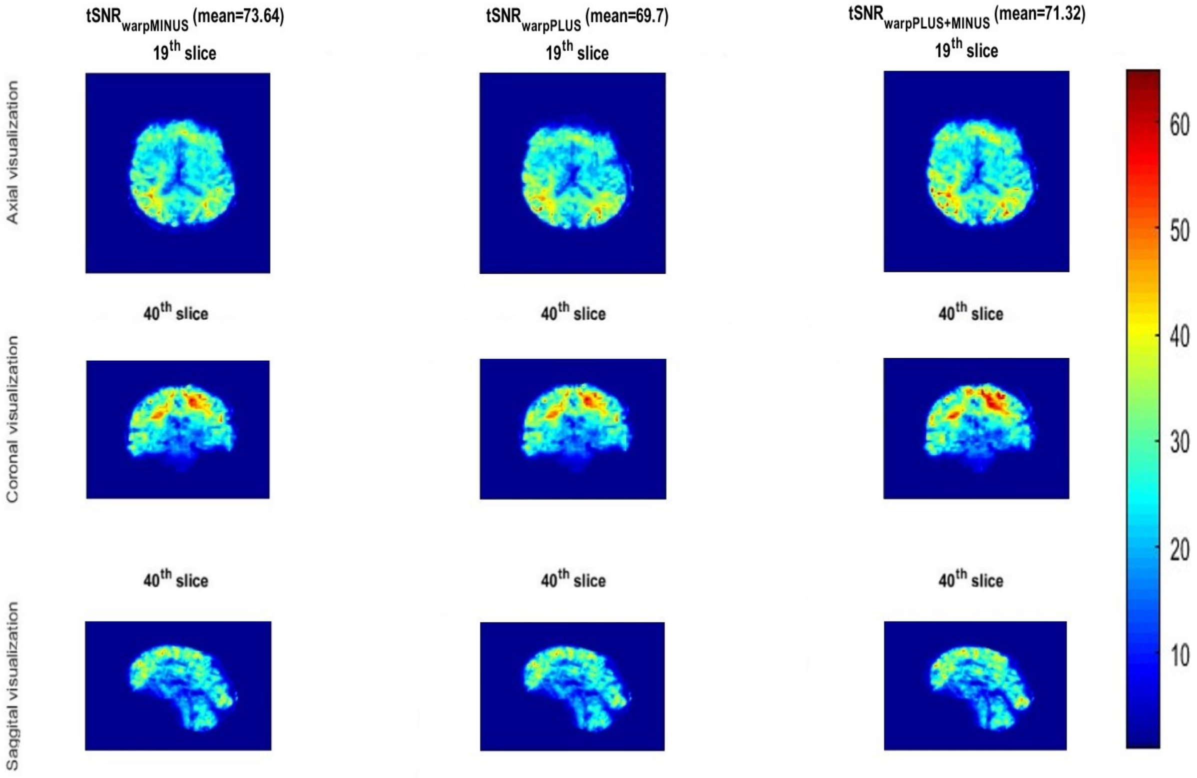

Figure 2.26 - Temporal Signal-to-Noise ratio (tSNR) maps of the fMRI signal with B0-field distortion correction using: negative warp (tSNR MINUS), positive warp (tSNR PLUS) or both (tSNR PLUS+MINUS) in the 3dNwarpApply command of AFNI. The results confirm that the correct warp to be applied to the fMRI signal to correct the B0 field distortions in a signal acquired in the AP direction is the negative warp, if the AP sequence is used as the base and the PA sequence as the source for the calculation of the displacement field with AFNI's 3dQwarp.

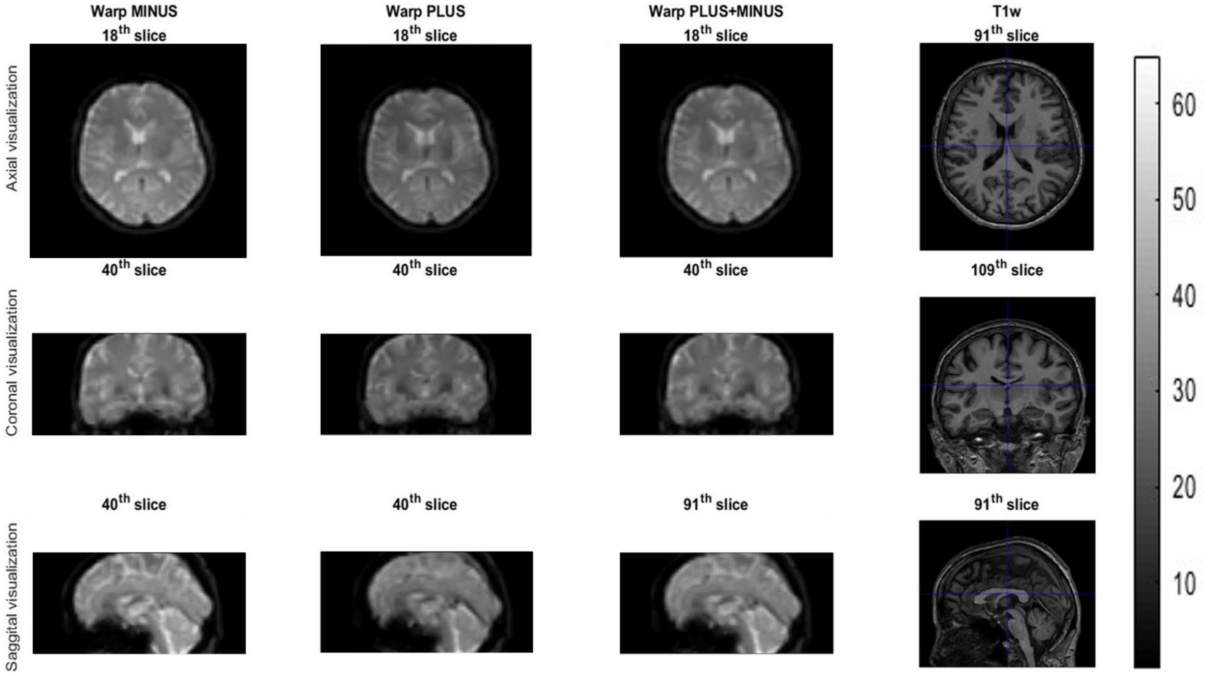

Figure 2.27 - Result of correcting the B0 field distortion of the fMRI signal using negative warp (MINUS), positive warp (PLUS) or both (PLUS+MINUS) in AFNI's 3dNwarpApply command. The fMRI signals are compared with the structural T1w image to verify that the brain structure is preserved during distortion correction. It is observed that with the application of the positive warp, strong distortions are introduced that lead to a brain structure that differs from the original, particularly in the frontal lobe (evident in the axial and sagittal views). The application of both warps draws more of the original structure but not completely, confirming instead that the application of the negative warp preserves the original cranial structure.

2.4.3 Comparison of Preprocessing Pipelines: AFNI vs FSL

TASK	TOOL	COMMAND	OPTIONS
HEAD-MOTION PARAMETER ESTIMATION	FSL	*mcflirt*	a. *mcflirt*: reference image for MoCo computed as mean image of motion corrected EPI of reference echo. b. *mcflirt*: estimation of head-motion, outputs transformation matrices for each BOLD volume, a parameters file (par, 3 rotations+3 translations) and *_meanvol.nii.gz used as REF
SLICE TIMING	FSL	*slicetimer*	a. write custom txt file with slice timings in fraction of TR to shift slices b. *slicetimer*: each raw echo EPI is slice-timed corrected
MOTION CORRECTION	FSL	*flirt*	a. *flirt*: motion correction of each BOLD volume with transformation matrices and REF computed in step 1)

Table 2.4 - commands used to implement slice timing and motion correction in FSL.

TASK	TOOL	COMMAND	OPTIONS
B0 DISTORTION ESTIMATION	FSL	*topup*	a. Resampling SE images to REF b. *topup*: estimation of the susceptibility induced field
B0 DISTORTION CORECTION	FSL	*applytopup*	*applytopup*: Unwarping of combined data

Table 2.5 - commands used to implement B0 distortions correction in FSL.

The same preprocessing steps performed with the AFNI software described above (slice timing and motion correction, before the optimal combination of the echoes in the tedana, and the subsequent correction of the B0 field distortions on the signal resulting from the combination of the echoes) were replicated in FSL (the FMRIB Software Library) with the corresponding commands, shown in Tab. 2.4 on the previous page and Tab. 2.5 above.

FSL is a comprehensive library of analysis tools for functional, structural and diffusion brain MRI data, written primarily by members of the Analysis Group, FMRIB, Oxford.[32]

For motion correction in FSL, rigid registration of each volume of the BOLD image with respect to the central volume was used, using the *mcflirt* function.[33]

mcflirt proceeds by loading the entire time series and selecting the central volume as the initial reference image. Then, an approximate search phase of motion parameters is initiated with a margin of 8 mm, using the specified cost function. This is followed by two additional search steps with a margin of 4 mm, with increasingly tight tolerances. All optimizations are performed with trilinear interpolation.

In the initial 8-mm search step, the transformation between the central and adjacent volumes is assumed to be identical. This initial transformation is then applied as an estimate of the transformation between the central volume and the volumes beyond the adjacent volume. In complex situations, this strategy does not penalize the quality of the final correction.

If averaged registration is adopted, the current motion correction parameters are applied to the time series. Then, the volumes are combined to create a new image model. Using this new averaged model, the three-stage correction step is performed again.

Finally, if a four-stage correction is opted for, an additional optimization step is performed using sinc interpolation (at the internal level) to achieve higher accuracy. However, this stage takes longer than the previous correction stage. On average, for a time series of 100 volumes, the correction phase should take about 10 minutes. It is important to note that this internal

interpolation is independent of the final resampling interpolation, specified via *sinc_final* or *spline_final*.
This approach has the advantage of precisely handling the final slices of a volume. Unlike other methods, in which voxels that leave the field of view (FOV) due to slight head movements are excluded or treated as null values, in this case volumes are extended by adding a duplication of the first and last slices in the z plane. This allows the data outside the FOV to be interpolated with appropriate values, preserving the maximum amount of useful information in the data.[h]

Slice timing correction was performed using the *slicetimer* function, a preprocessing tool specifically designed to mitigate sampling deviations present in EPI acquisition sequences, relative to individual slices.
The temporal evolution of each voxel is processed individually, and intensities are temporarily delayed reflecting the interpolated value of the signal at a reference instant common to all voxels. This process provides a snapshot of the data rather than a series of samples distributed across volumes. Synchronous interpolation, using a Hanning window as the kernel, is applied to each time series to compute the new interpolated values.
Since the slices were acquired in an interleaved order (0, 2, 4 ... 1, 3, 5 ...), the "--odd" option was enabled to make the appropriate correction.
In case the slices were not acquired in a regular order, it is necessary to use a slice sequence file or a slice timing file. When using a slice sequence file, simply create a text document containing a single number on each line: numbering begins with 1 for the first slice, 2 for the second, and so on.
In the case of a slice timing file, on the other hand, it is necessary to enter a value (one for each slice) on each line of the text file. The unit of measurement is TR, where 0.5 represents no displacement. Therefore, reasonable values are in the range [0,1].[i]

For the correction of B0 field distortions, however, the *topup* function was used, as well as a tool to estimate the induced susceptibility field.
The strategy employed by the *topup* method to determine the off-resonance susceptibility field is based on the use of at least two acquisitions with different acquisition parameters. This allows for distinct field mapping (distortions) between the acquisitions. A conventional example of this approach involves using two acquisitions with reversed polarity of the "blips" in the phase encoding. In practice, this means that the same magnetic field causes distortions in opposite directions in the two acquisitions.

With the help of these two images and knowledge of the acquisition parameters, the *topup* process attempts to estimate the susceptibility field by finding the field that, when applied to the two volumes, maximizes the similarity between the undeformed versions of the volumes. This similarity is measured by the sum of the quadratic differences between the images that have not been subjected to normalization. This particular measurement criterion allows the Gauss-Newton method to be used to jointly simulate the susceptibility field and any motion that might have occurred between the two acquisitions.[j]

The images obtained after preprocessing with AFNI and FSL were compared by generating temporal signal-to-noise ratio (tSNR) maps to assess the quality and consistency of the images processed by the two different approaches (see Chapter 3, section 3.1 "*Impact of the Preprocessing Pipeline").*

Chapter 3: Results

3.1 Impact of the Preprocessing Pipeline

3.1.1 Slice Timing, Motion Correction and B0 Field Distortions Correction

This study assessed the impact of AFNI and FSL software in combination with tedana, used to develop two different pre-processing pipelines in the analysis of multi-echo rs-fMRI data in a subject with Parkinson's disease and a healthy control.

The initial data pre-processing steps included slice timing and motion correction to mitigate the effects of temporal bias and subject motion during data acquisition. For both pipelines, the motion correction parameters were estimated using the third echo image (TE=30 ms). Next, in both pipelines, the tedana algorithm was used to optimally combine the echoes, generating a single pre-processed image with a better separation between BOLD and non-BOLD signals. Finally, the B0 field distortion correction was performed. This last step was performed using AFNI software in the pipeline where AFNI was used for slice timing and motion correction, while FSL software was used in the pipeline where FSL performed the same pre-processing steps.

To quantify the differences in impact at these stages between the two pipelines, histograms of the obtained tSNR maps were analysed after co-registering the images in structural space. These histograms represent the distribution of tSNR values between voxels, divided into intervals (or 'bins'), for each of the two pipelines. The number of intervals was determined by dividing the entire range of tSNR values into 50-unit intervals, and the data were normalised so that the sum of the bar heights was less than or equal to 1, thus representing the relative probability of occurrence in each interval.

The results show that in the patient with Parkinson's disease (Fig. 3.1 on following pages), the AFNI pipeline produced a mean tSNR value of 82.31, while the FSL pipeline generated a mean value of 88.46. In both cases, the histograms show a similar distribution of values with a higher concentration around the mean value. However, it should be noted that the AFNI pipeline has slightly more concentrated tSNR values between the voxels than the FSL pipeline, with higher probability density peaks around the mean, which explains the lower mean tSNR value.

In the healthy control subject (Fig. 3.2 on following pages), the AFNI pipeline produced a mean tSNR value of 125.37, while the FSL pipeline generated a mean value of 130.66. Again, the histograms show a similar distribution, with most values concentrated around the mean, but with more extensive tSNR values in the FSL pipeline. However, the probability density peaks around the mean are less pronounced than in the AFNI pipeline.

Comparing the performance of the two pipelines in the two subjects, it is observed that the healthy control has higher tSNR values than the voxels of the patient with Parkinson's disease. In fact, in the Parkinson's disease patient, both pipelines show lower probability density peaks than in the healthy subject, suggesting less variability in tSNR values. Furthermore, differences in the shape of the distributions between the two subjects suggest that the choice of one pipeline over the other affects the distribution of values differently.

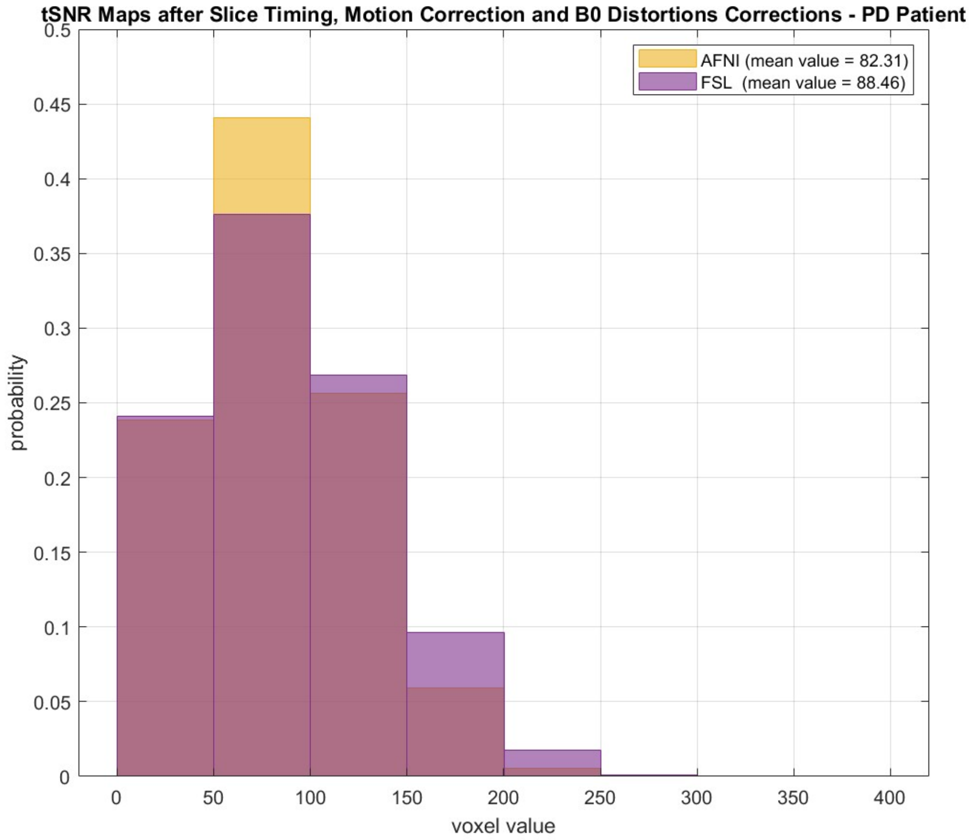

Figure 3.1 - Histograms of the temporal signal-to-noise ratio (tSNR) maps obtained with the AFNI preprocessing pipeline (in yellow) and FSL (in purple) after the slice timing, motion correction and B0 distortion correction steps for the PD patient.

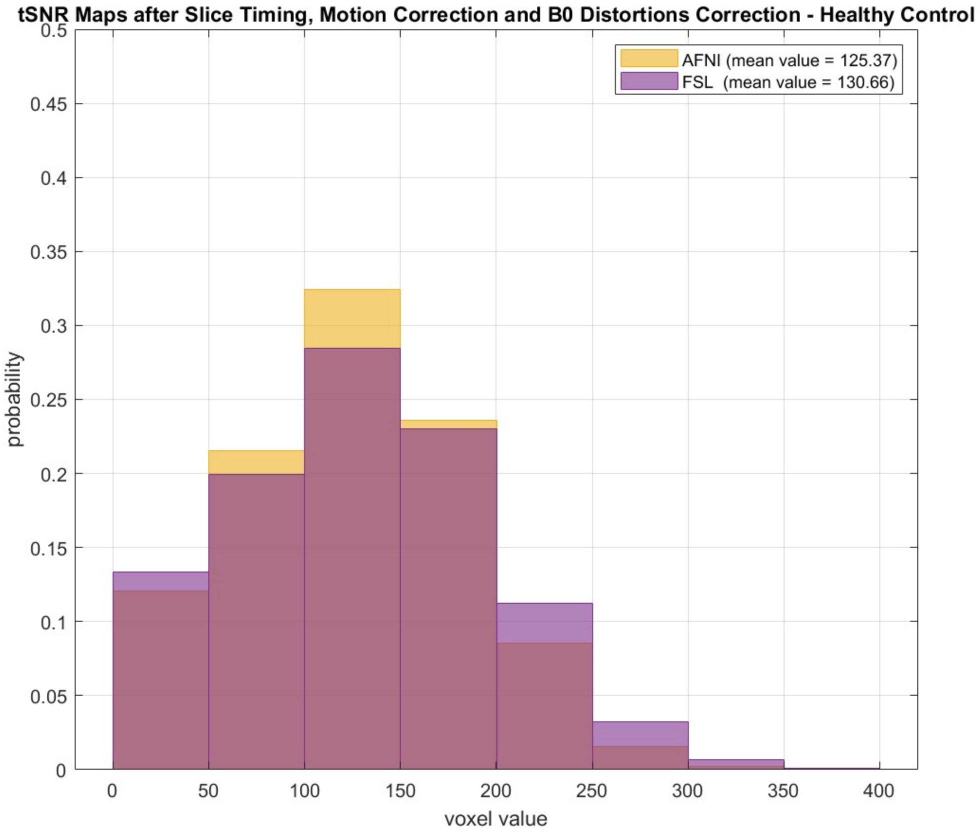

Figure 3.2 - Histograms of the temporal signal-to-noise ratio (tSNR) maps obtained with the AFNI preprocessing pipeline (in yellow) and FSL (in purple) after the slice timing, motion correction and B0 distortion correction steps for the healthy control.

The results show similar mean tSNR values and shapes of the distributions in both pipelines and for both subjects, with a larger deviation in the peak probability density and right tail of the distributions.

To better understand how pipelines affect data preprocessing, the latter was investigated by conducting an additional analysis considering the absolute differences between the tSNR maps obtained with the AFNI-based pipeline and that obtained with the FSL-based pipeline.

Studying the histograms of the differences in the absolute values (Fig. 3.3 on following pages), the differences in the distributions of tSNR values between the two pipelines are more pronounced in healthy control subjects (with a mean tSNR value of 29.64) than in subjects with Parkinson's disease (with a mean tSNR value of 19.94). It could be inferred from these results that pipelines may have a different impact on data variability, particularly in healthy subjects. However, since the study was based on only two subjects, it would be appropriate to verify these claims by including a larger group of subjects in the study.

In addition, visual inspection of images of the tSNR maps obtained with the two pipelines (Tab. 3.1 on the next page) shows a greater disparity in tSNR values within the primary motor cortex for both subjects, where the AFNI pipeline has higher values than the FSL-based pipeline. This could be explained by a different impact of the two softwares in correcting B0 field distortions or by a different impact of the coregistration programs, which differ in the two pipelines (SPM12 in the AFNI pipeline and ANTs in the FSL pipeline).
In addition, a divergence in tSNR map values is also observed within the parieto-occipital area. This phenomenon is prevalent only in the healthy subject, where higher tSNR values are found with the FSL pipeline than with the AFNI pipeline.

These results imply that the choice of preprocessing pipeline may affect the quality of tSNR maps, particularly when healthy subjects are involved, exerting an impact on the interpretation of functional MRI data in these types of subjects.
Researchers should therefore choose the pipeline to use based on the objectives of the study, such as the areas and population of interest. However, it would be advisable to conduct further statistical analysis to evaluate and determine the significance of these observed differences, possibly including a larger pool of subjects for analysis.

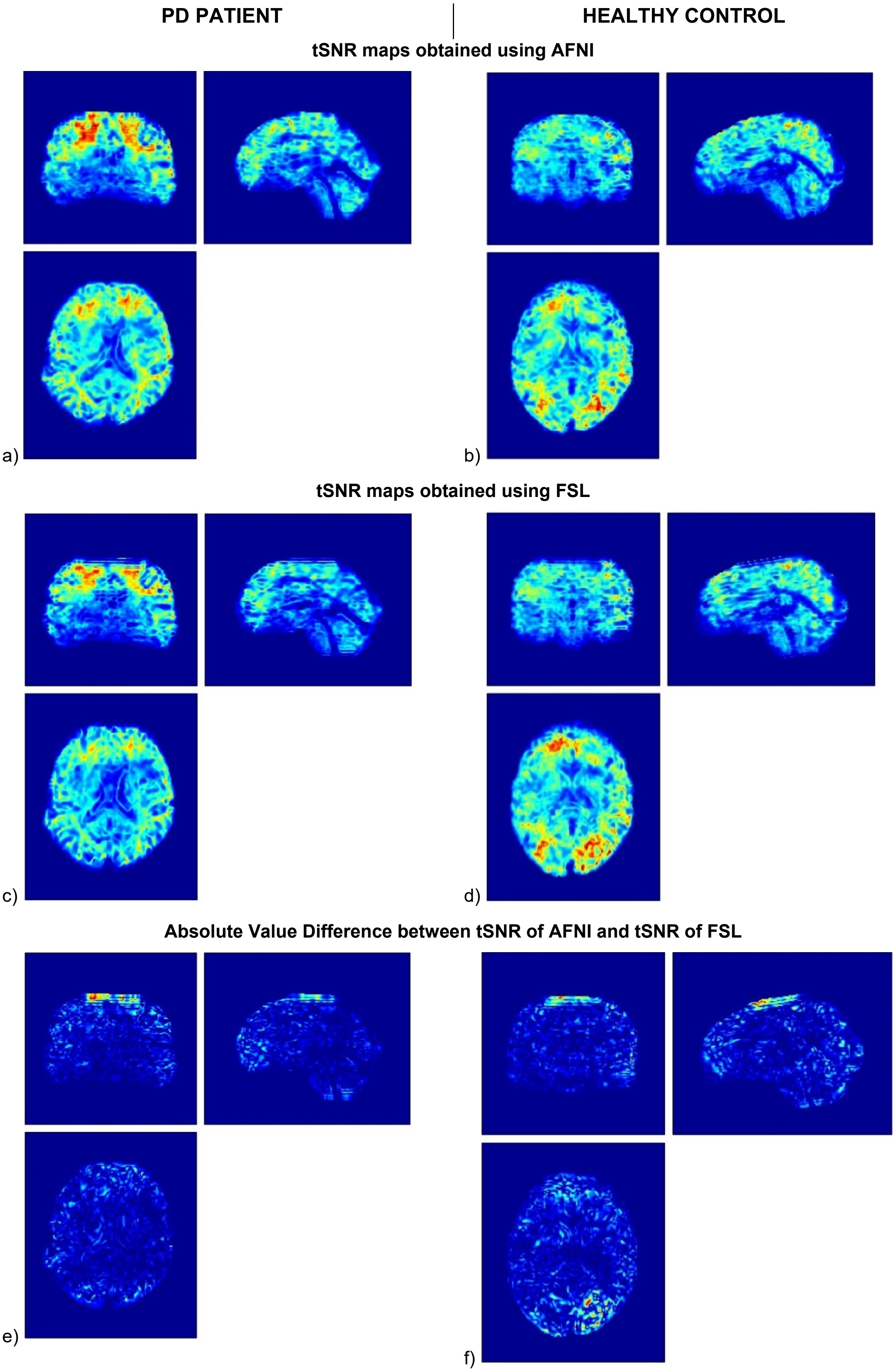

Table 3.1 - Summary of results obtained after slice timing, motion correction and B0 distortions corrrection steps with AFNI and FSL pipelines. Fig.s a) and b) show the tSNR maps obtained with AFNI, while Fig.s c) and d) show those with FSL, respectively for PD and HC subjects. Fig.s e) and f) show the absolute value difference between the previously described maps for PD and HC subjects, respectively.

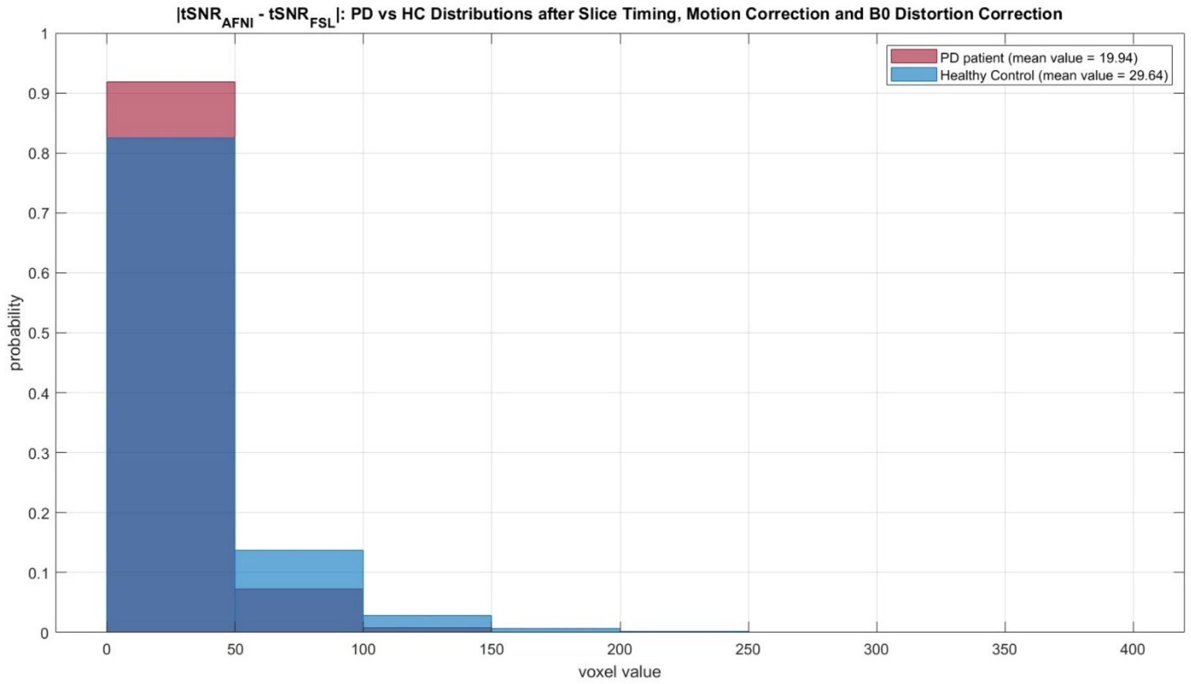

Figure 3.3 - Comparison of the distributions of absolute differences between the temporal signal-to-noise ratio (tSNR) maps obtained with the AFNI pre-processing pipeline and with FSL after the slice timing, motion correction and B0 distortion correction steps for the patient with Parkinson's disease (in red) and the healthy control (in blue).

3.1.2 Overall Comparison of Preprocessing Pipelines

The comparison between the AFNI- and FSL-based pre-processing pipelines was also performed after all data pre-processing steps were completed, which included regression for white matter and cerebrospinal fluid using the General Linear Model (GLM), high-pass filtering at 0.008 Hz and low-pass filtering with a Chebyshev filter of order 6 at 0.08 Hz, followed by normalization and spatial smoothing at 4 mm FWHM on both subjects.

Again, tSNR maps obtained from both pre-processing pipelines on both subjects were analyzed using histograms for quantitative evaluation.

On average, the tSNR values obtained using the FSL preprocessing pipeline appear to be higher, with an average of 545.67 for the patient with Parkinson's disease and 636.82 for the healthy control. In comparison, the values obtained by using AFNI show an average of 446.43 and 594.11, respectively (as shown in Figs. 3.4 and 3.5 on the next page). These results suggest a general tendency for the FSL pipeline to produce tSNR maps with higher values for both groups of subjects.

However, a closer look at the histograms reveals some variability in the distribution of tSNR values obtained from both pipelines on both subjects. In particular, the distributions in the healthy control show a long tail toward the higher values, suggesting the presence of some regions with higher-than-average tSNR values. This means that both pipelines can detect brain regions with high tSNR.

The most pronounced differences are also found this time around the average tSNR values, where the AFNI pipeline shows higher peaks. In addition, the distribution of tSNR values shows a more pronounced right tail in the FSL pipeline than in AFNI, especially in the subject with Parkinson's disease. Indeed, in the latter, AFNI shows much smaller tSNR values than the FSL pipeline, although with higher peak probability densities. This suggests that the FSL pipeline may identify regions of even higher tSNR in individuals with Parkinson's disease than the AFNI pipeline.

These differences could be relevant in the context of functional MRI image analysis, as regions with higher tSNR could affect the ability to detect brain activity.
However, it is again emphasized that to have confirmation of these results, the pool of subjects to be analyzed should be expanded, as with only two subjects, the results cannot be considered representative for the entire population.

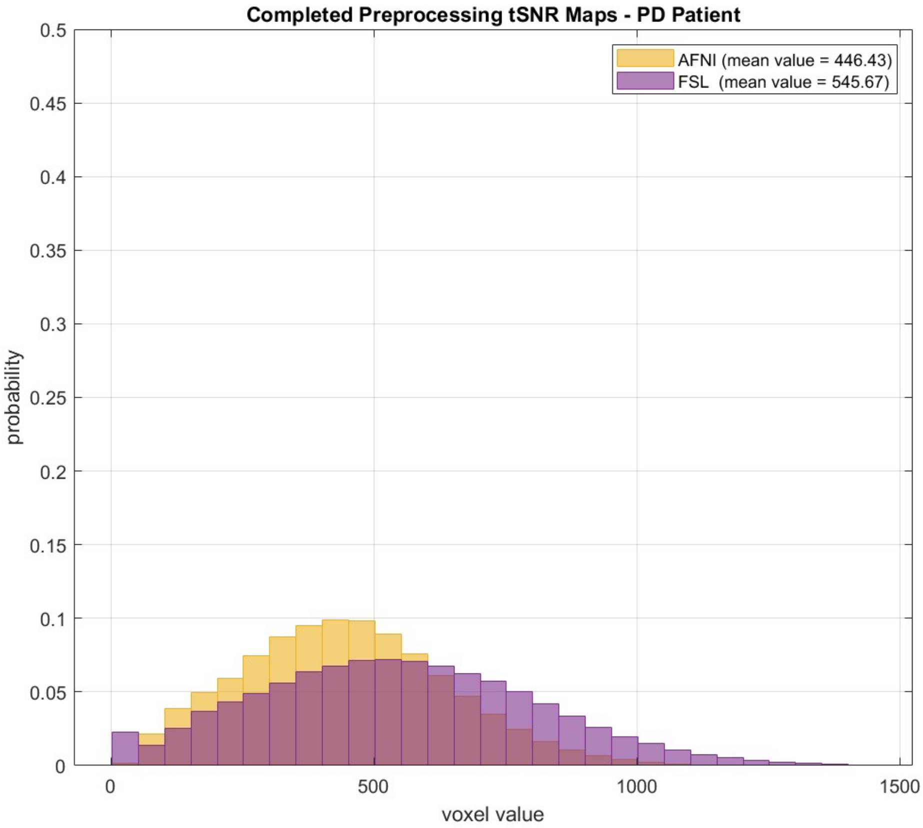

Figure 3.4 - Histograms of the temporal signal-to-noise ratio (tSNR) maps obtained with the preprocessing pipeline of AFNI (in yellow) and FSL (in purple) after completing the preprocessing for the subject with Parkinson's disease.

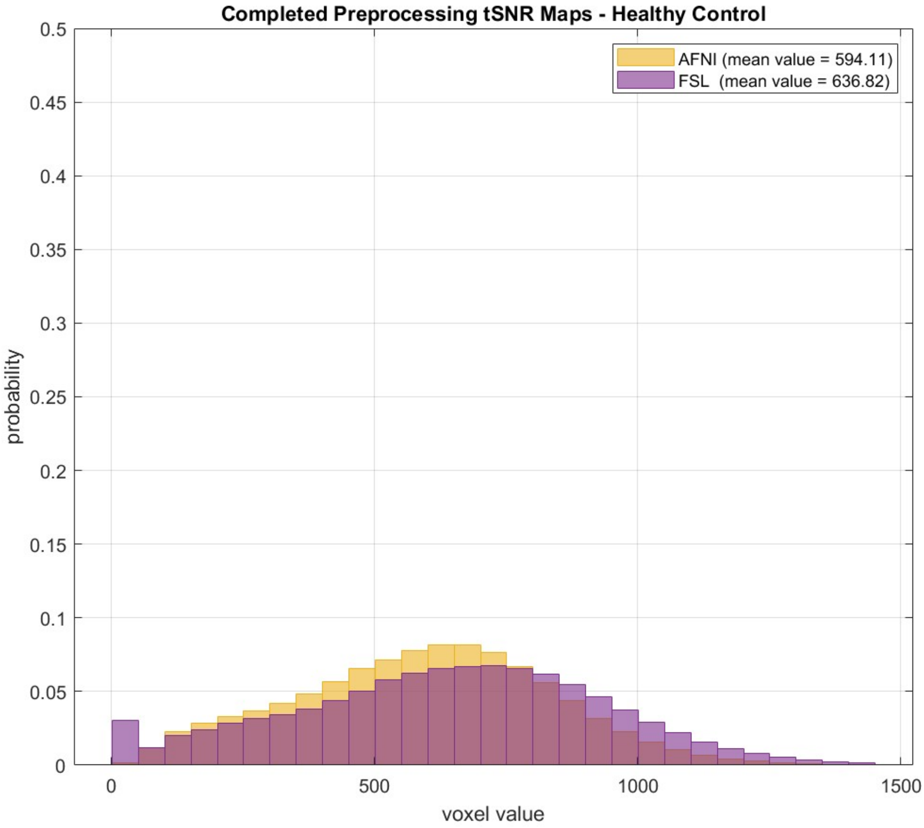

Figure 3.5 - Histograms of temporal signal-to-noise ratio (tSNR) maps obtained with the preprocessing pipeline of AFNI (in yellow) and FSL (in purple) after completing preprocessing for the healthy control.

Examining the absolute differences between the tSNR maps obtained with the AFNI and FSL pipelines for the two study subjects, it was observed that the mean absolute differences between the tSNR maps obtained with the two pipelines was 142.25 in the case of the patient with Parkinson's disease and 124.9 in the healthy control subject. These results show that, overall, the two pipelines produce tSNR maps with differences between them in both subjects, although with a smaller difference in the healthy control subject than in the Parkinson's patient.

Analyzing the histograms of absolute differences between the tSNR maps obtained with the two pipelines (Fig. 3.6 on the next page) shows that most of the differences are concentrated in relatively low values, with a long tail toward higher values. This suggests that the two pipelines are capable of generating tSNR maps with variations in certain brain regions.

Visual inspection of the images of the tSNR maps (Tab. 3.2 on the following pages) also reveals that, in both cases, higher brain regions, particularly the parieto-frontal area, are excluded in the images obtained with the FSL-based pipeline. Although this can produce tSNR maps with better values overall than the AFNI-based pipeline, the clipping of some regions could be a significant limitation, especially when specific brain areas, such as those related to motor functions, are to be studied.

To address this problem, it would be necessary to analyze in more detail the coregistration and regression implementation steps via GLM, which differ between the two pipelines.
It is also pointed out that the optimal echo combination step could also introduce divergences in the results: performing it via *t2smap* produces different results than the combination of echoes obtained during the denoising process via tedana, where it is provided in output already masking the brain based on the voxels considered reliable. In addition, the results could also vary depending on the space over which it is performed.

In both pipelines, the optimal combination of echoes was performed using *t2smap*, which considers temporal variations in brain tissue susceptibility, which can vary greatly from subject to subject. Rather, the main difference between the two pipelines lies in the fact that coregistration in structural space was performed at two different points in time: in the AFNI pipeline, it was performed after correction of B0 field distortions, whereas in the FSL pipeline all preprocessing steps were conducted in functional space, performing coregistration in structural space only at the end of the process.

The greater evidence of motor areas in the tSNR maps obtained with the AFNI pipeline, both after correction for B0 field distortions and at the end of the data preprocessing steps, suggests that this may be a more appropriate choice for studying brain regions related to motor activities or other specific functions.

Overall, the results obtained indicate that the choice of pre-processing pipeline may influence the distribution of tSNR values. In particular, the FSL pipeline shows a tendency to produce higher values than the AFNI pipeline at various stages of data pre-processing, although it struggles to capture all brain areas, excluding, for example, the primary motor cortex. However, considerable data variability is evident in both pipelines, demonstrating their success in improving signal quality in both subjects.

These results underscore the importance of considering the specific goals of the analysis, the brain regions of interest, and the population of subjects under study when selecting the data pre-processing pipeline, as these differences may influence the interpretation of the data. It is again suggested that further statistical analysis and the inclusion of more subjects in the study be considered to assess in more detail the significance of these divergences in the data.

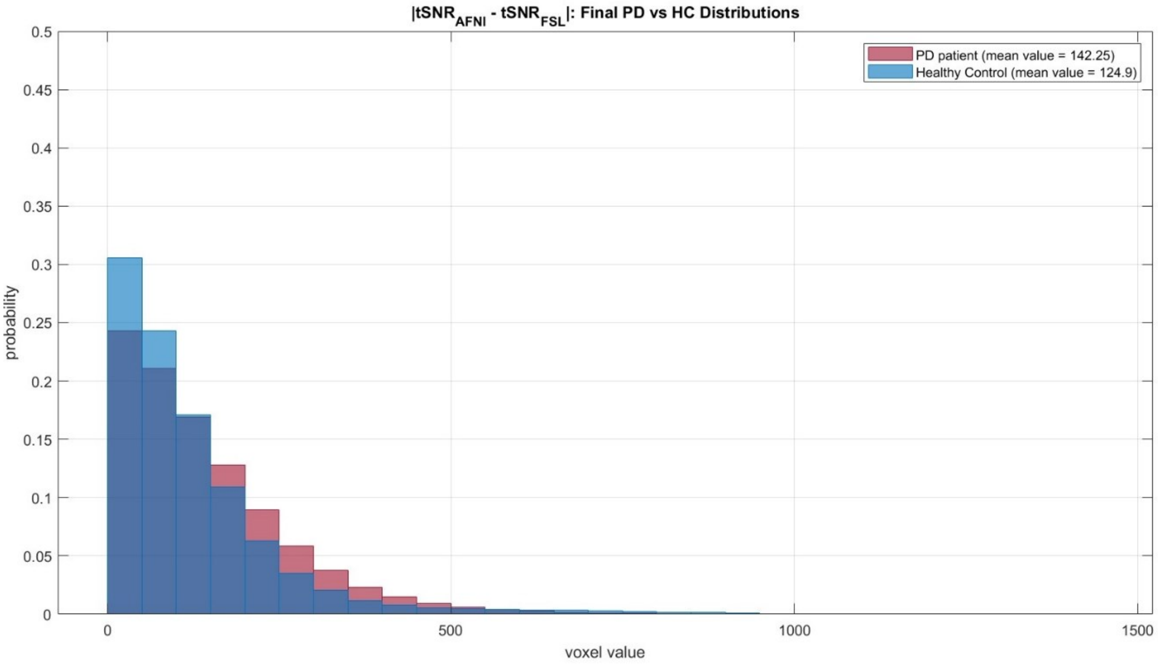

Figure 3.6 - Comparison of the distributions of the absolute differences between the temporal signal-to-noise ratio (tSNR) maps obtained with the AFNI pre-processing pipeline and with FSL after completing the pre-processing for the patient with Parkinson's disease (in red) and the healthy control (in blue).

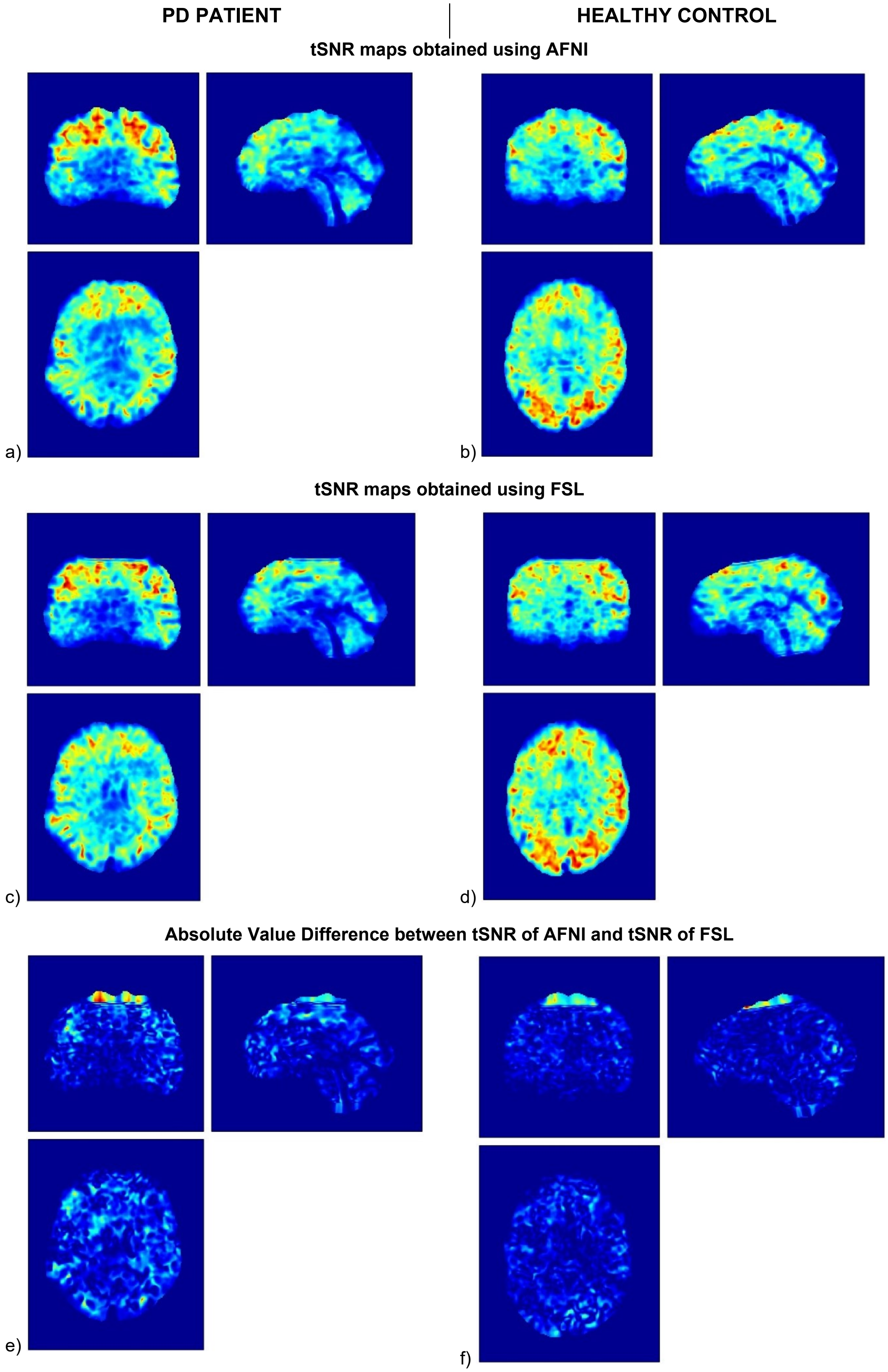

Table 3.2 - Summary of the results obtained after preprocessing with the AFNI and FSL pipelines. Fig. a) and b) show the tSNR maps obtained with AFNI, while Fig. c) and d) show those with FSL, for PD and HC subjects respectively. Fig. e) and f) show the absolute difference between the previously described maps for PD and HC subjects, respectively.

3.1.3 Effect of the AFNI Pipeline on tSNR

Fig. 3.7 on the following page provides a clear representation of the increase in mean tSNR through the different phases of the AFNI-based rs-fMRI image processing pipeline, showing a significant improvement in data quality.

After performing the optimal combination step with tedana, which allowed the optimal fusion of the three rs-fMRI echoes, tSNR values of 67.79 for the patient with Parkinson's disease and 100.44 for the control subject were obtained. This combination of echoes made it possible to exploit the information from the shorter times to recover the signal in the drop-out regions, resulting in a higher average tSNR than the images obtained from the single echoes (see Fig. 2.9 in Section 2.2.2 "*Tedana: Optimal Combination of Echoes*"). This suggests the effectiveness of integrating the echoes into a single image.

Subsequently, with the application of the B0 field distortion correction in AFNI, the mean tSNR further improved for both subjects. Compared to the previous phase, there was a percentage increase of 21.41% for the patient with Parkinson's disease and 24.83% for the healthy control. These results confirm the importance of this correction to compensate for magnetic variations in the electromagnetic field, ensuring greater accuracy of the rs-fMRI images.

The application of regression with the General Linear Model (GLM) for white matter (WM) and cerebrospinal fluid (CSF) in the next step showed a further improvement in signal quality, especially for the subject with Parkinson's disease. The percentage increase in mean tSNR values was 106.06% for the Parkinson's disease patient and 51.97% for the healthy subject compared to the previous B0 distortion correction phase.

The "HP&LP Filtering" phase shown in the figure, comprising high-pass filtering with a cutoff frequency of 0.008 Hz and low-pass filtering with a cutoff frequency of 0.08 Hz, further contributed to the increase in mean tSNR. At this stage, there was a percentage increase of 78.30% for the patient with Parkinson's disease and 65.15% for the healthy control compared to the previous regression phase.

Finally, the application of Spatial Smoothing with FWHM=4mm resulted in an overall percentage increase in mean tSNR of 46.98% for the patient with Parkinson's disease and 66.78% for the control subject compared to the temporal filtering phase.

The mean tSNR values reached considerable levels during this process, particularly for the control subject, where a final mean tSNR of 594.11 was reached.
Although the healthy control had a better initial tSNR, the AFNI pipeline proved to be particularly efficient in improving the tSNR for the Parkinson's disease patient as well, especially during the regression phase for the white matter and CSF, where the average tSNR value increases from 82.31 to 169.94.

These results clearly and quantifiably demonstrate the effectiveness of each pipeline step in improving signal quality, reducing noise, and improving signal sensitivity. Furthermore, they emphasize the importance of each step in the process of improving rs- fMRI data.

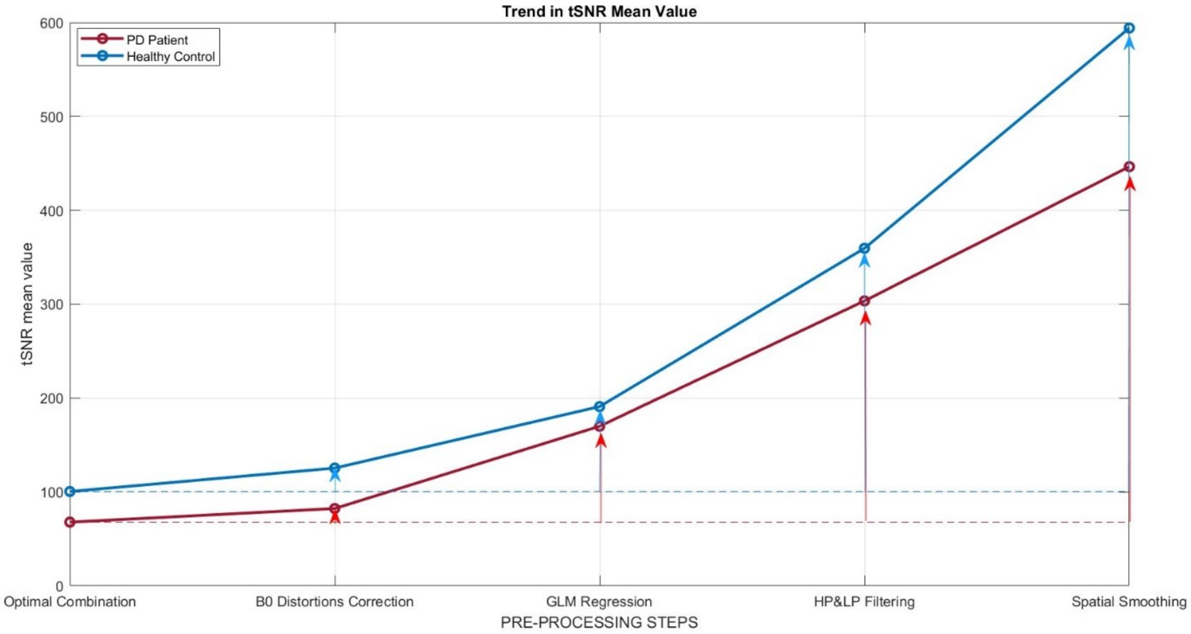

Figure 3.7 - Increased mean values of tSNR in the various stages of the AFNI software-based pipeline for the patient with Parkinson's disease (red) and the healthy control (blue), respectively. From the B0 field distortion correction step, rs-fMRI images coregistered on structural space are considered.

3.2 Functional Connectivity Analysis

After pre-processing the rs-fMRI data, the images output from the AFNI-based pipeline were chosen to conduct a functional connectivity (FC) analysis.

The choice of pipeline was justified by the fact that although the average tSNR values obtained from the FSL pipeline were higher, signals attributable to the primary motor cortex were excluded to a greater extent. In order not to neglect this area from the analyses, the AFNI-based pipeline was therefore chosen between the two, as it provided an acceptable compromise between a good yield in the average tSNR value and the ability to capture a wider range of areas.

Considering therefore the two previous subjects, the Parkinson's disease subject and the healthy control subject, after pre-processing their data with the AFNI pipeline, a Sheafer atlas was used to subdivide the brain images into 200 parcels, which in turn were grouped into 17 distinct brain networks.

To assess functional connectivity, time activity curves (TACs) were extracted for each of the 200 parcels, and correlations between them were subsequently calculated. This process led to obtaining a functional connectivity matrix reflecting the relationships between the different brain regions, of which the Z-Fisher transform was considered in order to obtain a more stable representation of the correlations and greater comparability between subjects. To consider only the most significant correlations, a statistical significance criterion was applied, keeping only those correlations with a p-value of less than 0.05.

In the patient with Parkinson's disease, the strongest positive correlations were found between the Dorsal Attention Network (dorsalAttentionB in Fig. 3.8) and the Sensorimotor Network (somatomotorA in Fig. 3.8) and vice versa, both in the left hemisphere. The most significant negative correlation in absolute value was instead observed between the Salience Ventral Attention Network (salienceVentralAttentionA in Fig. 3.8) of the left hemisphere and the Visual Peripheral Network (visualPeripheral in Fig. 3.8) of the right hemisphere, and vice versa.

In the healthy control subject, a similar pattern of positive correlations emerged between the Dorsal Attention Network (dorsalAttentionB in Fig. 3.9) and the Sensorimotor Network (somatomotorA in Fig. 9) of the left hemisphere, whereas the most pronounced negative correlation in this case occurred between the Default Mode Network (defaultB in Fig. 3.9) of the left hemisphere and the orbitofrontal cortex of the limbic system (limbicOrbitofrontal) of the right hemisphere, and vice versa.

The Dorsal Attention Network (DAN) involves voluntary orientation (top down) and selective attention, whereas the Sensorimotor Network (SMN) is central to detecting and processing sensory input and preparing and executing motor functions.[9]

The positive correlation between Dorsal Attention Network and Sensorimotor Network in both subjects is consistent with what was expected, as, considering that data acquisition occurred in both subjects in a resting state by calling them to attention to check their waking state, it could reflect their concomitant activation during the normal waking and attention states.

This result could indicate that when people are awake and alert, the cognitive and motor activities involved in spatial attention (Dorsal Attention Network) and sensory and motor information processing (Sensorimotor Network) are more effectively integrated. The positive correlation between these networks in this context therefore suggests that these neural networks work together in a synchronized manner when individuals are awake and alert, which is consistent with their role in regulating spatial attention and sensory and motor information processing.

The negative correlation in opposite hemispheres detected in patients with Parkinson's disease between the Salience Network (SN), which detects and responds to salient behavioral events, and the Visual Network, which is involved in processing visual information, could be indicative of a deficit in visual stimulus recognition, suggesting that the PD patient shows less functional communication between these two neural networks than would be expected in a healthy individual. [9] This could indicate that the PD patient may have difficulty recognizing or giving importance to salient visual stimuli.

A negative correlation could therefore reflect an impaired ability of the SN to pick up on relevant visual cues or respond to them appropriately, resulting in less co-ordination between the SN and the Visual Network.

Furthermore, the fact that it occurs between opposite hemispheres could reflect an asymmetry in brain response in PD patients, which could thus be indicative of specific Parkinson's disease alterations in different parts of the brain.

By contrast, the negative correlation found in the healthy individual between the Default Mode Network (DMN), involved in introspection and the wandering mind, and the orbitofrontal cortex, involved in functions related to emotions and decision-making, is consistent with what one would expect to find in a healthy individual.

The DMN is in fact known to be anticorrelated with certain brain networks involved in external or attentional tasks when the brain is in a state of wakefulness and attention. This anticorrelation reflects the alternation between DMN and orbitofrontal cortex activity, and the fact that it occurs in opposite hemispheres indicates that they are active at different times or in response to different tasks. [9]

The negative correlation could also reflect a dynamic balance between times when the brain is more oriented towards introspection and times when it is more oriented towards emotional response or decision-making, as could also be specific to the experimental conditions used in the study. For example, it could reflect a response to specific tasks or stimuli that require a change in the activity of these brain regions.

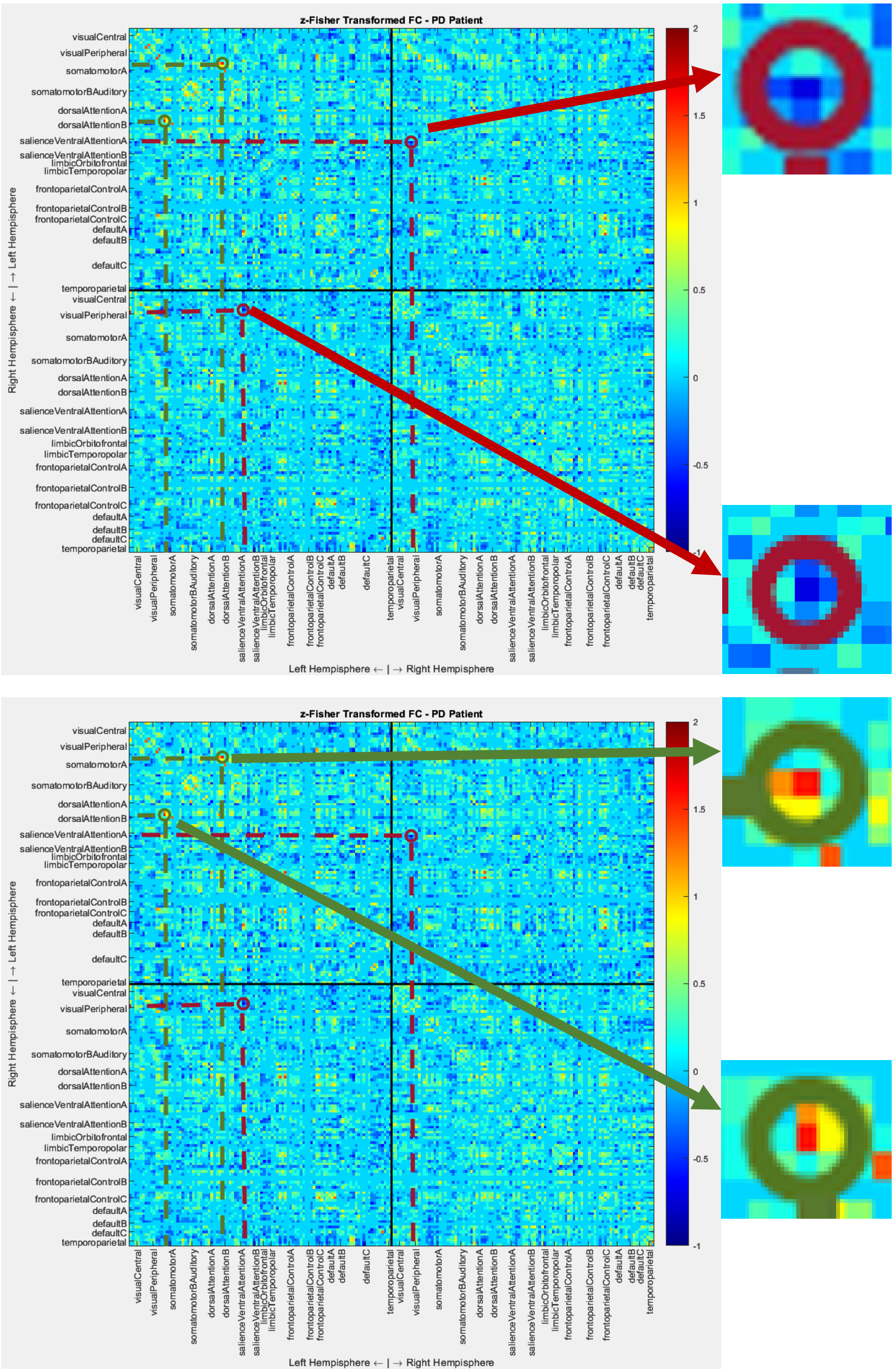

Figure 3.8 - Statistically significant correlations (p<0.05) found in the subject with Parkinson's disease. In the upper image the positive correlations (in green) between Dorsal Attention Newtork and Sensorimotor Network belonging to the same hemisphere are highlighted, while in the lower image the negative correlations (in red) between Salience Ventral Attention Network and Visual Peripheral Network belonging to opposite hemispheres are highlighted.

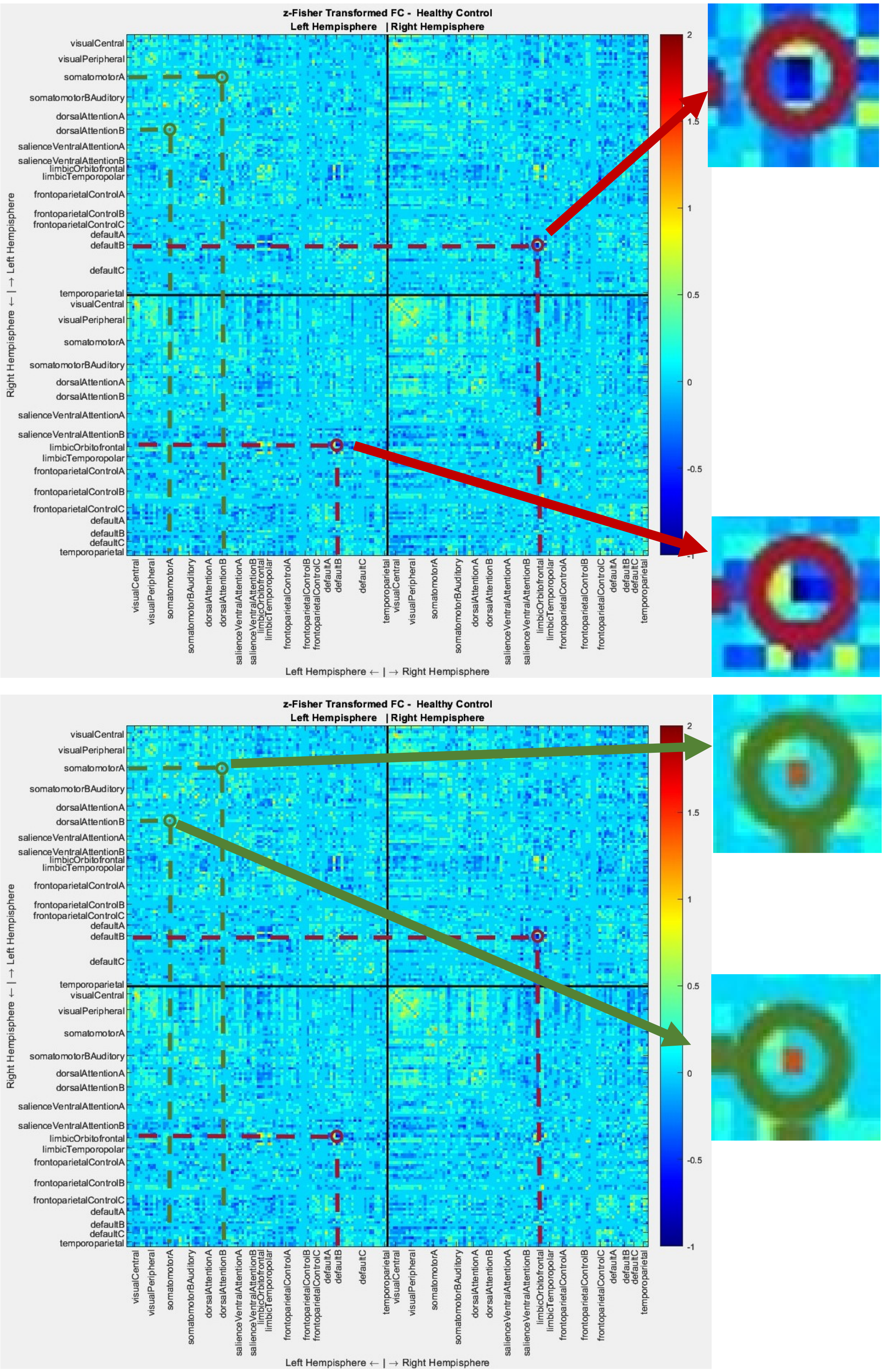

Figure 3.9 - Statistically significant correlations (p<0.05) found in the healthy control. In the upper image the positive correlations (in green) between Dorsal Attention Newtork and Sensorimotor Network belonging to the same hemisphere are highlighted, while in the lower image the negative correlations (in red) between Default Mode Network and orbitofrontal cortex of the limbic system belonging to opposite hemispheres are highlighted.

Chapter 4: Discussion

4.1 Summary of Results

This study consisted of two phases: in the first part, two different pipelines, based on AFNI and FSL software, were tested in a subject with Parkinson's disease and in a healthy control to pre-process multi-echo rs-fMRI data; in the second part, after selecting the most appropriate pipeline for the purpose, the data pre-processed by this pipeline were used to conduct a functional connectivity analysis.

The results for the first part of the study indicated that both pipelines can produce similar tSNR maps in terms of mean values and distribution of values, although with slight differences.
A tendency was observed for the FSL pipeline to generate slightly higher mean tSNR values with greater variability than those generated by the AFNI-based pipeline. The discrepancy in the output of the two pipelines was found to be greater for the subject with Parkinson's disease than for the healthy control, as evidenced by an absolute difference between the tSNR maps that was greater at both mid-pre-processing and completed pre-processing.
In addition, the pipelines showed a different impact on the representation of some brain regions, particularly motor areas that were excluded in the FSL pipeline.

In general, these results suggest a potential influence by the choice of pipeline on the quality of tSNR maps and, consequently, on the interpretation of functional fMRI data preprocessed with it. Selection of the preprocessing pipeline should therefore be based on the specific objectives of the study to be conducted and the population of subjects to be analyzed, considering observed differences.
Further statistical analysis, possibly on a larger sample of subjects, is recommended to assess the significance of these differences and improve understanding of the impact of pipelines on rs-fMRI data quality.

For the second part of the study, preprocessed images from the AFNI-based pipeline were chosen to conduct a functional connectivity (FC) analysis.
Among the two pipelines studied, in fact, the AFNI pipeline offered an acceptable compromise between overall signal quality and the ability to capture brain areas, particularly the primary motor cortex, in a more extensive manner.
After using this pipeline, the brain images were divided into 200 regions, grouped into 17 distinct brain networks. Next, correlations between the activity over time (TAC) curves of each

region were calculated, generating a functional connectivity matrix, of which only statistically significant correlations (with a p-value less than 0.05) were considered.

In both subjects, strong positive correlations were found between the Dorsal Attention Network (DAN) and the Sensorimotor Network (SMN), both in the left hemisphere.
In addition, strong negative correlations were observed between networks belonging to opposite hemispheres, particularly between Salience Network (SN) and Visual Network in the patient with Parkinson's disease, and between Default Mode Network (DMN) and orbitofrontal cortex of the limbic system in the healthy control subject.

These results suggest potential variability in functional connectivity between healthy individuals and patients with Parkinson's disease, with possible implications for visual perception and response to salient stimuli. The positive correlation between the Dorsal Attention Network and Sensorimotor Network in both groups suggests a more effective integration of cognitive and motor activities during wakefulness and attention. On the other hand, negative correlations between brain networks in opposite hemispheres may reflect asymmetries in brain responses in Parkinson's patients and experimental condition-specific activity dynamics.

In this study, the importance of detailed comparative analysis between pre-processing pipelines before conducting a specific study emerged to optimize data quality and ensure accurate results in the analysis of multi-echo rs-fMRI data. In this context, it has indeed been shown that pipelines based on different software have different performance depending on variables such as subject groups or brain regions analyzed. These factors should indeed be given due consideration, as they may affect the interpretation of the results of analyses conducted on this type of data.

In the context of functional connectivity analysis between an individual with Parkinson's disease and a healthy individual as a control, an AFNI software-based pre-processing pipeline appears to be more fit for purpose than an FSL software-based pipeline. In fact, the AFNI pipeline was found to be particularly appropriate because of its greater ability to identify and capture disease-relevant brain areas, such as motor regions, in the individual with Parkinson's disease.

4.2 Clinical and Scientific Implications

This work helped to enrich the clinical and neuroscientific landscape by providing considerations that could be considered in future research based on multi-echo resting-sate fMRI data.

In the first part of the study, it was found that the choice of pre-processing pipeline for multi-echo rs-fMRI data can significantly affect the quality of tSNR maps and the representation of certain brain regions, especially motor areas. This suggests that pipeline selection should be made according to the specific objectives of the study and the population of subjects analyzed, as the latter may require a special focus on certain areas that may be better highlighted using some pipelines than others.

This result thus underscores the importance of customizing pre-processing pipelines based on the subject population being studied, a factor that should be given greater consideration in a clinical setting. As shown in this study, the use of AFNI might be preferable when working with patients with Parkinson's disease, as it ensures the inclusion of the primary motor cortex compared with FSL.

In addition, the functional connectivity analysis performed helped reveal differences in correlations between brain networks between the Parkinson's disease subject and the healthy control individual. Strong positive correlations emerged between the Dorsal Attention Network and the Sensorimotor Network in both groups, suggesting more effective integration of cognitive and motor activities. In contrast, negative correlations between Parkinson's disease patient brain networks in opposite hemispheres revealed potential asymmetries in brain responses. These findings may carry important implications for research pertaining to visual perception, response to salient stimuli, and brain activity dynamics specific to this condition.

Thus, with this study, the importance of carefully considering the implications of software choices for processing multi-echo rs-fMRI data and tailoring the pre-processing approach to the specific context of the study was emphasized, thereby improving the validity and applicability of neuroscience research.

The adoption of the AFNI software-based pipeline proved to be particularly suitable for analyzing functional connectivity in disease-relevant brain regions, providing insights in this context. Through this study, a contribution has been made to the understanding of the pathology, paving the way for the possibility of considering therapeutic approaches targeted to the population of interest.

However, it is again emphasized that further statistical analysis on a larger sample of subjects is recommended to confirm these findings to better understand the impact of pipelines on rs-fMRI data quality.

4.3 Limitations of the Study and Possible Future Implementations

In the course of this study, it is important to consider some limitations that could affect the interpretation of the results and that could provide insights for future implementations of the study. It is important to note that this was a project started from scratch, which required a considerable amount of time to develop a coherent research topic and plan the necessary steps.

The most important limitation concerns the sample of subjects considered in the study, as it included only two participants and turned out to be extremely limited: a 60-year-old patient with Parkinson's disease and a healthy 70-year-old individual, both of whom had MMSE scores of 30. Because of such a small size, the considerations made may not be representative of the general population and, consequently, the results obtained may not be generalizable.
In addition, the selection of these subjects was not based on specific criteria but was done randomly from a larger dataset, which could introduce a potential bias in the representativeness of the participants.

Another limitation relates to methodological differences in the implementation of the two preprocessing pipelines, such as the coregistration software used: SPM12 was used in the AFNI-based pipeline, while ANTs were used in the FSL-based pipeline. This discrepancy may have influenced the results, making it difficult to determine whether the observed differences between the two preprocessing pipelines are attributable to the specific coregistration methodologies or other factors.
In addition, the implementation of the data regression model and the low-pass filter was performed using functions specific to two different programming languages: MatLab was used in the AFNI-based pipeline, while Python was used in the FSL-based pipeline. Although this choice of implementation should not have a significant impact on the results, it would be worth considering this difference in future studies to reduce the disparity between the two pipelines and make the results more directly comparable.

Finally, connectivity analysis was conducted using a Schaefer atlas with 200 parcels and 17 networks, on coregistered data in structural space. Future research might consider using different atlases or conducting the analyses on spaces other than structural space to further explore brain connectivity.

Future implementations of the study should include a larger and more representative sample of participants, greater control over the consistency of the methodologies used between the two pipelines, and the use of different atlases in the functional connectivity analysis, while also exploring other spaces.

The implementation of an integrated approach of both pipelines, AFNI and FSL, could also be considered: their use in a complementary way could be advantageous as it would allow the strengths of each software to be exploited according to the needs of the analysis.

These improvements could contribute to a deeper and more reliable understanding of brain connectivity in subjects with Parkinson's disease and healthy controls.

4.4 Conclusions

In conclusion, this study demonstrated the critical role played by the choice of pre-processing pipeline in the analysis of multi-echo rs-fMRI data and the subsequent influence exerted by it on data quality and interpretation.

Considering a subject with Parkinson's Disease and a healthy control subject, two pre-processing pipelines were implemented and compared: one based on AFNI, and one based on FSL.

It was made clear that the choice of pipeline should be made taking into consideration the specific objectives of the research and the characteristics of the investigated subject population, encouraging the customization of the pipeline according to the study context to obtain more accurate and reliable results.

Although both pipelines have been shown to be able to produce similar tSNR maps in terms of mean values and distribution, with a higher yield of FSL in terms of mean tSNR, it was found that the AFNI pipeline seems to be more suitable for analyzing functional connectivity, especially in brain regions relevant to Parkinson's disease such as motor areas. With this aspect, the impact on the results exerted by the choice of preprocessing software was emphasized, as it can significantly influence the interpretation of the data and the quality of the resulting images.

With this study, differences in correlations between brain networks between the two subjects analyzed were also investigated: the strong positive correlations between the Dorsal Attention Network and the Sensorimotor Network in both suggest greater integration of cognitive and motor activities during wakefulness and attention. On the other hand, negative correlations between Salience Network (SN) and Visual Network in the patient with Parkinson's disease could reflect asymmetries in brain responses specific to this condition, with implications for visual perception and response to salient stimuli.

However, it is important to recognize the limitations of this study, chief among them the sample size of subjects used: the presence of only two participants, a patient with Parkinson's disease and a healthy individual, could limit the generalization of the results. In addition, the random selection of these subjects may have introduced a potential bias in the results, as no specific inclusion criteria were applied. Future implementations of the study should aim to address these limitations by considering a larger and more representative sample of subjects.

Another factor to take into consideration concerns the methodological differences between the two compared pipelines: the fact that they differ in terms of coregistration software and means of implementing regression models and low-pass filters may have contributed to the discrepancies observed in the results. Therefore, it would be advisable for a more direct comparison to standardize the methodologies between the pipelines to make the results more comparable.

In addition, a more comprehensive perspective of the results could be had by considering conducting the analyses in spaces other than structural and implementing an integrated approach using both pipelines, exploiting the strengths of AFNI and FSL as needed.

Despite these limitations, this study thus highlighted the critical importance of pre-processing pipeline selection in the analysis of multi-echo rs-fMRI data, paving the way for potential therapeutic interventions targeting specific brain regions especially in the context of Parkinson's disease. It also indicated the need for further research with larger samples and more standardized methods to confirm and expand these findings. The implications of this study could thus improve the understanding of brain connectivity in health and disease conditions.

Chapter 5: References

6.1 Bibliography

[1] Kandel ER, Koester JD, Mack SH, Siegelbaum SA. Principles of Neural Science, Sixth Edition. McGraw Hill LLC, 2021. ISBN: 9781259642241. https://books.google.it/books?id=IYoEEAAAQBAJ

[2] Yousaf T, Dervenoulas G, Politis M. Advances in MRI Methodology. Int Rev Neurobiol. 2018;141:31-76. doi: 10.1016/bs.irn.2018.08.008. Epub 2018 Sep 14. PMID: 30314602.

[3] Smitha KA, Akhil Raja K, Arun KM, Rajesh PG, Thomas B, Kapilamoorthy TR, Kesavadas C. Resting state fMRI: A review on methods in resting state connectivity analysis and resting state networks. Neuroradiol J. 2017 Aug;30(4):305-317. doi: 10.1177/1971400917697342. Epub 2017 Mar 29. PMID: 28353416; PMCID: PMC5524274.

[4] Huettel SA, Song AW, McCarthy G. Functional Magnetic Resonance Imaging. Oxford University Press, Incorporated, 2009, p.26. ISBN: 9780878932863. https://books.google.it/books?id=BNhMPgAACAAJ

[5] Lv H, Wang Z, Tong E, Williams LM, Zaharchuk G, Zeineh M, Goldstein-Piekarski AN, Ball TM, Liao C, Wintermark M. Resting-State Functional MRI: Everything That Nonexperts Have Always Wanted to Know. AJNR Am J Neuroradiol. 2018 Aug;39(8):1390-1399. doi: 10.3174/ajnr.A5527. Epub 2018 Jan 18. PMID: 29348136; PMCID: PMC6051935.

[6] Agcaoglu O, Wilson TW, Wang YP, Stephen J, Calhoun VD. Resting state connectivity differences in eyes open versus eyes closed conditions. Hum Brain Mapp. 2019 Jun 1;40(8):2488-2498. doi: 10.1002/hbm.24539. Epub 2019 Feb 5. PMID: 30720907; PMCID: PMC6865559.

[7] Sharaev MG, Zavyalova VV, Ushakov VL, Kartashov SI, Velichkovsky BM. Effective Connectivity within the Default Mode Network: Dynamic Causal Modeling of Resting-State fMRI Data. Front Hum Neurosci. 2016 Feb 1; 10:14. doi: 10.3389/fnhum.2016.00014. PMID: 26869900; PMCID: PMC4740785.

[8] Song XW, Dong ZY, Long XY, Li SF, Zuo XN, Zhu CZ, He Y, Yan CG, Zang YF. REST: a toolkit for resting-state functional magnetic resonance imaging data processing. PLoS One. 2011;6(9):e25031. doi: 10.1371/journal.pone.0025031. Epub 2011 Sep 20. PMID: 21949842; PMCID: PMC3176805.

[9] Tessitore A, Cirillo M, De Micco R. Functional Connectivity Signatures of Parkinson's Disease. J Parkinsons Dis. 2019;9(4):637-652. doi: 10.3233/JPD-191592. PMID: 31450512; PMCID: PMC6839494.

[10] Kundu P, Voon V, Balchandani P, Lombardo MV, Poser BA, Bandettini PA. Multi-echo fMRI: A review of applications in fMRI denoising and analysis of BOLD signals. Neuroimage. 2017 Jul 1;154:59-80. doi: 10.1016/j.neuroimage.2017.03.033. Epub 2017 Mar 29. PMID: 28363836.

[11] Axel L. Glossary of MR Terms. American College of Radiology. Magn Reson Imaging. 1987;5(3):163-4. doi: 10.1016/0730-725x(87)90015-4. PMID: 3626784.

[12] Elster AD, Burdette JH. Questions & Answers in Magnetic Resonance Imaging. Mosby, 2001. ISBN: 9780323011846. https://books.google.it/books?id=QY5jQgAACAAJ

[13] Meijer FJ, Goraj B. Brain MRI in Parkinson's disease. Front Biosci (Elite Ed). 2014 Jun 1;6(2):360-9. doi: 10.2741/E711. PMID: 24896211.

[14] Lin H, Cai X, Zhang D, Liu J, Na P, Li W. Functional connectivity markers of depression in advanced Parkinson's disease. Neuroimage Clin. 2020;25:102130. doi: 10.1016/j.nicl.2019.102130. Epub 2019 Dec 13. PMID: 31869768; PMCID: PMC6931212.

[15] Cucca A, Di Rocco A, Acosta I, Beheshti M, Berberian M, Bertisch HC, Droby A, Ettinger T, Hudson TE, Inglese M, Jung YJ, Mania DF, Quartarone A, Rizzo JR, Sharma K, Feigin A, Biagioni MC, Ghilardi MF. Art therapy for Parkinson's disease. Parkinsonism Relat Disord. 2021 Mar;84:148-154. doi: 10.1016/j.parkreldis.2021.01.013. Epub 2021 Jan 23. PMID: 33526323.

[16] Lundbeck Institute Campus. History, definitions and diagnosis. Migraine - 06.04.2021. https://institute.progress.im/

[17] Goetz CG, Tilley BC, Shaftman SR, Stebbins GT, Fahn S, Martinez-Martin P, Poewe W, Sampaio C, Stern MB, Dodel R, Dubois B, Holloway R, Jankovic J, Kulisevsky J, Lang AE, Lees A, Leurgans S, LeWitt PA, Nyenhuis D, Olanow CW, Rascol O, Schrag A, Teresi JA, van Hilten JJ, LaPelle N; Movement Disorder Society UPDRS

Revision Task Force. Movement Disorder Society-sponsored revision of the Unified Parkinson's Disease Rating Scale (MDS-UPDRS): scale presentation and clinimetric testing results. Mov Disord. 2008 Nov 15;23(15):2129-70. doi: 10.1002/mds.22340. PMID: 19025984.

[18] Hoehn MM, Yahr MD. Parkinsonism: onset, progression and mortality. Neurology. 1967 May;17(5):427-42. doi: 10.1212/wnl.17.5.427. PMID: 6067254.

[19] Goetz CG, Poewe W, Rascol O, Sampaio C, Stebbins GT, Counsell C, Giladi N, Holloway RG, Moore CG, Wenning GK, Yahr MD, Seidl L; Movement Disorder Society Task Force on Rating Scales for Parkinson's Disease. Movement Disorder Society Task Force report on the Hoehn and Yahr staging scale: status and recommendations. Mov Disord. 2004 Sep;19(9):1020-8. doi: 10.1002/mds.20213. PMID: 15372591.

[20] Dayan E, Sklerov M. Autonomic disorders in Parkinson disease: Disrupted hypothalamic connectivity as revealed from resting-state functional magnetic resonance imaging. Handb Clin Neurol. 2021;182:211-222. doi: 10.1016/B978-0-12-819973-2.00014-9. PMID: 34266593.

[21] Chao-Gan Y, Yu-Feng Z. DPARSF: A MATLAB Toolbox for "Pipeline" Data Analysis of Resting-State fMRI. Front Syst Neurosci. 2010 May 14;4:13. doi: 10.3389/fnsys.2010.00013. PMID: 20577591; PMCID: PMC2889691.

[22] Cox RW. AFNI: what a long strange trip it's been. Neuroimage. 2012 Aug 15;62(2):743-7. doi: 10.1016/j.neuroimage.2011.08.056. Epub 2011 Aug 27. PMID: 21889996; PMCID: PMC3246532.

[23] Ziad S. Saad, Daniel R. Glen, Gang Chen, Michael S. Beauchamp, Rutvik Desai, Robert W. Cox. A new method for improving functional-to-structural MRI alignment using local Pearson correlation. NeuroImage, Volume 44, Issue 3, 2009, Pages 839-848. ISSN 1053-8119. https://doi.org/10.1016/j.neuroimage.2008.09.037.

[24] Kassinopoulos M, Mitsis GD. A multi-measure approach for assessing the performance of fMRI preprocessing strategies in resting-state functional connectivity. Magn Reson Imaging. 2022 Jan;85:228-250. doi: 10.1016/j.mri.2021.10.028. Epub 2021 Oct 27. PMID: 34715292.

[25] Ashburner, John & Barnes, Gareth & Chen, Chun-Chuan & Daunizeau, Jean & Flandin, Guillaume & Friston, Karl & Gitelman, Darren & Glauche, Volkmar & Henson, Rik & Hutton, Chloe & Jafarian, Amirhossein & Kiebel, Stefan & Kilner, James & Litvak, Vladimir & Mattout, Jérémie & Moran, Rosalyn & Penny, Will & Phillips, Christophe & Razi, Adeel & Zeidman, Peter. (2021). SPM12 Manual.

[26] Viviani R, Grön G, Spitzer M. Functional principal component analysis of fMRI data. Hum Brain Mapp. 2005 Feb;24(2):109-29. doi: 10.1002/hbm.20074. PMID: 15468155; PMCID: PMC6871761.

[27] Bartoň M, Mareček R, Krajčovičová L, Slavíček T, Kašpárek T, Zemánková P, Říha P, Mikl M. Evaluation of different cerebrospinal fluid and white matter fMRI filtering strategies-Quantifying noise removal and neural signal preservation. Hum Brain Mapp. 2019 Mar;40(4):1114-1138. doi: 10.1002/hbm.24433. Epub 2018 Nov 7. PMID: 30403309; PMCID: PMC6865642.

[28] Chen JE, Glover GH. Functional Magnetic Resonance Imaging Methods. Neuropsychol Rev. 2015 Sep;25(3):289-313. doi: 10.1007/s11065-015-9294-9. Epub 2015 Aug 7. Erratum in: Neuropsychol Rev. 2015 Sep;25(3):314. PMID: 26248581; PMCID: PMC4565730.

[29] Schaefer A, Kong R, Gordon EM, Laumann TO, Zuo XN, Holmes AJ, Eickhoff SB, Yeo BTT. Local-Global Parcellation of the Human Cerebral Cortex from Intrinsic Functional Connectivity MRI. Cereb Cortex. 2018 Sep 1;28(9):3095-3114. doi: 10.1093/cercor/bhx179. PMID: 28981612; PMCID: PMC6095216.

[30] Rieck JR, Baracchini G, Nichol D, Abdi H, Grady CL. Dataset of functional connectivity during cognitive control for an adult lifespan sample. Data Brief. 2021 Nov 15;39:107573. doi: 10.1016/j.dib.2021.107573. PMID: 34877370; PMCID: PMC8627991.

[31] Welvaert M, Rosseel Y. On the definition of signal-to-noise ratio and contrast-to-noise ratio for FMRI data. PLoS One. 2013 Nov 6;8(11):e77089. doi: 10.1371/journal.pone.0077089. PMID: 24223118; PMCID: PMC3819355.

[32] Jenkinson M, Beckmann CF, Behrens TE, Woolrich MW, Smith SM. FSL. Neuroimage. 2012 Aug 15;62(2):782-90. doi: 10.1016/j.neuroimage.2011.09.015. Epub 2011 Sep 16. PMID: 21979382.

[33] Pauli R, Bowring A, Reynolds R, Chen G, Nichols TE, Maumet C. Exploring fMRI Results Space: 31 Variants of an fMRI Analysis in AFNI, FSL, and SPM. Front Neuroinform. 2016 Jul 5;10:24. doi: 10.3389/fninf.2016.00024. PMID: 27458367; PMCID: PMC4932120.

6.2 Sitography

[a] https://tedana.readthedocs.io/en/latest/multi-echo.html#

[b] https://mriquestions.com/data-pre-processing.html

[c] https://mriquestions.com/best-fmri-software.html

[d] https://afni.nimh.nih.gov/pub/dist/doc/program_help/3dvolreg.html

[e] https://afni.nimh.nih.gov/pub/dist/doc/program_help/3dTshift.html

[f] https://afni.nimh.nih.gov/pub/dist/doc/program_help/3dQwarp.html

[g]https://github.com/ThomasYeoLab/CBIG/blob/master/stable_projects/brain_parcellation/Schaefer2018_LocalGlobal/Parcellations/MNI/README.md

[h] https://fsl.fmrib.ox.ac.uk/fsl/fslwiki/MCFLIRT

[i] https://poc.vl-e.nl/distribution/manual/fsl-3.2/slicetimer/index.html

[j] https://fsl.fmrib.ox.ac.uk/fsl/fslwiki/topup

[k] https://sphinx-doc-brant.readthedocs.io/en/latest/Menu_FC.html

[l] https://www.lead-dbs.org/helpsupport/knowledge-base/atlasesresources/cortical-atlas-parcellations-mni-space/